Novel Laser Based NiTi Shape Memory Alloy Processing Protocol for Medical Device Applications

By

Andrew Pequegnat

A thesis

presented to the University of Waterloo

in fulfilment of the

thesis requirement for the degree of

Doctor of Philosophy

in

Mechanical Engineering

Waterloo, Ontario, Canada, 2014

Author's declaration

I hereby declare that I am the sole author of this thesis. This is a true copy of the thesis, including any required final revisions, as accepted by my examiners.

I understand that my thesis may be made electronically available to the public.

Andrew Pequegnat

Abstract

The unique performance offerings of NiTi based shape memory alloys (SMAs), which includes the shape memory effect (SME), pseudoelasticity (PE) and biocompatibility have led to widespread acceptance of these alloys as valuable engineering materials. Over the past several decades the complex metallurgy behind the SME and PE properties has for the most part been uncovered and the design and engineering knowhow has been demonstrated; facilitating successful application of NiTi devices in numerous industries. Specifically, more mature applications in the medical industry including medical devices such as, catheters, guide wires, orthodontic arch wires, maxillofacial reconstruction implants, minimally invasive surgical tools, and arterial and gastrointestinal stents, have become common practice in modern medicine. Recently however, there has been a drive for more demanding functionality of SMAs for example to locally modify properties creating tuneable or gradient SME and PE performance. Unique processing protocols are therefore necessary to meet these demands and allow SMAs to reach their full potential in a wider range of applications. The current thesis successfully details the application of pulsed Nd:YAG laser processing along with post-processing techniques to locally tune both the SME and PE functional properties of monolithic binary NiTi wires and strip, while maintaining confidence in the retained corrosion performance and limited release of biologically harmful Ni ions. This extensive study contains three distinct parts which include: i) application of a laser induced vaporization protocol to locally embed multiple memories in a monolithic wire actuator; ii) uncovering the process, structure, and performance relationship of combined laser, cold working, and heat treatment processes; and iii) comprehensive characterization of surface characteristics and their relationship with corrosion performance and Ni ion release from laser processed material.

In the first part of this study, a novel laser induced vaporization protocol capable of locally modifying the shape memory effect property was applied to enhance the functionality of a NiTi linear actuator. By altering local transformation temperatures, an additional memory was imparted into a monolithic NiTi wire enabling dynamic actuation via controlled resistive heating. Characterisations of the actuator load, displacement, and cyclic properties were conducted using a custom-built spring biased test set-up. Monotonic tensile testing was also implemented to characterise the deformation behaviour of the martensite phase. Observed differences in the deformation behaviour of laser processed material were found to affect the magnitude of active strain. Furthermore, residual strain during cyclic actuation testing was found to stabilize after 150 cycles while the recoverable strain remained constant. This laser

processed actuator allows for the realization of new actuation applications and improved control methods for shape memory alloys.

In the second part of this study, a unique protocol to locally tune the structural and functional properties of NiTi based shape memory alloys (SMAs) was developed combining laser-induced vaporization, cold work, and heat treatment processes. Unprecedented SMA performance was achieved using precise process, structure, property correlations developed in this work. Specific focus was directed toward characterizing composition and microstructure of processed material using micro-particle induced x-ray emission (micro-PIXE) spectroscopy and transmission electron microscopy (TEM) respectively. Thermoanalytical properties were identified through differential scanning calorimetry (DSC) while the structural and functional properties, including the shape memory effect (SME) and pseudoelasticity (PE), were determined using micro-tensile testing at various temperatures. Extraordinarily precise control of Ni:Ti ratio was accomplished through laser induced vaporization leading to controlled changes in transformation temperatures. Subsequent cold rolling and annealing increased the yield strength allowing for tuneable performance offerings including multiple PE plateau stresses and combined SME and PE properties in monolithic tensile specimen. Synergistic behaviour of adjacent locally processed regions demonstrated a significant increase in SMA functionality and their potential in future application.

Finally, laser processing of NiTi SMAs promises to enable useful multifunctional capabilities for medical device applications as demonstrated in parts i) and ii) of this study. However, prior to clinical implementation, understanding of the surface characteristics is essential in order to identify any adverse performance or biological interaction that may occur. The current study systematically investigated two laser processed surface finishes, including as-processed and mechanically polished, while comparing them to a chemically etched parent material. Spectrographic characterisation of the surface included; x-ray photoelectron (XPS), auger electron (AES), and Raman. Corrosion performance and Ni ion release were also assessed using potentiodynamic cyclic polarization testing and inductively coupled plasma optical emission spectroscopy (ICP-OES), respectively. Results showed that surface defects, including increased roughness, crystallinity, and presence of volatile oxide species, overshadowed any possible performance improvements from a decreased Ni:Ti ratio or inclusion dissolution imparted by laser processing. However, post-process mechanical polishing was shown to remove these defects and restore the performance, making it comparable to chemically etched NiTi material.

Acknowledgements

I would like to thank my supervisor Prof. Norman Y. Zhou for valuable career and life lessons as well as for freedom in pursuing my research and academic goals. My success in this chapter of my life was not possible without his mentorship and support. The memories and successes that were shared with my colleagues in the Centre for Advanced Materials Joining (CAMJ) will never be forgotten.

I would also like to acknowledge Matt Daly for assisting with the ground work in the area of post processing of laser processed NiTi as well as Jeff Wang and Andrew Michael for assisting with corrosion and surface characterization experiments and data analysis.

Finally, I would like to thank my family for their love and support. My successes in life would not be possible without them.

This work has been supported by the Natural Sciences and Engineering Research Council of Canada (NSERC).

Dedication

To My Beautiful, Supportive Wife Colleen

&

My Awesome Son Riley

Table of contents

List of figures

List of tables

1 Introduction

1.1. Background

The unique shape memory effect of NiTi based alloys (also known as Nitinol) was first discovered in 1963 by Buehler et al. [1]. The popularity of NiTi alloys compared to shape memory alloys (SMAs) discovered earlier, such as Au-Cd [2] and In-Tl [3] alloys, is a result of their superior mechanical and functional properties as well as the promotion of the alloy by the world-renowned Naval Ordinance Laboratory [4]. NiTi alloys are the most commonly applied SMAs due to superior strength, ductility, recoverable strains, corrosion resistance, biocompatibility, and stability of transformation temperatures [4]. Application of NiTi alloys however did not occur until the 1980s, before which necessary research was conducted to adequately understand the alloy due to the complex nature of the NiTi system [4].

In addition to understanding the complex metallurgy behind the SME and PE properties [4], the design and engineering knowhow has also now been demonstrated [5, 6] facilitating successful application of NiTi devices in numerous industries including, medical, automotive, aerospace, and micro-electronics. Their potential in high profile applications such as minimal-invasive surgical tools, biomedical implants, and energy harvesting clean technologies are driving innovation and application of these smart materials [5-10]. There are however still limitations of the traditional NiTi processing methods and a lack of understanding of new promising processing technologies such as, laser processes, that must be addressed before NiTi SMAs can reach their full potential in engineering application. Addressing these limitations in traditional manufacturing technologies through novel laser processes and better understanding the effects of laser processing combined with post-processing treatments on material performance is therefore the basis of this thesis work. In particular, detailed studies into the process, structure, and performance relationship were conducted, furthering the science of thermomechanical processing of NiTi SMAs. Specific focus was directed to medical device requirements as the medical device industry has already embraced NiTi SMAs in several extremely successful applications including, but not limited to, catheters, guide wires, orthodontic arch wires, maxillofacial reconstruction implants, minimally invasive surgical tools, and arterial and gastrointestinal stents [5, 7-9]. The medical device industry was identified as having immediate applications suited for enhanced functionality achieved via novel laser processing SMA technologies.

1.2. Objectives

The motivation behind this work was to develop novel laser processing protocol to improve the functionality of NiTi based SMAs and expand the potential applications suitable for immediate implementation of these smart materials. Currently only limited studies exist on the laser processing of NiTi SMAs. Therefore, comprehensive analysis of a pulsed Nd:YAG laser process was undertaken, addressing the following important objectives:

1. Demonstrate the application of laser induced vaporization to locally augment the functional properties of monolithic NiTi components and characterize necessary performance metrics to better understand SME properties and means of actuation and control;
2. Characterize the process, structure, and performance relationship of Nd:YAG laser processed NiTi and explore the possibilities of post-laser processing for improving SME and PE performance while further increasing functionality; and
3. Identify the surface characteristics of laser processed NiTi materials and the effects of laser processing on corrosion performance and release of biologically harmful Ni ions.

1.3. Thesis organization

This thesis is subdivided into eight chapters. Chapter 2 provides an up to date literature review of the physical metallurgy and the processing protocol currently utilized during their manufacture. In this chapter the limitations of current processing technologies as well as in our understanding of the complex NiTi system are identified. Novel unprecedented local processing technologies including laser processing are introduced along with the motivation behind this work.

Chapter 3 details experimental methods and conditions used in this comprehensive study including information regarding the test equipment and procedures followed.

Chapter 4 reports for the first time on the development and characterization of a laser processed monolithic NiTi actuator. Detailed thermal analysis along with tensile testing at various temperatures allowed for in-depth understanding of the SME performance, including cyclic behaviour of laser processed NiTi SMAs. A simple means of resistive heating control was also developed to identify the extensive potential for these novel processed actuators in application.

Chapter 5 details the process, structure, and performance relationship for laser and post-processed NiTi materials. More specifically, the laser induced vaporization mechanism was proven through precision

composition measurement made using micro-PIXE spectroscopy and the thermoanalytical properties and microstructure were characterized using systematic DSC and TEM analysis. Through tensile testing at various temperatures improved performance and extremely unique and desirable functional SME and PE properties were demonstrated.

Chapter 6 characterizes the surface condition of laser processed NiTi material through various spectrographic techniques including XPS, AES, and Raman. Correlations between the surface condition and corrosion and Ni-ion release performance of laser processed material were also made using cyclic potentiodynamic corrosion testing and ICP-OES respectively. Moreover, past theories regarding the corrosion and Ni-ion release performance of laser processed NiTi material were tested. Simple surface treatments such as mechanical polishing were found to greatly improve the resistance to corrosion through removing superficial surface defects and confidence in using laser processed material in medical device applications was instilled.

Chapter 7 details the main conclusions of this research study and future recommendations are provided for laser processing technologies and direction of future research.

Finally, Chapter 8 lists significant contributions to research and development by the author.

2 Literature Review

2.1. Physical metallurgy of NiTi SMAs

NiTi shape memory alloys are a group of NiTi alloys with near equiatomic composition; as shown in the binary Ti-Ni phase diagram of Figure 1 [4, 11]. At room temperature NiTi SMAs are stoichiometric intermetallic compounds (IMC). This NiTi IMC is unique since it possesses shape memory properties and also remarkably has good mechanical properties such as ductility and strength [4]. Binary NiTi is not a line-compound with a fixed composition. Above 923 K (650 °C) Ni is soluble in Ti, therefore through quenching supersaturated Ni-rich NiTi SMAs can be produced. Ti-rich supersaturated mixtures on the other hand are not possible because Ti cannot dissolve in excess. Besides NiTi, there are many other IMCs in the Ti-Ni system. The IMCs that can be found adjacent to near equiatomic NiTi are also very important with respect to material properties. The Ti-rich Ti_2Ni IMCs, along with TiC are however, commonly found in bulk NiTi material due to the ingot casting process during material manufacture [6] as shown in Figure 2 [12]. These inclusions are generally not seen to be a large issue affecting material performance but limiting inclusions is always seen as best practice [6]. Ti_2Ni IMCs are however, undesirable in rapid solidification processes such as in welding due to their poor mechanical properties often leading to solidification cracking [13]. In contrast, metastable Ni-rich precipitates (i.e. Ni_4Ti_3, Ni_3Ti_2, and Ni_3Ti) are utilized to tailor the functional properties of the alloy and are very important in achieving the desired functional and mechanical properties for a specific application [14, 15].

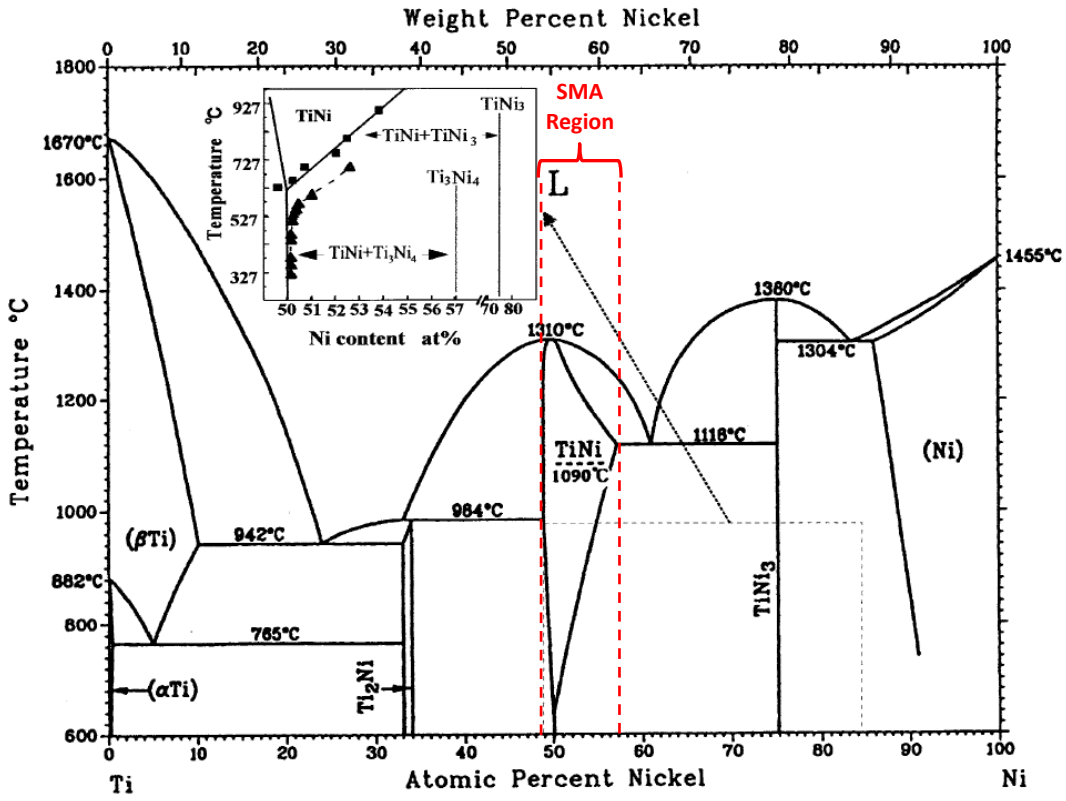

Figure 1: Binary Ti-Ni phase diagram. Inset showing metastable Ni-rich TiNi IMCs. Figure adapted from [4, 11].

The unique shape memory properties of NiTi SMAs are a result of a reversible solid-state phase transformation that occurs when the material is subject to external stimuli such as a change in temperature or applied stress. This diffusionless martensitic transformation occurs between the parent B2 austenite phase and the B19' martensite phase [6, 16, 17]. The parent B2 austenite phase is a simple cubic CsCl type ordered structure with a lattice parameter of 0.3015 nm as illustrated in Figure 3 a) [18]. The B19' martensite phase has a monoclinic structure with lattice parameters of a = 0.2889, b = 0.4120, and c = 0.4622 nm with a monoclinic angle β = 96.8°, as illustrated in Figure 3 b) [19].

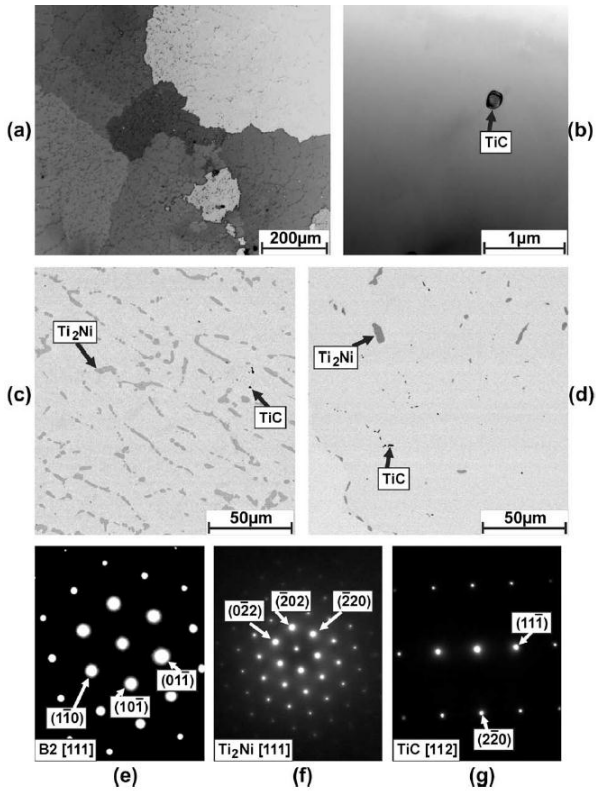

Figure 2: Microstructures of NiTi: a) optical micrograph of the grain structure of a NiTi alloy with 51.0 at.% Ni; b) TEM bright field image showing low dislocation density and carbide of type TiC; c) and d) backscatter SEM micrographs of a NiTi alloy with c) 48.6 at.% Ni and d) 51.0 at.% Ni; and e)–g) TEM diffraction patterns of e) the B2 phase in NiTi with 51 at.% Ni, f) Ti_2Ni in a NiTi alloy with 51 at.% Ni and g) TiC. Figure taken from [12].

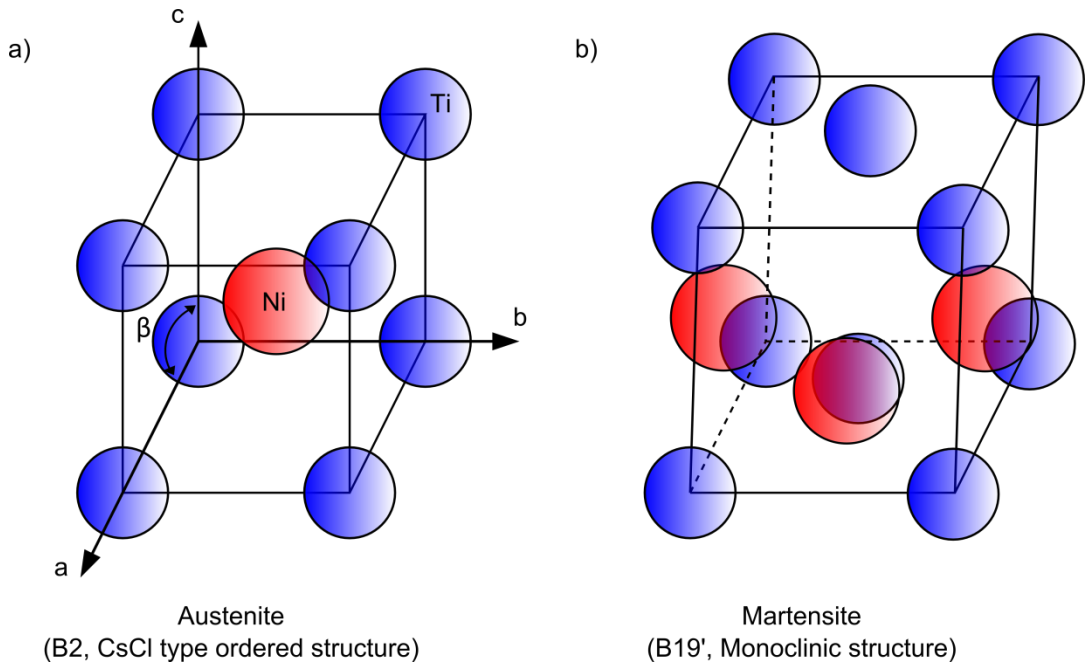

Figure 3: a) Parent B2 austenite and b) B19' martensite unit cells (not to scale)

2.1.1. Reversible martensitic transformations in NiTi alloys

Martensitic phase transformation is defined as a shear/shuffle of the crystal lattice that takes place due to a change in the thermodynamic stability of the system. The reversible martensitic phase transformation that occurs in SMAs is accommodated through twinning of the crystal lattice [19-21]. Unlike during martensitic transformation in steel alloys (i.e. fcc → bct) which is accommodated by irreversible dislocation motion, twinning in SMAs can be reversible allowing for unique functional properties. The slip and twinning type of accommodation for martensitic transformations are illustrated in Figure 4. During slip, the atomic planes glide over one another creating irreversible dislocations in the crystal lattice. This phenomenon occurs more easily in materials that have fcc and bcc crystal structures due to the many slip systems available and/or high stacking fault energies. Twinning on the contrary is the shearing of the crystal lattice where the structures on each side of the habit plane are mirror and/or rotation related and the atomic movement relative to one another is less than one atomic spacing. Twinning occurs in NiTi SMAs because of lack of symmetry and hence a lack of slip systems available, increasing the driving force for creating twins following the martensitic phase transformation. The B19' martensite crystal structure has many twinning modes available (Table 1) and only one slip mode $(001)[100]_{B19'}$.

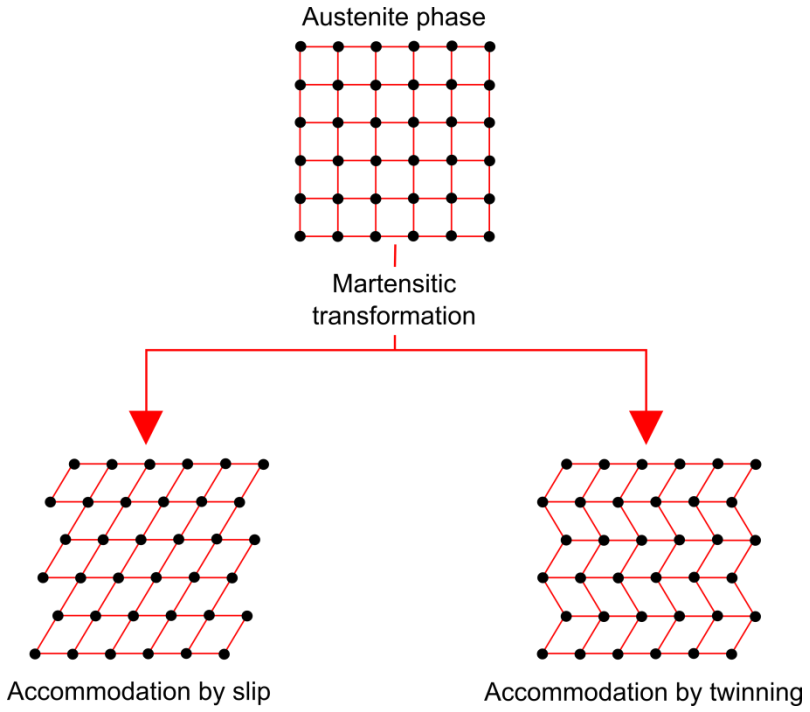

Figure 4: Martensitic phase transformation accommodation by irreversible slip or reversible twinning in the crystal lattice

Table 1: Twinning modes in B19' martensite phase and their respective twinning elements [4]

Twin type	K_1	η_1	K_2	η_2	s (i.e. shear)
$\{\bar{1}\bar{1}1\}$ Type I [1]	$(\bar{1}\bar{1}1)$	$[0.54043\ 0.45957\ 1]$	$(0.24695\ 0.50611\ 1)$	$[\bar{2}\bar{1}1]$	0.30961 nm
	$(\bar{1}11)$	$[0.54043\ \overline{0.45957}\ 1]$	$(0.24695\ \overline{0.50611}\ 1)$	$[\bar{2}11]$	0.30961
$\{111\}$ Type I	(111)	$[\overline{1.51172}\ 0.51172\ 1]$	$(\overline{0.66875}\ 0.33750\ 1)$	$[211]$	0.14222
	$(1\bar{1}1)$	$[\overline{1.51172}\ \overline{0.51172}\ 1]$	$(\overline{0.66875}\ \overline{0.33750}\ 1)$	$[2\bar{1}1]$	0.14222
$\{011\}$ Type I [1]	(011)	$[1.57271\ 1\ \bar{1}]$	$(0.72053\ 1\ \bar{1})$	$[011]$	0.28040
	$(01\bar{1})$	$[\overline{1.57271}\ 1\ 1]$	$(\overline{0.72053}\ 1\ 1)$	$[01\bar{1}]$	0.28040
$\langle 011\rangle$ Type II [1,2]	$(0.72053\ 1\ \bar{1})$	$[011]$	(011)	$[1.57271\ 1\ \bar{1}]$	0.28040
	$(\overline{0.72053}\ 1\ 1)$	$[01\bar{1}]$	$(01\bar{1})$	$[\overline{1.57271}\ 1\ 1]$	0.28040
Compound	(001)	$[100]$	(100)	$[001]$	0.23848
	(100)	$[001]$	(001)	$[100]$	0.23848
$\{20\bar{1}\}$ [3]	$(20\bar{1})$	$[\bar{1}0\bar{2}]$	$(00\bar{1})$	$[100]$	0.4250

1. lattice invariant shear
2. Dominant twinning mode
3. $\{20\bar{1}\}$ twinning is an irreversible deformation twinning mode under heavy deformation

There are three different paths that the martensitic transformation can take in NiTi base alloy systems [4]. These different paths are presented in Figure 5 to assist in the following discussion. The simplest path is the first order thermoelastic martensitic transformation from B2 austenite to B19' martensite. This transformation is observed in binary Ni-Ti systems which have either been solution treated or possess only low amounts of cold work or precipitation [4]. The second transformation path is from B2 to the trigonal R-phase and then finally to the B19' martensite phase. R-phase transformation is a martensitic transformation that competes with B19' martensite in materials that have high dislocation density, Ni-rich precipitates, or in ternary alloys that contain Fe [22, 23]. In this case the B19' martensite transformation is suppressed by either the Fe alloying element, dislocations following cold work, and/or the precipitation of Ni-rich precipitates, allowing R-phase to form [4]. Chemical substitution of Fe in to the matrix, dislocations, and Ni_4Ti_3 precipitates all resist large lattice variant deformations associated with the formation of B19' martensite. Since the R phase produces a significantly smaller lattice variant deformation it will therefore preferentially form [4, 24, 25]. The third transformation path is from B2 austenite to orthorhombic B19 martensite then finally to B19' martensite [26]. This type of martensitic transformation is only observed in ternary Ni-Ti-Cu systems with Cu compositions above 7.5 at.%. It is still debated whether B19 occurs in Ni-Ti-Cu alloys with Cu compositions below 7.5 at.% [4].

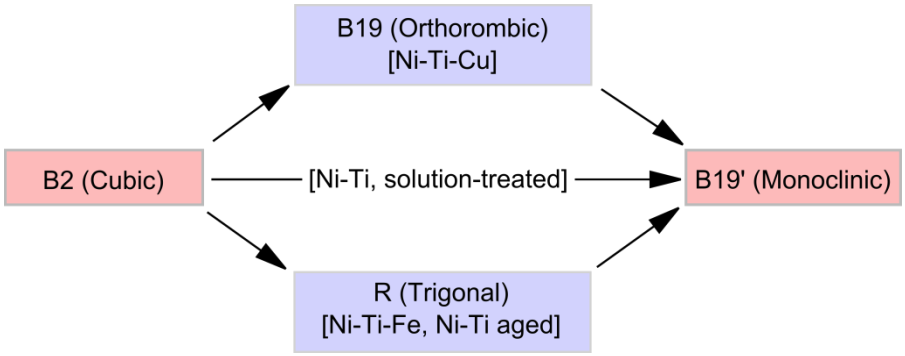

Figure 5: Three possible martensitic transformation paths in NiTi based alloys [4].

The structural relationships between the B2, B19 and B19' phases are illustrated in Figure 6 [27]. It can be seen that the B2 to B19 martensitic transformation occurs through the common shear/shuffle of the basal plane $(110)_{B2}$ along the $[1\bar{1}0]$ direction. The transformation to B19' however also includes a non-basal $(001)[1\bar{1}0]_{B2}$ shear component leading to the monoclinic angle β which is a unique martensitic transformation [27]. The B2 to R phase transformation is more complex and not yet fully understood [4] therefore not reviewed here. One proposed theory on the precursor R-phase transformation can however be found in the Selected Area Diffraction Pattern (SADP) investigation of Wu et al. [28].

Of the three paths that the transformation can take (i.e. B2-B19', B2-R-B19', or B2-B19-B19') the specific path taken depends on precursor events such as phonon softening that directly affects stability of the different phases [29]. Phonon softening results in softening of the elastic moduli c' and c_{44}, which represent resistance to basal plane $\{110\}\langle 1\bar{1}0\rangle_{B2}$ and non-basal plane $\{001\}\langle 100\rangle_{B2}$ (i.e. or $\{001\}\langle 1\bar{1}0\rangle$ due to cubic symmetry) shear, respectively [27]. The relative softening of c' and c_{44} and the resulting anisotropy factor A ($=c_{44}/c'$) dictates the path that the martensitic transformation takes in NiTi SMAs [29]. For example, significant softening in c_{44} is always observed as temperature approaches the B19' martensite phase transformation temperature which explains the ultimate transformation to B19', even though precursor (R or B19) martensites may occur [4]. It is important to note that the softer the c_{44} the higher the phase transformation temperature of B19' [4]; addressed in more detail when discussing the effects of NiTi alloy composition on functional properties.

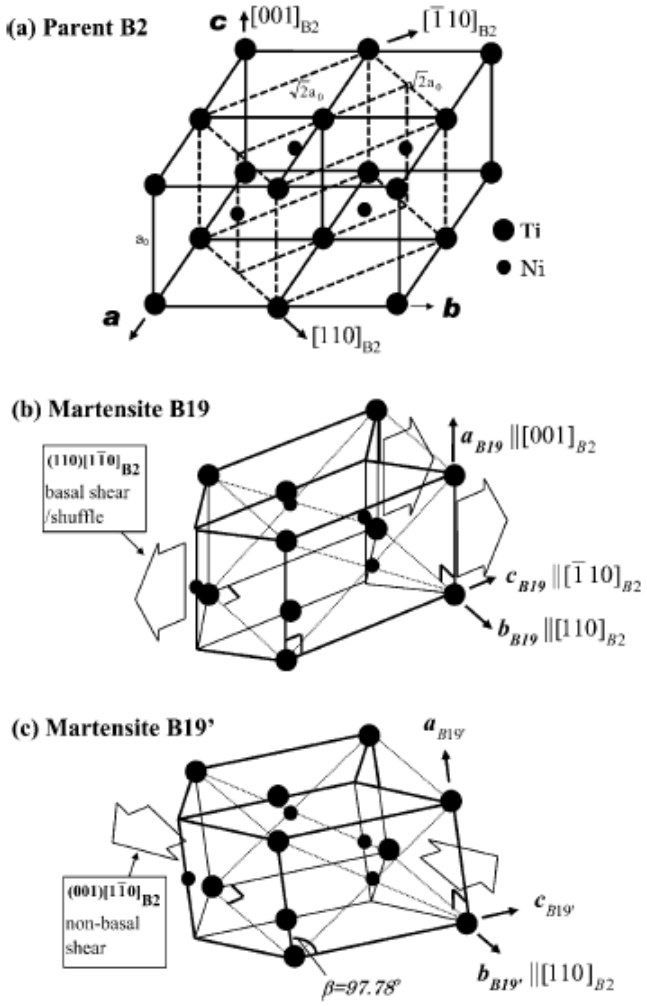

Figure 6: a) Structural relation between B2, b) B19, and c) B19'. Figure taken from [26].

2.1.2. Mechanism for high ductility of NiTi alloys

Despite the fact that NiTi alloys are IMCs they can exhibit elongation upwards of 50 % in tensile loading conditions due to very high ductility, as reported by Miyazaki et al. [30]. This high ductility of the NiTi IMC was proposed by Otsuka and Ren [4] to be the result of both the elastic behaviour of the material and martensitic transformations. The elasticity constants c' and c_{44} are thought to contribute to low critical stress for slip in NiTi [27]. Low c' and c_{44} compared to other IMCs (Table 2) translates to a decrease in rigidity of the crystal structure which is proportional to the stress required to move dislocations [27]. Also, the low anisotropy factor 'A' of NiTi, calculated to be less than 2, promotes high ductility because fracture at grain boundaries is avoided [31]. A softening in both the c' and c_{44} occurs in NiTi with lowering temperature further towards the martensite start (M_s) phase transformation temperature decreasing anisotropy, unlike in other SMAs where only c' displays softening (Table 2) [27].

Table 2: Elastic properties of NiTi and other β phase alloys near M_s (i.e. SMA IMCs). Table adapted from [27].

Elastic properties near M_s	**NiTi**	CuAlNi	CuZn	CuZnAl	AuZnCu	AuCd	NiAl
c' (GPa)	**17-19**	~7	8	5.8	3-5	3-3.8	14.6
Softening of c'	**Yes**	Yes	Yes	Yes	Yes	Yes	Yes
c_{44} (GPa)	**35-39**	95	90	86	~60	42	132
Softening of c_{44}	**Yes**	No	No	No	No	No	No
A = c_{44}/c'	**2**	13	11	15	20-12	14-11	9
Softening of A	**Yes**	No	No	No	No	No	No

The correlation between temperature and elongation during tensile testing was reported by Miyazaki et al. [32]; shown in Figure 7. In the B19' martensite phase at low temperatures, NiTi exhibits high ductility due to many twinning modes that are available (Table 1) in addition to the slip mode $(001)[100]_{B19'}$. The highest ductility is however available in the B2 austenite phase near the M_s temperature due to the fact that stress-induced-martensite (SIM) transformation is possible (i.e. with 24 theoretical variants) as an additional deformation mode. The lowest ductility occurs at high temperatures where SIM is not possible and only the slip mode $\{001\}\langle 100\rangle_{B2}$ and twinning modes $\{114\}\langle 22\bar{1}\rangle_{B2}$ are available.

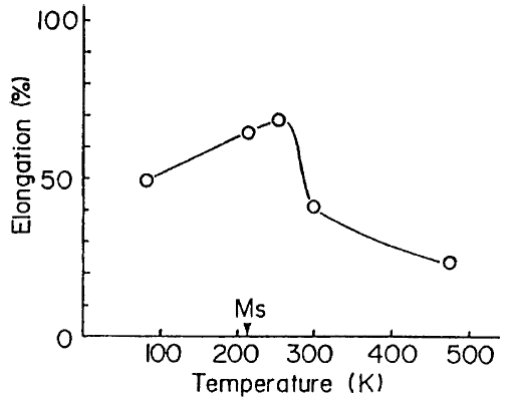

Figure 7: Change in tensile elongation with testing temperature for a Ti - 51.0 at% Ni alloy. Figure taken from [32].

2.2. Functional properties

The functional properties of SMAs originate from the thermomechanical response of the material. The thermomechanical response of NiTi SMAs can be differentiated into two different functional properties depending on whether the austenite ↔ martensite transformation is induced thermally or by applied stress. Thermally induced transformation enables the shape memory effect (SME) while the stress induced transformation leads to pseudoelasticity (PE) (a.k.a. superelasticity) [6, 16, 17]. The thermomechanical response of the NiTi SMA largely depends on temperature. As shown in Figure 8 [30], during cyclic tensile testing the test temperature has a large effect on the material performance. More

specifically, the SME can be utilized if the material is in the martensite phase and PE can be utilized if the material is in the austenite phase; illustrated in the stress-temperature dependence plot of Figure 9 [33]. The temperatures which determine current phase of the material are called the phase transformation temperatures. The martensite start (M_s) and austenite start (A_s) temperatures represent the temperature at which the austenite → martensite or martensite → austenite phase transformations begin, respectively. The martensite finish (M_f) and austenite finish (A_f) represent the temperatures at which the respective phase transformation is completed. The SME can be observed in Figure 8 (a – e) [30] where the temperature is less than M_f and the NiTi alloy is in the martensite state. The residual strain observed in the tensile curves of Figure 8 (a – e) can therefore be recovered by heating the specimen to a temperature above A_f [30]. Pseudoelasticity can be observed in the tensile curves shown in Figure 8 (j – l) [30] where the test temperature is just above A_f. In this region large amounts of strain are possible with complete recovery upon unloading. Miyazaki et al. [34] found that for single crystals, 10% recoverable strain was possible before permanent straining occurs. However, in polycrystals less strain (i.e. < 8%) is possible before permanent strain results [30]. Curves (f – i) of Figure 8 [30] represent a partial phase transformation region ($A_s < T < M_f$) where the material will possess both SME and PE to a certain degree. As the test temperature is increased further above A_f, as shown in Figure 8 (m – p) [30], perfect PE no longer occurs and permanent strain results. This temperature at which the stress for permanent slip becomes lower than the stress to induce SIM is termed 'M_d' and is identified in Figure 9.

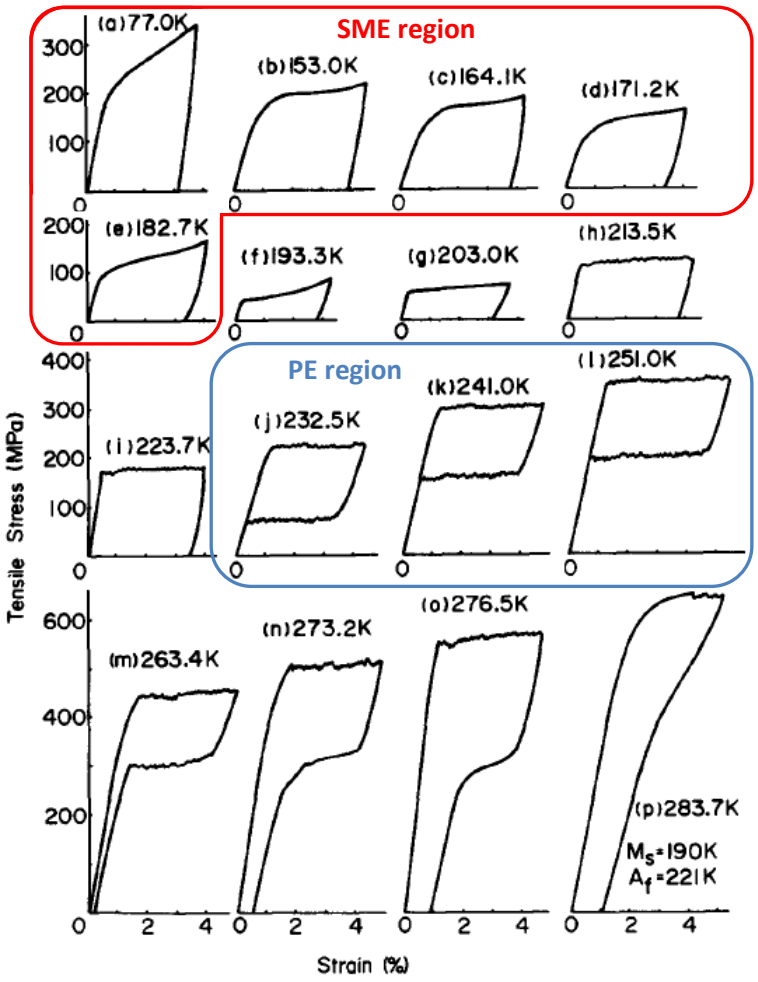

Figure 8: Cyclic tensile testing performed on Ti – 50.6 at. % Ni material with increasing test temperatures. Shape memory effect temperature range highlighted in red. Pseudoelastic temperature range highlighted in blue. Adapted figure from [30]

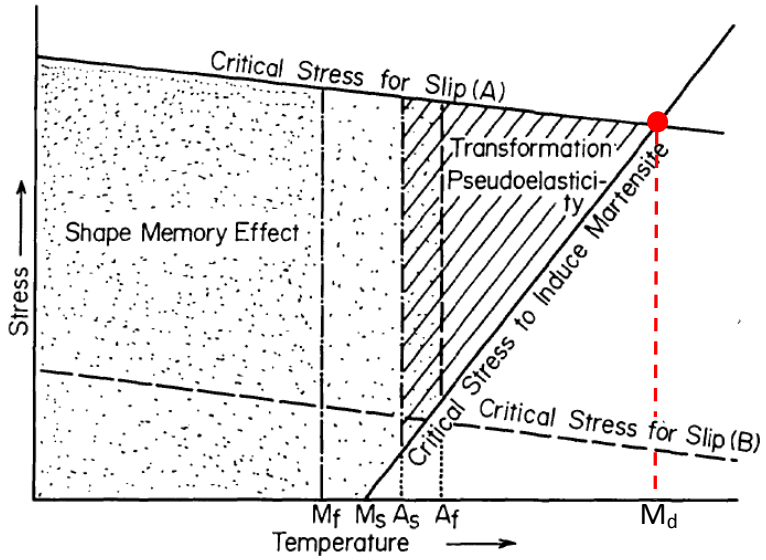

Figure 9: Stress-temperature dependence of NiTi SMAs for exhibiting SME or PE. Adapted figure from [33]

2.2.1. Thermally induced phase transformation and the shape memory effect

As discussed above, when in the martensite phase (i.e. $T < M_f$) NiTi SMAs can exhibit SME by thermally inducing phase transformations. There are two common methods for characterizing the thermal response of SMAs. The first method utilizes the change in electrical resistance brought about by changes in the crystal structure following a phase change [35]. The second method, and the method used in this work, is measuring heat flow during phase changes via the thermoanalytical DSC technique. Using either of these techniques the M_s, M_f, A_s, and A_f (including R_s and R_f, if R-phase exists) phase transformation temperatures can be identified. A typical DSC plot for a NiTi alloy is presented in Figure 10 where the transformation temperatures have been identified and therefore describe the thermal response of the specific alloy. The transformation temperatures are found by finding the intercept of the tangents to the transformation peak and base line, as per the ASTM F2004-05 standard. A distinct hysteresis in the phase transformation temperatures when transforming from martensite to austenite opposed to from austenite to martensite is observed in Figure 10. This hysteresis results from internal friction and defects in the crystal structure. Hysteresis is largely affected by composition, processing history, and the stress state of the particular component [26, 36, 37].

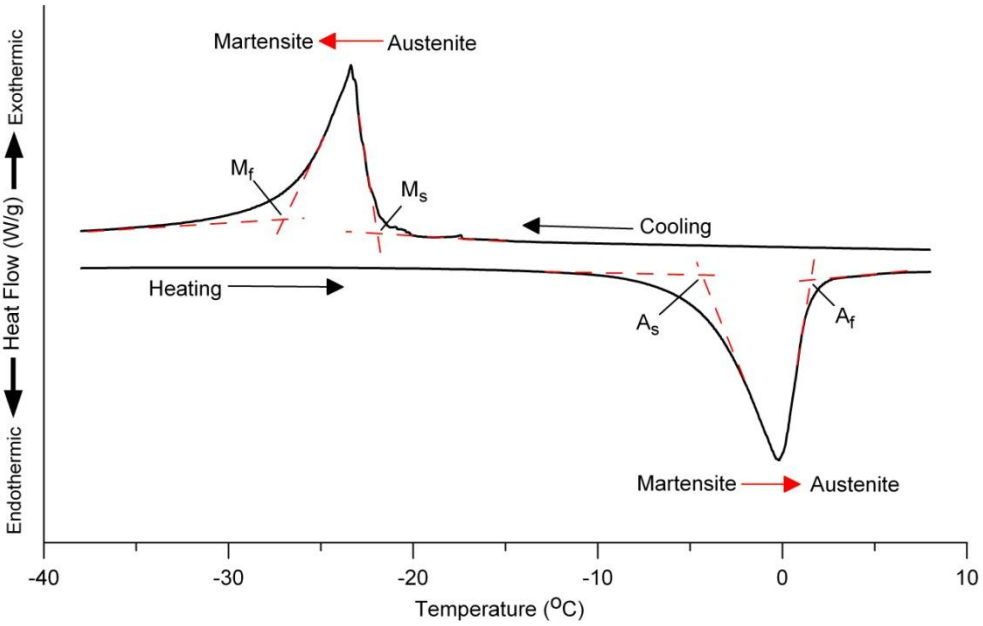

Figure 10: Typical DSC plot for an annealed NiTi alloy. Phase transformation temperature identified by taking tangents of the phase change peaks and the base line.

The SME refers to the ability of a SMA to undergo a certain degree of deformation and subsequently recover its original shape upon heating above A_f. The remembered shape is trained by a technique called shape-setting where the material is held in a fixed shape during a heat treatment protocol. The SME is illustrated in Figure 11 which shows the state of the crystal structure throughout the SME process. As illustrated in Figure 11 a), the deformation of martensite is accommodated through reversible detwinning of the crystal lattice. This deformation proceeds through twin boundary motion where less preferred martensite variants are converted to the most favorable variant under the current stress condition, until only a single variant exists [4, 38]. The deformation of martensite is also illustrated in Figure 11 b) moving from point A to point B on the stress-strain-temperature plot. In the early stages of the deformation of martensite, an elastic region is observed before the martensite detwinning stress (σ_m) is reached where the stress remains almost constant. This constant stress region is followed by the elastic straining of the fully detwinned structure. Once the material is in the deformed state and the stress has been unloaded, heating to a temperature above A_s will cause the detwinned martensite to begin transforming into austenite. This transformation of the crystal structure translates into the recovery of the original trained shape on the macroscopic scale once the temperature reaches above A_f. This transformation is illustrated in Figure 11 b) moving from B to C. The deformed crystal structure remembers its original orientation because of the lattice correspondence [4]. When the temperature is returned to below M_f the austenite structure changes back to martensite (i.e. A → B in Figure 11) and

the cycle can be repeated. During this phase change from austenite back to martensite upon cooling no macroscopic shape change is observed (Figure 11 a)) due to self-accommodation. Self-accommodation is the removal of the elastic strain resulting from martensitic transformation through twinning, where multiple variants form to relieve strain on the microscopic scale [39]. Often in application, a biasing mechanism is required to deform the martensite structure to allow for continuous SME (i.e. actuation). This can be done for example by storing energy via a biasing spring during the martensite to austenite transformation (i.e. shape change). Therefore, upon transforming back from austenite to martensite the stored energy in the spring deforms the martensite (A → B, Figure 11) allowing for continuous SME deployment; this concept is discussed in more detail in Chapters 4 and 5.

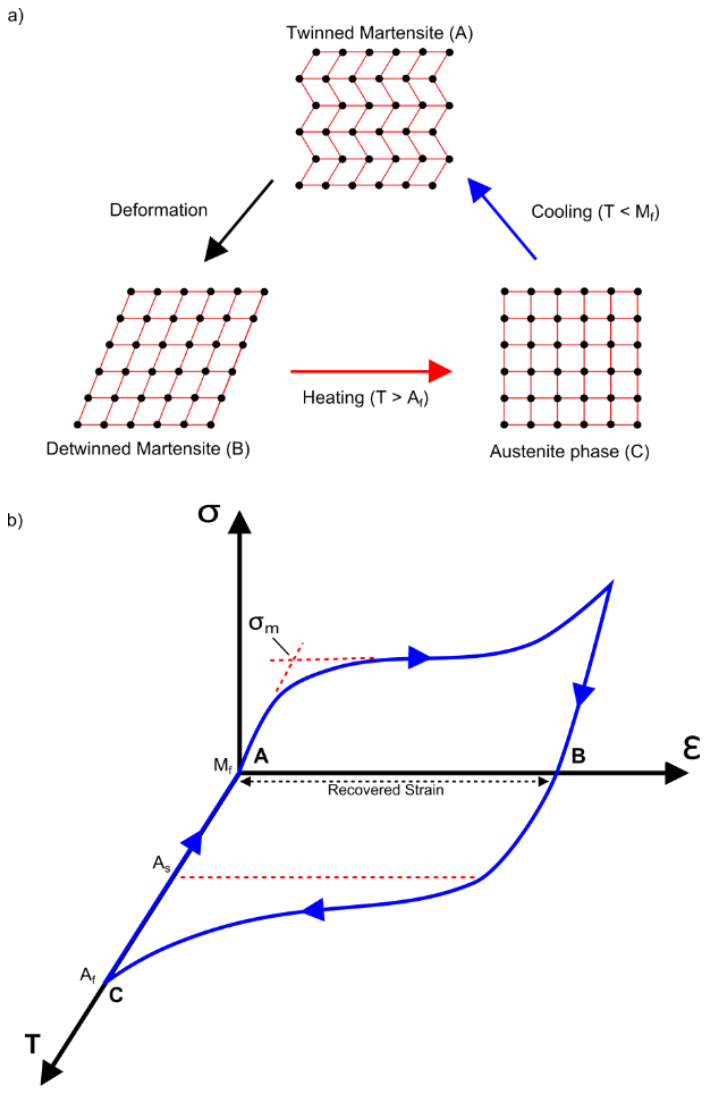

Figure 11: Illustration of the shape memory effect. a) Response of the NiTi crystal structure during deformation, heating and then cooling. b) Stress-strain-temperature response during SME [17]

2.2.2. Stress induced phase transformation and pseudoelasticity

When a NiTi SMA is in the austenite phase (i.e. $T > A_f$) PE is possible by stress induced phase transformation. The product of straining the austenite phase is called stress induced martensite (SIM). It is however important to note that in order for SIM to be produced the critical stress to induce martensite (σ_{SIM}) must be below the critical stress for slip as illustrated in Figure 9 [33]. A typical solutionized NiTi material cannot exhibit PE due to the yield stress being lower than that of σ_{SIM} (i.e. critical stress for slip (B) condition in Figure 9). Therefore, strengthening of NiTi alloys is necessary in order to increase the critical stress for slip above σ_{SIM} (i.e. critical stress for slip (A) condition in Figure 9). Typical strengthening protocol for NiTi alloys includes both strain hardening and precipitation hardening. Cold work of greater than 25 % [40] coupled with heat treatment at temperatures between 623 and 773 K (350 – 500 °C) is commonly quoted as an ideal protocol for creating PE NiTi SMAs [4]. This thermomechanical processing protocol was designed to precipitate harden the NiTi lattice via coherent Ni_4Ti_3 IMCs [41].

Pseudoelastic behaviour of SMAs is usually characterized through tensile testing as illustrated in Figure 12. A typical cyclic tensile curve, as illustrated in Figure 12 b), can be broken into several different segments. During initial loading the austenite phase exhibits elastic deformation (A – B) up until σ_{SIM} is reached. Once σ_{SIM} has been reached an isostress condition is observed (B – C) as the cubic austenite structure shears into detwinned SIM, followed by the elastic deformation of the detwinned SIM structure (C – D). A serrated appearance often is observed during the isostress PE region (B – C) (Figure 8) which is attributed to Lüders-like deformation, where strain bands propagate across the gauge length of the loaded tensile specimen [42, 43]. Just as for the thermally induced phase transformation during the SME, the formation of SIM is reversible. During unloading (D – A) elastic strain is recovered and the SIM transforms back into the parent austenite phase. Note that the recovery stress (σ_r) is lower than σ_{SIM}. Similar to the hysteresis observed in the thermally induced SME, the hysteresis in PE again arises from internal friction and defects in the crystal structure. Up to 8 % recoverable PE strain is possible in polycrystalline NiTi material [44] however, if loading continues past 8 % strain permanent plastic deformation of the SIM will occur [30]. Texture plays a large role in the ability of the NiTi specimen to fully recover strain. Perfect PE (i.e. 100 % recovery of strain) may not be possible due to the yielding of unfavorably oriented grains [45].

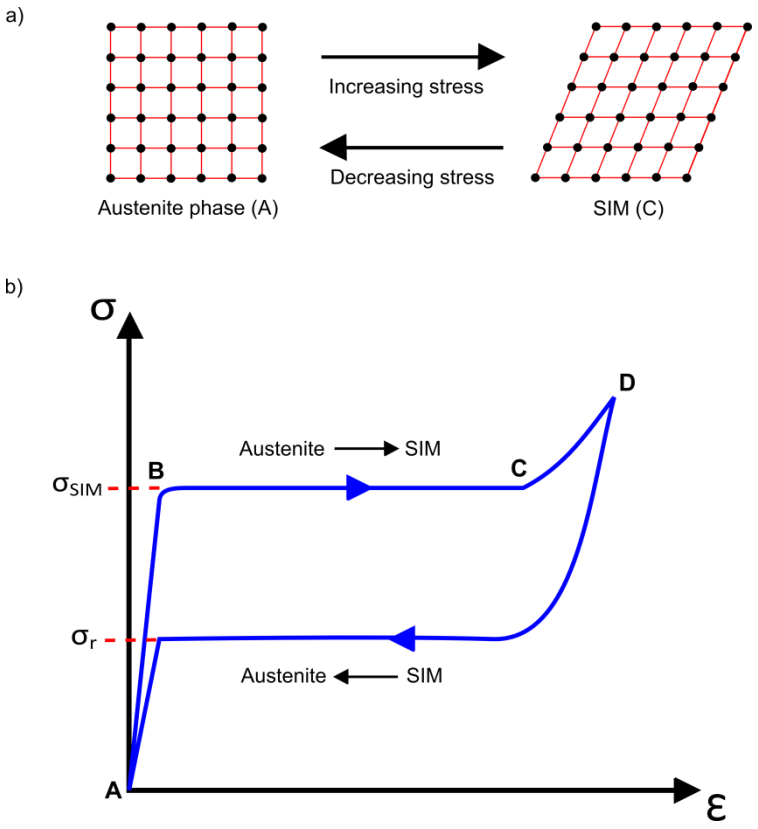

Figure 12: Illustration of pseudoelasticity. a) Response of the NiTi crystal structure to stress. b) Typical stress strain curve for a PE NiTi SMA

The PE properties are largely affected by the temperature of the NiTi SMA where, σ_{SIM} and σ_r increase with temperature; previously shown in Figure 8 [30]. As the test temperature increases above A_f the stress required to create SIM also increases due to an increase in the stability of the austenite phase. This increase in σ_{SIM} (and σ_r) has been observed to be linear as shown in Figure 13 and follows a Clausius-Clapeyron relation [30, 46, 47]. The Clausius-Clapeyron relation is given in equation (1) [46]:

$$\frac{d\sigma}{dT} = \frac{-\Delta H}{T\varepsilon_0}$$

where, $d\sigma$ is the change in σ_{SIM}, dT is the change in test temperature, ΔH is the latent heat of transformation (eg. obtained from DSC analysis), and ε_0 is the transformational strain. The right side of equation (1) therefore is the stress rate which is typically between 3 and 20 MPa/°C depending on the processing history of the NiTi material [46]. This highlights the importance of understanding the material behaviour at the in-service temperature of a particular SMA device. For example, a SMA medical device in the mouth such as, an orthodontic arch wire will be at 35 °C however, if the same alloy is used for a stent implanted in an artery, the stent will be at 37 °C and will have 6 – 40 MPa greater σ_{SIM}.

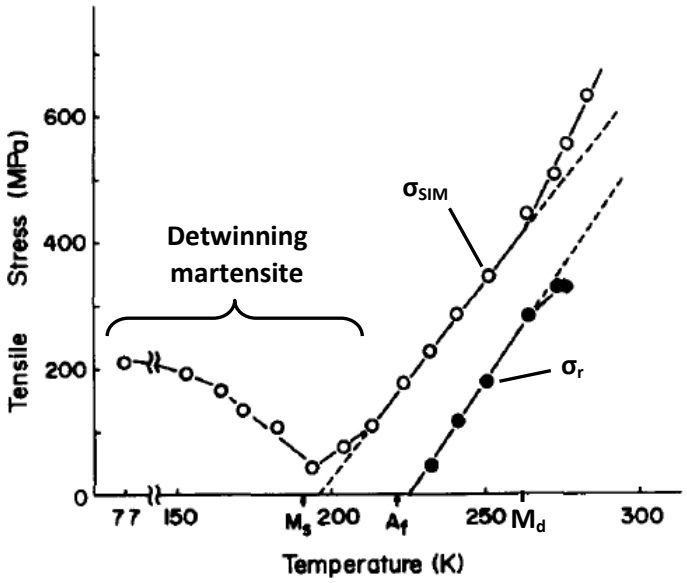

Figure 13: Plateau stress versus temperature plot. Dashed lines represent linear Clausius-Clapeyron relation between σ_{SIM} (empty circles) and σ_r (solid circles) and temperature (i.e. when $T > A_f$). Below A_f detwinning of martensite occurs and above M_d plastic deformation of austenite occurs resulting in deviation from the Clausius-Clapeyron relation. Adapted figure from [30]

2.2.3. Effects of composition and ageing treatment

The functional properties of NiTi SMAs are extremely sensitive to changes in composition. This is largely due to the phase transformation temperatures being extremely sensitive to the mole fraction of Ni, as shown by Tang [48] and Frenzel et al. [12] in Figure 14. A slight increase in Ni composition above 50 at.% drastically decreases the transformation temperature. However, on the Ti-rich side the transformation temperatures remain almost constant. This is due to the insolubility of Ti below 50 at.% composition (Figure 1) making Ti-rich solid solutions impossible. Therefore, Ti-rich alloys behave the same as equiatomic NiTi alloys with an M_s temperature of approximately 338 K (65°C) [4, 48]. Otsuka and Ren [4] state that controlling the composition of the NiTi alloy is the most effective way to achieve application specific functional properties. However, controlling material composition and experimentally quantifying compositions with the required precision is difficult [48, 49]. Also, any internal defects in the material created during manufacture can alter the transformation temperatures; discussed in more detail in following sections. In fact the deviation of experimental data from Tang's [48] experimental model shown in Figure 14a) have been attributed to such material condition uncertainties and were the basis of the improved model developed by Frenzel et al. [12] shown in Figure 14b). These issues in material manufacturing and in obtaining data from completely characterized material are areas in which laser processing will enable significant contributions to NiTi research; discussed in Chapter 5.

Post processing heat treatments which produce Ni-rich precipitates have also been proven as an effective way to modify material functional properties. The precipitation of Ni-rich precipitates depletes the NiTi matrix of Ni causing significant increases in transformation temperatures as shown in the time-temperature-transformation diagram developed by Pelton et al.; Figure 15 [46]. In this work Pelton et al. [46] also shows the relation between the A_f transformation temperature and σ_{SIM} which as discussed earlier follows a Clausius-Clapeyron relation (equation 1). An increased in the A_f transformation temperature caused by increasing Ni depletion of the matrix leads to a decrease in σ_{SIM} (i.e. and σ_r) due to a reduction in the thermodynamic stability of the parent austenite phase [50]. It is important to recall that the precipitation of Ni_4Ti_3 precipitates also leads to the intermediate R-phase martensitic transformation; discussed above in section 2.1.1.

It can be deduced that lower Ni:Ti ratios leads to increased transformation temperatures for SME and decreased PE stresses as will be discussed in detail in subsequent sections. Hence, the importance of material composition and processing history in achieving application specific properties is evident. The mechanism behind the compositional effects on the functional properties has been linked to a softening in the elastic constants c' and c_{44} as the temperature is lowered towards the martensitic phase transformation temperature [4, 51]. It has been shown that there is a critical value of c' at which transformation takes place and this value is not sensitive to NiTi composition [52-55]. On the other hand, the elastic constants themselves are sensitive both to temperature and composition. In fact, c' and c_{44} have been shown to be highly sensitive to composition in martensitic alloys due to changes in lattice dynamic properties (i.e. phonon dispersion) [56]. Therefore, in order to keep the critical values of c' and c_{44} constant at martensite transformation, a change in composition must be accompanied by a change in transformation temperature [51]. In other words, the magnitude of the energy barrier for martensite transformation decreases with increasing Ni content, leading to lower phase transformation temperatures and hysteresis [12]. Lattice miss-match between the parent and product phases dictates the elastic strain energy at the austenite/martensite interface, modifying the energy barrier for phase transformation [12].

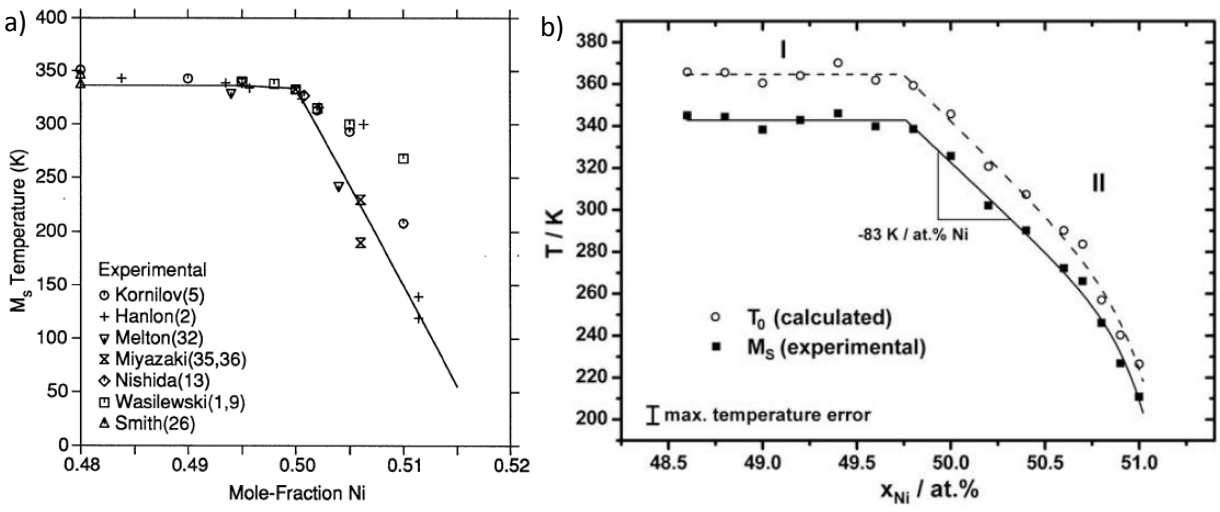

Figure 14: Relation between mole-fraction of Ni and M_s temperature in binary NiTi SMAs a) as proposed by Tang [48] and b) as proposed by Frenzel et al. [12]. Figures taken from [12, 48].

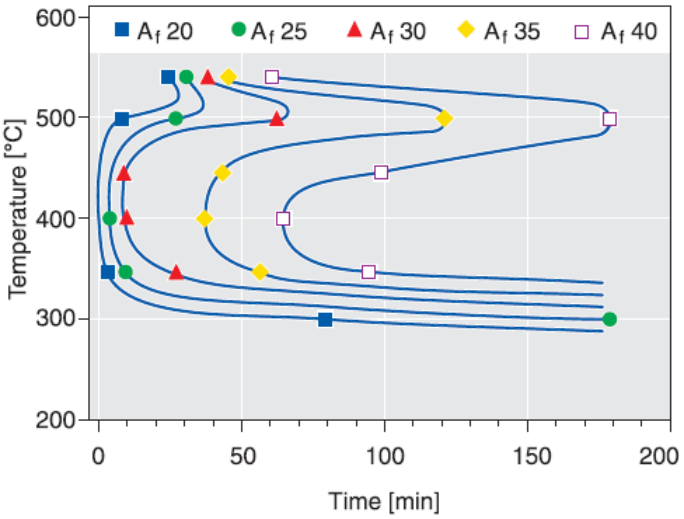

Figure 15: Time-temperature-transformation (TTT) diagram showing relation between heat treatment temperature, time, and A_f transformation temperatures. Figure taken from [46]

2.3. Traditional thermomechanical processing techniques

Traditionally NiTi SMAs are fabricated using vacuum induction melting (VIM) or vacuum arc re-melting (VAR) technologies followed by hot and cold forming processes where the ingot is shaped into sheet, wires, tubes, etc. [49]. Once the NiTi material has been formed into its final geometry, ageing heat treatments are applied to fine tune the functional properties of the bulk material to that of a specific application [47]; as discussed in section 2.2.3. Typically, commercial NiTi components require ±5 °C which means a composition tolerance of 0.05 at.% is necessary [49]. Therefore the melting processes must be controlled very precisely. The ability to measure composition with the necessary accuracy of

less than ± 1.0 at.% also poses challenges and as a result NiTi material manufacturers provide nominal compositions only. Differential scanning calorimetry analysis is therefore usually used as an indirect quality check [49] given the linear trend in transformation temperatures with respect to molar mass of Ni, shown in Figure 14 [12, 48]. A great deal of complexity comes into play when considering the drastic changes that occur not only to the structural properties but also the functional SME and PE properties during each processing step before arriving at the final net-shape. Since extensive literature exists on these topics, readers are encouraged to reference [4, 6, 16] for a complete review on this topic. General processing concepts will be discussed here in order to follow the process – structure – performance study in Chapter 5.

In the as-cast state NiTi SMAs have low yield stress and random crystal texture [57]. This leads to both poor mechanical and functional properties of the SMA. As highlighted in Figure 9, a certain yield stress is necessary to prevent dislocation motion allowing for more perfect SME and PE properties; meaning no buildup of residual strain [33]. Typically NiTi alloys are strengthened via several different mechanisms which include grain refinement [58], strain-hardening [50], and precipitation hardening (i.e. Ni_4Ti_3 precipitates) [46]. Combinations of hot working, cold working, and annealing/aging heat treatments are usually applied during the manufacture of a specific component [4]. It has been shown that for Ni-rich alloys a combination of strain hardening and heat treatment is best for increasing the critical stress to induce slip (i.e. yield strength), as summarized in detail by Otsuka and Ren [4]. The resulting combination of strain-hardening and precipitation hardening allows for more perfect SME and PE properties, larger ranges of temperatures at which PE can occur [4], and more stable performance in low cycle experiments [35]. With each processing step, the phase transformation characteristics of the NiTi SMA are changing. Therefore, the phase transformation temperatures and hence, SME and PE properties discussed in sections 2.2.1. and 2.2.2. are also altered. For example, the Differential Thermal Analysis (DTA) results in Figure 16 [59] clearly show the effects of deformation and different annealing temperatures. The introduction of dislocations into the NiTi matrix decreases and broadens phase transformation temperatures [59, 60], introduces R-phase as discussed in section 2.1.1., and can even prevent phase transformation from occurring all together in heavily cold worked materials, reducing heat of transformation [60]. Subsequent heat treatments again decrease the width of the transformation peaks while shifting them to higher temperatures (Figure 16). Depending on the heat treatment temperatures R-phase may also remain as identified by the presence of two phase transformation peaks (Figure 16).

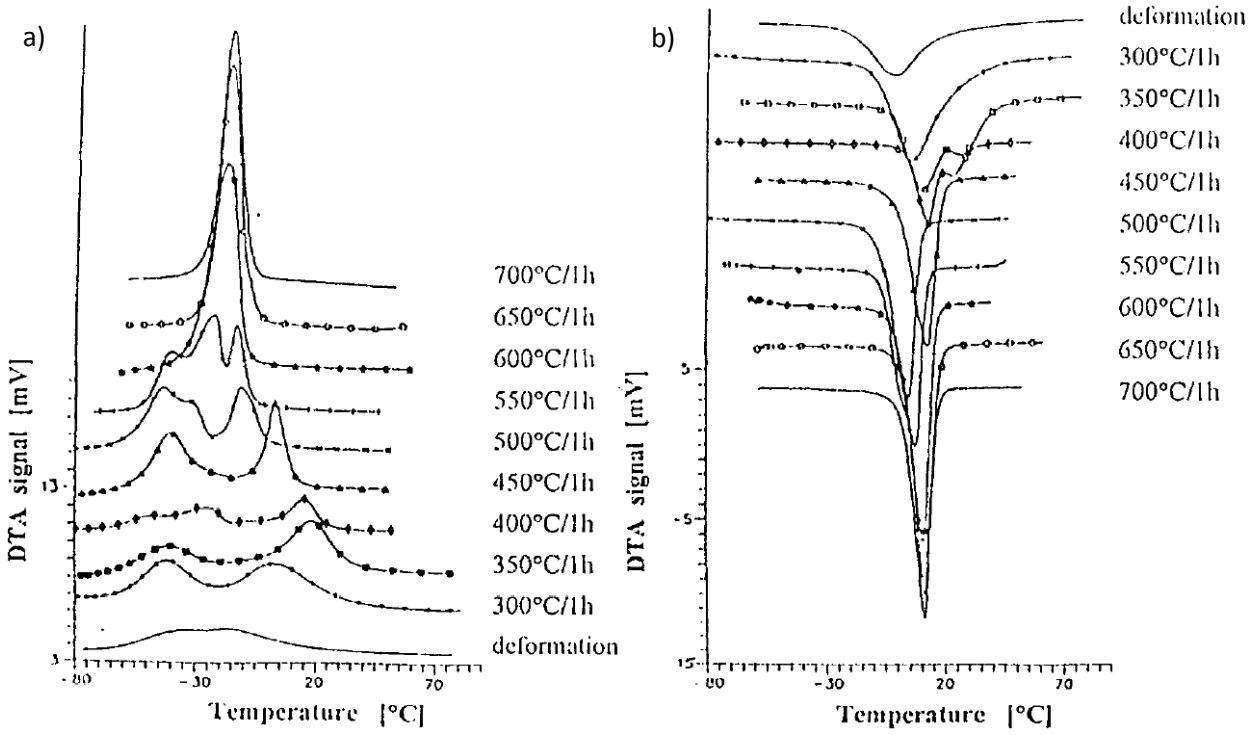

Figure 16: DTA results for deformed Ti-50.6 at. % Ni alloy when subject to subsequent heat treatments. a) cooling curves, b) heating curves. Figures taken from [59]

Finally, crystallographic texture that forms in the component creates anisotropy in martensite detwinning and SIM formation. This can lead to phenomena such as higher residual strains because martensite variants must rearrange themselves at the expense of dislocation motion to accommodate for the applied stress and also drastically different deformation behaviour. The classic example of large difference in PE behaviour from a NiTi SMA loaded in tension or compression, as shown in Figure 17, highlights the importance of texture with respect to applied stress [57]. It was observed that larger PE strains can be achieved when stressed in the direction of ⟨111⟩ texture and the slope of the plateau remains flat [57].

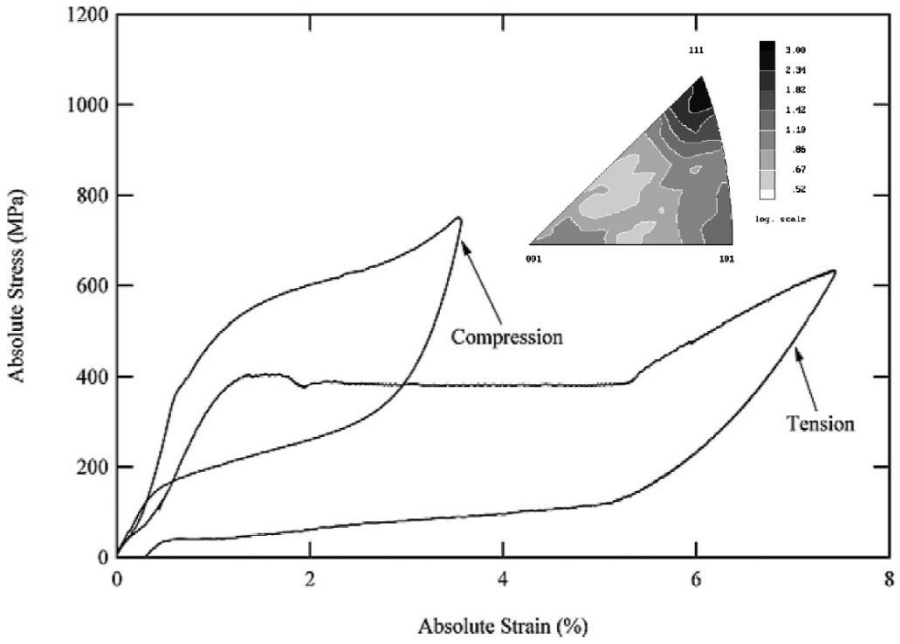

Figure 17: Tensile and compression tests for hot rolled Ti-50.9 at. % Ni SMA having strong ⟨111⟩ texture on the axis of applied stress. Figure adapted from [57]

2.4. Novel processing protocol for enhanced functionality

Traditional SMA fabrication technologies can be performance limiting since they produce monolithic components which consist of only a single set of phase transformation characteristics. The whole component will therefore have the same transformation temperatures and PE properties, limiting its functionality. A novel material processing protocol is therefore required to overcome these challenges to enable further innovation and application.

Many methods have been presented to locally control the properties of NiTi based components, improving functionality and increasing design flexibility. Specific methods previously attempted included, direct electric resistance heat treatment (DERHT) [61, 62], direct hot air heat treatment (DHAHT) [61], powder metallurgy (PM) [63-66], gradient annealing [67], joining of multiple alloys [68], and more recently novel laser processes [69-72]. All of these techniques aim to enable designs that utilize more than one set of functional properties in a monolithic component. However, inherent processing issues restricted their widespread application in the current state of the art. For example, local heat treatment methods can only be applied to simple geometries, are time intensive, and provide a lack of resolution in functional properties [61, 62, 67, 69]. Powder metallurgy methods exhibited issues with porosity, poor surface finish and composition inhomogeneity leading to undesirable IMC formation [64-66]. Joining of multiple alloys was shown to be relatively effective for simple devices [68]. However,

challenges associated with joining such as dissimilar SMAs, IMC formation, large freezing range, and more complex joint geometries again limit application [49]. Laser technologies which locally modify composition and/or microstructure [69-73] offer the most promising solutions to creating novel NiTi devices with improved functionality. The ability to locally process, high speeds, low heat input, high cooling rate, and high quality inherent of laser processes, make them excellent candidates for processing SMAs. Laser processes will therefore be discussed in more detail in the following section and will be the platform technology of studies detailed in Chapters 4 through 6.

2.5. Laser processing

Traditionally laser processing of NiTi SMAs was largely limited to laser welding [68, 74-79]. Due to the high sensitivity of functional properties to thermal events, the low heat input and high cooling rate characteristics of laser welding were found to be ideal [74]. However, the means of utilizing laser processing methods for improving the performance or enhancing the functionality of traditional SMA materials has only very recently gained a lot of momentum [69-73, 80, 81]. New technologies such as the patented multiple memory material (MMM) technology [73] and laser annealing [69] have great promise to revolutionize the way we process and design SMA devices.

Remarkably, in the last two years the effectiveness of laser processing has been proven through the development and testing of a two way actuator [69] and creation of a multiple memory microgripper [71] detailed in Figure 18 and Figure 19 respectively. Also, improved NiTi functional properties were achieved through the synergistic approach of laser processing while locally alloying with Cu [70], detailed in Figure 20. In these novel laser processing technologies, rapid changes in microstructure and/or local chemical composition have proven very effective in fine tuning the functional properties of NiTi SMAs. They are however unprecedented techniques and there are several uncertainties that must be first be addressed before they can be applied to their full potential.

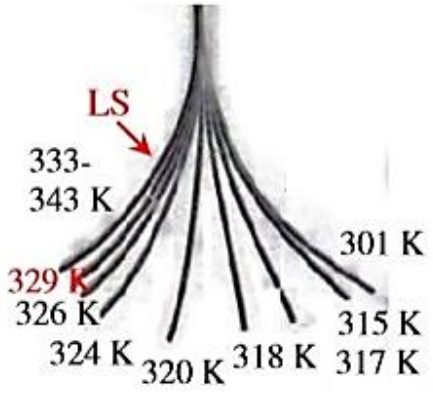

Figure 18: Unique two way memory of functionally graded strip utilizing laser annealing. Arrow indicates laser processed side of strip (LS). Adapted figure from [69]

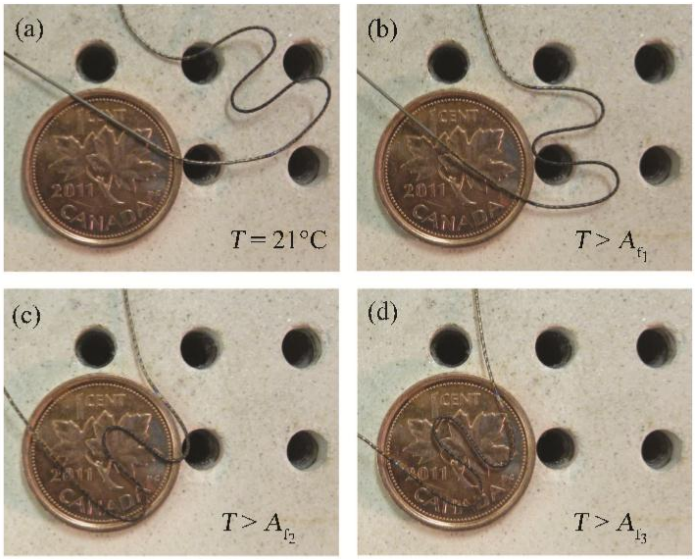

Figure 19: Multiple memory micro-gripper created by MMM laser processing. a) → d) increasing temperature via resistive heating. Adapted figure from [71]

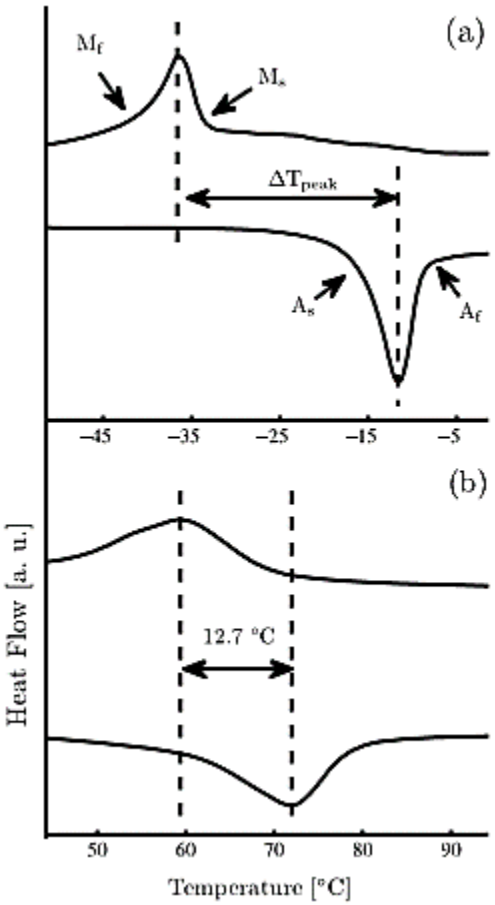

Figure 20: Locally reduced phase transformation hysteresis with laser annealing Cu into a NiTi SMA. a) base material DSC curve, b) laser alloyed NiTiCu material DSC curve showing reduced hysteresis. Adapted figure from [70]

2.5.1. Effects of laser processing on mechanical and functional properties

It is clear that the yield strength and working strains are reduced following laser processing [82-87]. The effects of past material treatments such as cold work, precipitation hardening, etc. are lost following the thermal cycles induced by the laser process [82, 84, 87]. Only limited success has been realized from post-laser processing techniques in modifying or restoring material properties [83, 88, 89] and in each of these studies only aging heat treatments were explored. More fundamental work must be done before laser technologies can be applied to their full potential with necessary confidence.

In addition to poor structural properties, the unique functional properties of SMAs pose more complex effects of laser processing which are not well understood in literature. There is much confusion on what happens to the functional properties of the alloy after laser processing where several studies seem to contradict each other. For example, laser processing has been shown to decrease the phase transformation temperatures that are critical to the SME and PE functional properties in studies by Hsu

et al. [78] and Chan et al. [89], however other studies have shown either no change [83, 87, 90], increases in transformation temperatures [74, 84, 91-93], and/or removal of R-phase transformation [84, 87]. Clarification of the effects of processing on the functional properties and identification of the mechanisms responsible must therefore also occur.

2.6. Laser induced vaporization

In this research study a laser induced vaporization protocol [73] will be utilized to improve our understanding of the effects of laser processing on the functional properties of NiTi SMAs as well as contribute fundamental research in the area of smart materials. Therefore, this section provides a detailed review of the current state of understanding regarding this novel processing method and the underlying mechanism behind the technology. This chapter is based off of a study by Khan et al. [72].

2.6.1. The vaporization concept

Composition changes induced by vaporization using high power density processing methods (eg. laser beam, electron beam, etc.) is well documented in literature [94-102]. Prior studies have concluded that local loss of elemental constituents can be detrimental to the properties of a bulk material. For example, it has been reported that the loss of certain alloying elements during laser processing was responsible for reduction in solid solution strengthening in Al alloys (i.e. due to loss of Mg) [95, 98] or decreased corrosion resistance in stainless steels (i.e. due to loss of Cr) [97, 99-102]. However, by controlling elemental loss during laser processing, the local properties of an alloy can theoretically be precisely tailored for that of a specific application. NiTi SMAs are a prime example of a group of materials that are extremely sensitive to change in composition, as discussed in section 2.2.3., where the advantages of elemental loss during processing can be realized. Similarly, transformation temperatures and temperature/stress hysteresis in ternary (or quaternary, etc.) NiTi systems and other SMAs, such as Cu-Al alloys, were also found to be highly composition dependent [103-110]. A laser induced vaporization protocol could therefore be used for quickly modifying the local functional properties of monolithic SMA components [73, 72].

2.6.2. Selective vaporization of elemental constituents

To apply this novel vaporization protocol to NiTi SMAs the relative vaporization flux of each elemental constituent (i.e. Ni and Ti) must be considered to aid in predicting the change in composition. The relative loss of elemental constituents during laser processing is determined largely by their volatility [56, 95-102]. More specifically, the pressure gradient has been shown to have the largest effect on

vaporization flux J_i of each element i present in the molten pool during laser processing as shown in equation (2) [101, 102]:

$$J_i = J_{P,i} + J_{C,i}$$

where $J_{P,i} >> J_{C,i}$ and $J_{P,i}$ is given by equation (3) [102]:

$$J_{P,i} = a_i \frac{P_i^o}{P_L} \frac{M_i}{M_v} J_P$$

where a_i is the activity of alloying element i, P_i^o is the equilibrium vapor pressure of the element i over pure i, P_L is the summation of equilibrium vapor pressures of all alloying elements on the surface layer (Knudsen layer), M_i is the molecular weight of element i in the Knudsen layer, M_v is the mean molecular weight of vaporized species, and J_P is the total vaporization flux caused by the pressure gradient. Therefore, relative loss of elemental constituents can be approximated by calculating the vapor pressures of each element. Assuming ideal conditions at high temperatures, equilibrium vapor pressure of both Ni and Ti is calculated over the alloy mixture of the molten pool via equation (4): [100, 101]

$$\mathrm{P_i} = \mathrm{X_i P_i^o}$$

where X_i is the mole fraction of the element i. The equilibrium pressure P_i^o of each alloying element was calculated with respect to temperature using equation (5): [111]

$$\log_{10}(\mathrm{P_i^o}) = \mathrm{A} + \frac{\mathrm{B}}{\mathrm{T}} + \mathrm{C}\log_{10}(\mathrm{T}) + \mathrm{DT} + \mathrm{ET}^2$$

where *A*,*B*,*C*,*D* and *E* are constant coefficients and *T* refers to temperature. The corresponding coefficients for Ni and Ti are provided in Table 3 [111].

Table 3: Constant coefficients for calculation of equilibrium vapor pressure (P_i^o) of Ni and Ti [111]

	A	B	C	D	E
Ni	-214.3	-3.52E+03	7.49E+01	-1.80E-02	1.51E-06
Ti	-194.8742	-8.27E+03	6.83E+01	-1.73E-02	1.55E-06

Calculated vapor pressures of Ni and Ti over an equiatomic NiTi alloy as a function of temperature are presented in Figure 21 [72]. Significant differences in vapor pressures were observed between the two elemental constituents, with Ni being substantially larger over the plotted temperature range. Hence,

the vaporization flux of Ni can be expected to be larger than that of Ti during laser processing of a near equiatomic NiTi SMA.

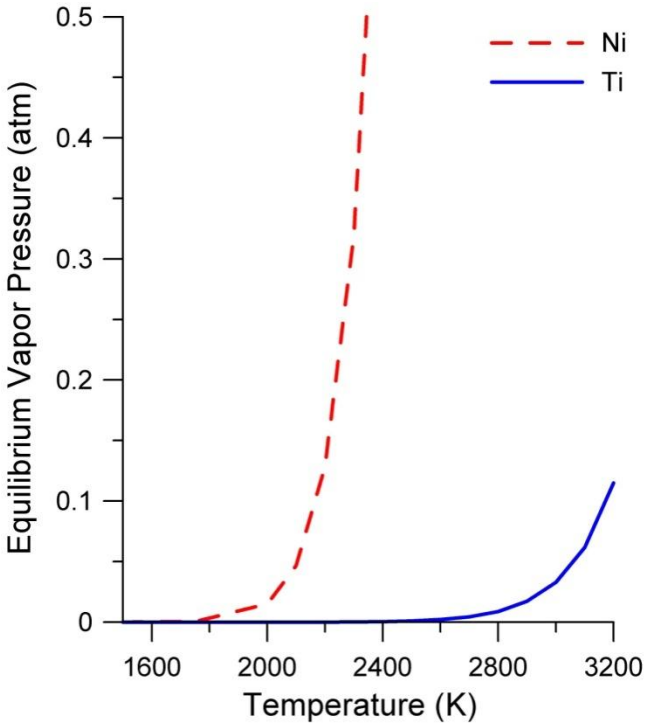

Figure 21: Nickel and Titanium vapor pressures over an equiatomic NiTi mixture. Significantly higher vapor pressure of Nickel corresponds to a comparatively larger vaporization flux. Figure taken from [72].

2.6.3. Augmentation of transformation temperatures

A decrease in the Ni:Ti ratio translates to an increase in phase transformation temperatures as discussed in section 2.2.3. [48, 112-115]. Therefore, the anticipated loss of Ni following laser processing was expected to increase the phase transformation temperatures. This hypothesis agrees with results from the differential scanning calorimetry (DSC) analysis presented in Figure 22 [72]. After processing the NiTi alloy, a second set of transformation peaks appears at higher temperatures compared to those of the solutionized base metal. Furthermore, during pulsed Nd:YAG laser processing it has been shown that vaporization primarily occurs during the first few milliseconds of laser application, when utilizing the keyhole laser interaction mode [102]. Therefore, a compound effect resulted when using multiple pulses that maximized vaporization. Accordingly, transformation temperatures were found to increase with each additional laser pulse, identifying the possibility for high resolution through this laser processing protocol (Figure 22).

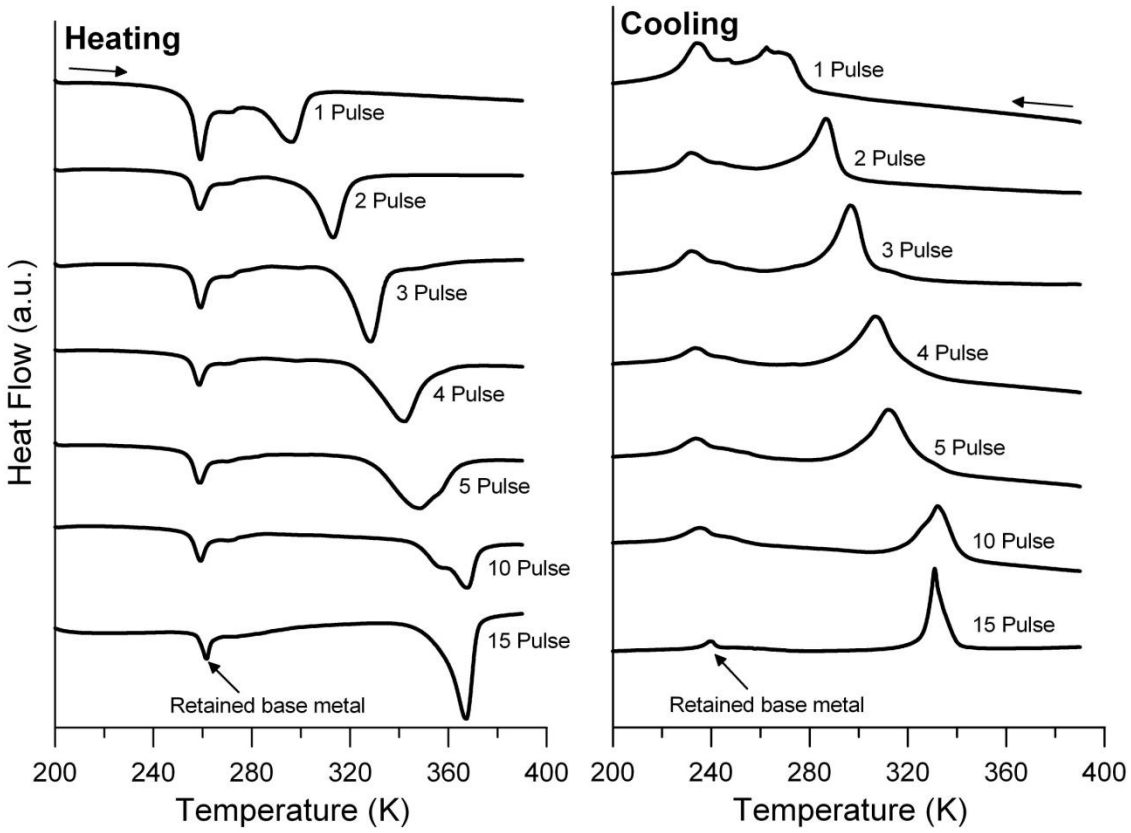

Figure 22: Thermo-analytical differential scanning calorimetry (DSC) analysis. Following laser processing of a Ti-50.7 at. % Ni alloy with 0.6 kW peak power and 30 ms pulse duration, a second set of phase transformation peaks were identified at higher temperatures. During heating, the endothermic B2 austenite peaks were measured. Similarly, the exothermic B19' martensite peaks were measured during cooling. Increasing the number of pulses caused a compound vaporization effect, raising the transformation temperatures with increasing number of pulses. Figure taken from [72].

Relative composition change of laser processed materials is highly dependent on a balance between the vaporization flux of elemental constituents and molten pool dilution [101, 102]. Effects of pulse duration on transformation temperatures therefore must be considered as shown in Figure 23 [72]. Using a laser power of 0.6 kW, increasing pulse duration increased DSC peak intensity. The more prominent transformation peaks are a result of an increase in the processed material to base metal volume ratio with increased pulse duration. Transformation temperatures of processed material decreased slightly (i.e. by < 20 °) with increasing pulse duration, as shown in Figure 24 [72]. Since vaporization flux is highest during the first few milliseconds of the laser pulse and decreases drastically with pulse duration [102], dilution of the molten pool caused by an increase in volume was likely the mechanism behind decreasing transformation temperatures with longer pulse durations. Hence, vaporization flux decreased and the pool volume increased with increased pulse duration, leading to smaller changes in final composition; consistent with literature [102].

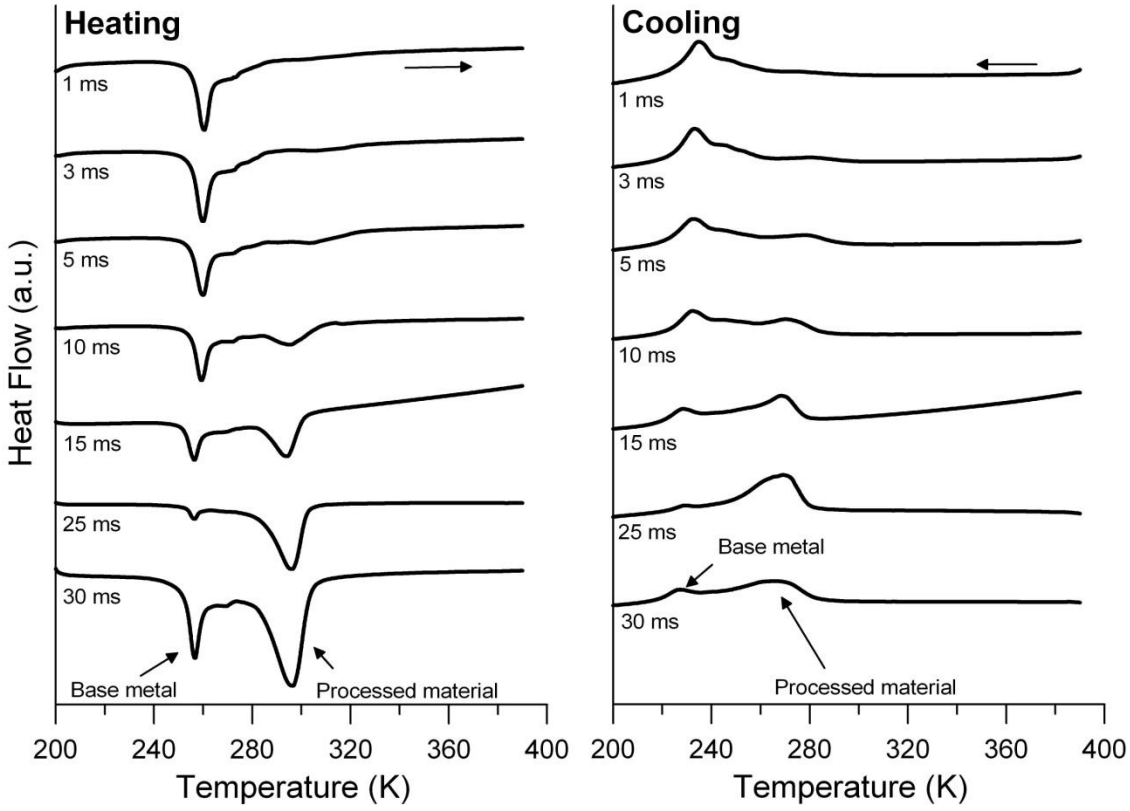

Figure 23: The effect of pulse duration on transformation temperatures as measured by DSC analysis. Less significant changes in transformation temperature of the processed region were observed with increasing pulse duration and a laser power of 0.6 kW compared to number of laser pulses. Figure taken from [72]

The effects of laser power on transformation temperatures are shown in Figure 24 [72]. Only a small decrease in transformation temperature (i.e. < 10 °) was observed when increasing laser power to 0.9 kW from 0.6 kW. Similar to the decrease in transformation temperatures with increasing pulse duration, increasing the laser power can also cause an increase in dilution of the molten pool leading to lower transformation temperatures.

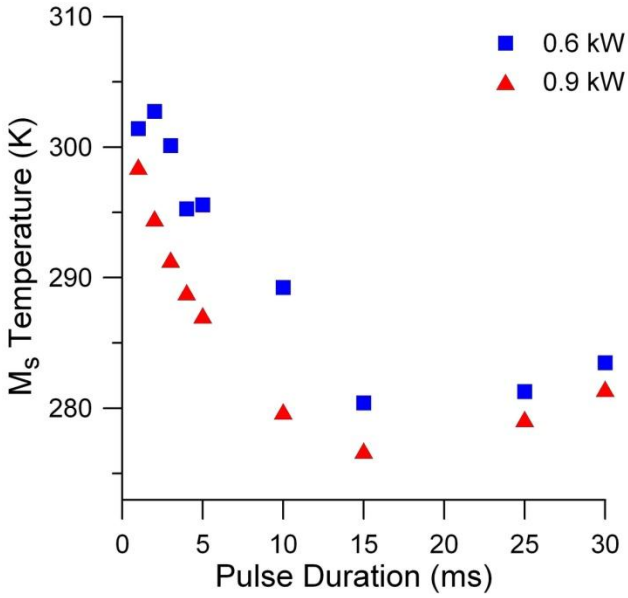

Figure 24: Effect of laser power on transformation temperatures. M_s temperature versus pulse duration for the 0.6 kW and 0.9 kW laser power conditions. Less than 10 K difference in transformation temperatures was observed between the 0.6 kW and 0.9 kW laser power conditions. Figure taken from [72]

2.6.4. Verification of the vaporization mechanism

Thus far thermoanalytical DSC analysis was shown to be a useful tool in identifying the effects of laser parameters on transformation temperatures. However, it is still necessary to definitively confirm that vaporization was in fact the primary mechanism at play. Khan et al. [72] provided evidence that composition change due to vaporization is in fact the mechanism responsible for the augmentation temperatures including: i) EDS line scan including the base metal and processed region (i.e. after 5 laser pulses), ii) EDS analysis performed on the captured plume produced during laser processing showed 75.5 at. % Ni and 24.5 at. % Ti; and iii) identification of the martensite phase in the processed region while the substrate remained in the austenite phase. However, EDS is typically only accurate to ± 1 at.% and the changes in composition realized due to vaporization will be an order of magnitude lower taking into account the relationship between the M_s temperature and Ni-composition of Δ 83 K/at. % Ni [12]. In addition to the absence of definitive composition measurement of pulsed laser processed material, there are also other possible mechanisms that can contribute to changes in transformation temperatures in NiTi alloys such as, contaminants (i.e. O and C), changes in dislocation density, and growth of Ni-rich precipitates; discussed in section 2.2.3. [1, 15, 103, 116]. More accurate composition measurement and in depth microstructural analysis must take place to better understand all of the mechanisms at play during this vaporization based protocol.

2.6.5. Multiple memory material proof of concept

Multiple memory materials fabricated using controlled constituent vaporization have great potential in aiding in the realization and development of novel SMA devices. Proof of concept was demonstrated by Khan et al. [72] through the local modification of the transformation temperatures in the NiTi component shown in Figure 25. Commercially available material that exhibits a single set of transformation temperatures (i.e. single shape memory) was locally processed, as shown in Figure 25a. Pulsed Nd:YAG laser processing at the annotated sites caused a localized increase in phase transformation temperatures while the phase transformation dynamics in the untreated regions remained unchanged. This increase in transformation temperatures allowed for a two-stage (i.e. two-memory) actuation through sequential heating of the specimen beyond the A_f temperatures of the base metal and the processed material, respectively. A schematic and photograph of the actuation process are shown in Figure 25b and 23c. At low temperatures the entire sample was in the martensitic phase and easily deformed (i.e. by detwinning) into a 'C-like' shape. Upon heating to a temperature greater than T_1, the bulk unprocessed base metal transforms to austenite and recovers its original shape, while the processed regions remain in the martensite phase. Subsequently, heating to above T_2 induces the transformation of the processed regions to austenite and the recovery of the second shape memory.

Although, proof of concept had been demonstrated for locally augmenting transformation temperatures via laser vaporization processing [71, 72] much research is still necessary to fully understand the effects of laser processing on the structural and functional properties of NiTi SMAs which are critical to their performance in application.

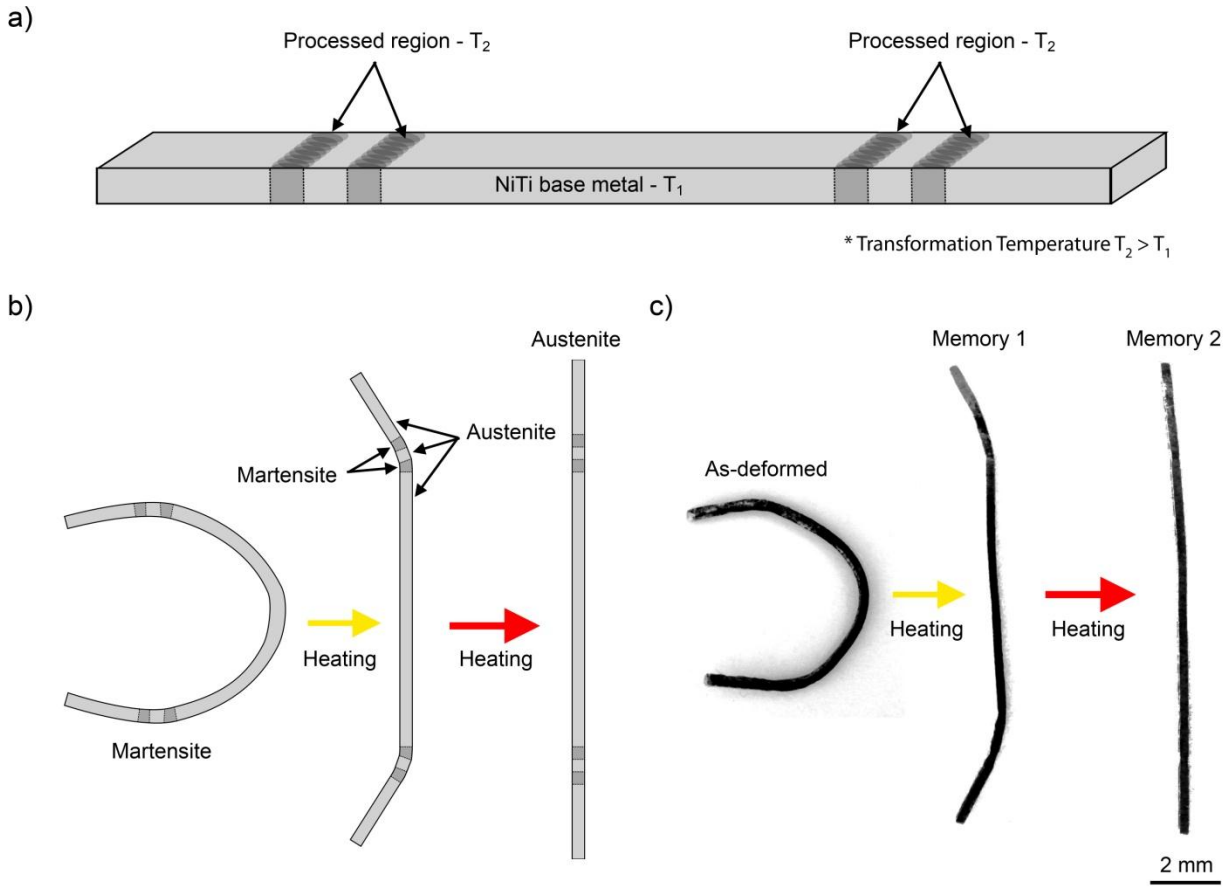

Figure 25: Multiple memory material proof of concept. a) Four select regions of a commercially available NiTi alloy were laser processed, increasing the phase transformation temperatures (Not to scale). b) Schematic demonstration of multiple actuations of the laser processed component. c) Actual images of processed component during different stages of actuation. After cooling below the martensite finish temperatures of both the processed region (T_2) and base metal (T_1) the component was deformed by detwinning in the martensite phase to a "C-like" shape. Upon heating past the austenite phase transformation temperatures of the base metal, the base metal recovered its shape while the processed region remains strained and in the martensite phase. Further heating past the austenite transformation temperatures of the processed regions lead to a second transformation and complete recovery of the original shape of the processed NiTi component. Hence, the monolithic component possessed two distinct shape memories after processing. Figure taken from [72]

2.7. Corrosion resistance and biocompatibility

The corrosion resistance and biocompatibility of NiTi alloys is attributed to the protective Ti oxide layer that forms on its surface. Due to the thermodynamic driving force (i.e. ΔG) Ti oxides dominate over Ni oxides on the surface of NiTi material, where ΔG of forming TiO_2 and NiO are -940 kJ/mol and -211.7 kJ/mol respectively [117]. Therefore, like other medical alloys such as Ti6Al4V and 316 stainless steel (SS), NiTi alloys possess a passive oxide layer on its surface which increase the corrosion breakdown potential and lower the release of harmful Ni ions. As shown by Wever et al. [118], NiTi alloy breakdown potential and current density identified through cyclic potentiodynamic corrosion testing, falls somewhere in between the Ti6Al4V and 316 SS materials depending on the surface characteristics; shown in Figure 26. Also, the Ni ion release from NiTi material when immersed in Hanks' solution was found to be high at first but dropped off quickly, eventually decreasing below detectable limits; shown in Figure 27 [118]. The unique nature of the NiTi surface stems from the near equiatomic ratio of Ni to Ti in the alloy. Depending on the previous processing history the surface species will contain different mixtures of Ti-based surface oxides, Ni-based oxides/hydroxides, and even elemental Ni [119, 120]. As a result, the corrosion performance and Ni ion release can vary quite significantly depending on the surface condition [119-121]. Different surface treatments such as mechanical polish, electropolish, chemical passivation, oxide building heat treatments, etc. are commonly applied which drastically affect biocompatibility [75, 120-122]. It is therefore very important to understand the effects of laser processing technologies on corrosion and biocompatibility of these NiTi alloys. Albeit, cases of Ni ion release from medical devices have been reported during clinical implementation [123, 124], highlighting the importance of, and need for, proper characterization; especially for material processed using novel protocols.

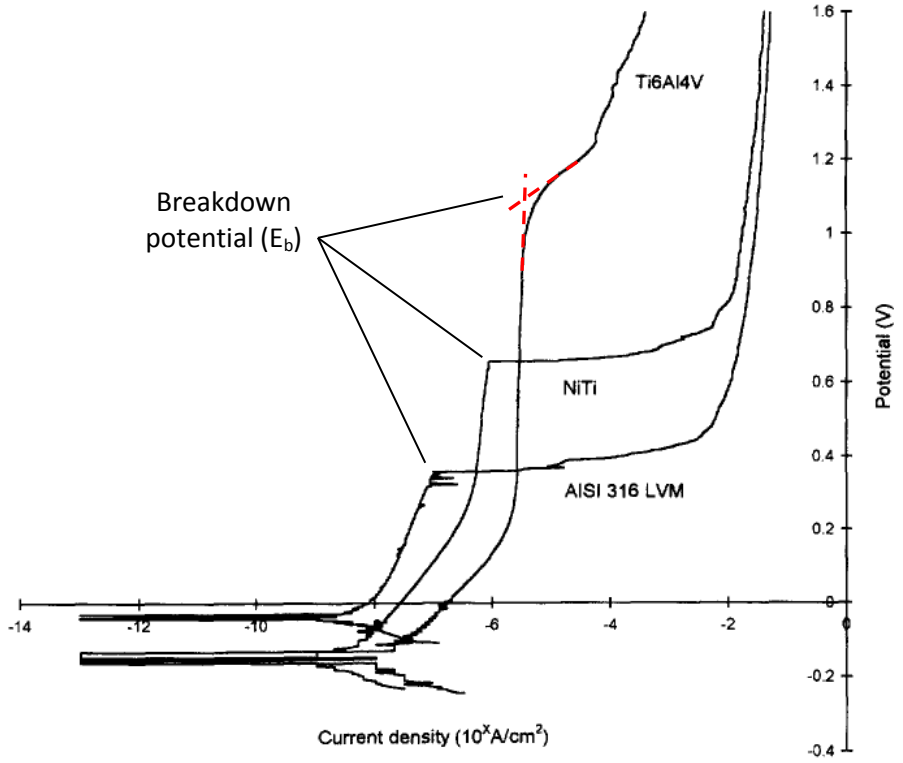

Figure 26: Cyclic potentiodynamic corrosion test results for Ti6Al4V, equiatomic NiTi, and 316 SS alloys. Test performed in Hanks' solution at 37 °C. Adapted figure from [118]

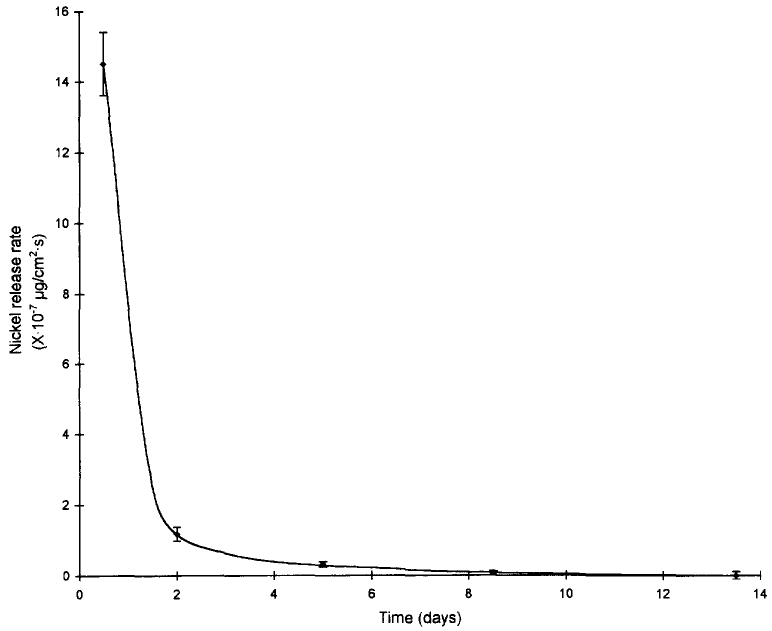

Figure 27: Ni ion release from an equiatomic NiTi alloy immersed in Hanks' solution at 37 °C; measured using Atomic Absorption Spectroscopy. Figure taken from [118].

2.7.1. Corrosion performance and biocompatibility of laser processed NiTi

Currently, only limited studies detail the corrosion performance and biocompatibility of laser processed NiTi [75-81, 125, 126], while even fewer attempt to thoroughly characterize its surface [75, 81]. Improvements in corrosion performance immediately following laser processing have been reported in most studies, including those by Yan et al. [76, 77, 79], Man et al. [80], Cui et al. [81], and Villermaux et al. [126]; as shown in Figure 28 [79]. Furthermore, Ni and Ti ion release from laser processed NiTi specimen was also shown to remain lower than that found in drinking water as observed by Sevilla et al. [125]. These promising results have been attributed to a combination of mechanisms, including enhanced surface condition (i.e. reduced roughness, increased oxide stability, etc.), removal of contaminants (i.e. carbon and oxide inclusions, additional phases, etc.), and changes in Ni:Ti ratio on the surface [75, 76, 79-81]. An example of removing contaminants is provided in Figure 29 following a laser surface melting (LSM) process [80]. Insignificant proof stemming from a lack of surface analysis however, limits any validation of the above proposed mechanism for improved corrosion and Ni ion release performance. This is further complicated by inconsistencies in literature. For example, a study by Chan et al. [75] on laser welded NiTi showed a reduction in corrosion performance immediately after welding; contradicting all the aforementioned studies showing improvements in the as-processed state. Hence, a better understanding and sufficient level of confidence on the mechanisms behind the corrosion properties of laser processed NiTi SMAs is required.

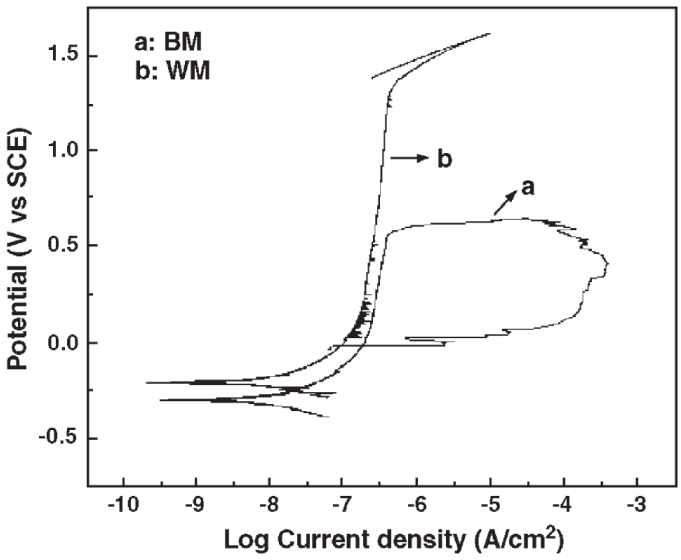

Figure 28: Cyclic potentiodynamic corrosion results for the base material (BM) and welded metal (WM), highlighting improved resistance to corrosion post-welding. Figure taken from [79].

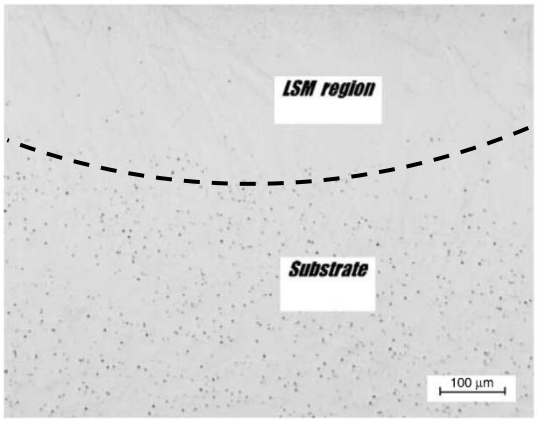

Figure 29: Comparison of inclusion content in laser surface melted (LSM) versus the NiTi substrate. The dark phase consists of Ti_2Ni and TiC inclusions in the bulk material. Adapted figure from [80].

2.8. Summary and concluding remarks

Extensive review of the literature highlights the complexity of the NiTi system, its phase transformation characteristics, and most notably in manufacture/processing of NiTi components. The extreme sensitivity of the unique SME, PE and biocompatibility properties of NiTi was identified to result from factors such as composition, dislocation density, texture, secondary phases, mechanical properties, and surface condition. Traditionally the functional properties are fine-tuned through combined hot work, cold work, and annealing and/or aging heat treatment by material manufacturers to produce net-shape products (i.e. sheet, bar, tube, wires, strip, etc.). These manufacturing processes are however performance limiting since each component possesses only one set of thermomechanical properties throughout. Novel techniques such as local heat treatments, powder metallurgy, welding and joining, and more recently laser processes have been investigated to locally modify functional properties improving material functionality. However, only limited success was achieved with these novel protocols in their current state of the art.

Laser processes such as laser annealing, laser alloying, and laser induced vaporization have more recently shown great promise in achieving local augmentation of functional properties. Local augmentation of functional properties combined with the high speeds, low heat input, high cooling rate, and high quality inherent of laser processes make them a strong candidate for achieving increase functionality of NiTi SMAs. Laser processing of NiTi SMAs is however for the most part unprecedented and much research is required before they can be applied successfully in industry. The main shortcomings in the current science of laser processing NiTi SMAs identified herein include:

1. The mechanical properties of laser processed materials degrade following laser processes such as laser welding. The thermal cycles of the process induce melting and/or heat treatment to the NiTi base material removing or altering any past effects from thermomechanical processing. The structural properties must therefore be restored to achieve full functionality of the NiTi SMA in particular regarding PE and cyclic performance. Only limited studies however investigate post-laser processing techniques. More work in this area is therefore essential in achieving application specific performance requirements.
2. There is much confusion regarding the effects of laser processing on phase transformation characteristics. Different laser processing studies show conflicting changes in phase transformation temperatures with no explanation or analysis regarding these contradictions (section 2.5.1.).

3. Although proof of concept has been demonstrated for laser processes (section 2.5.) including the laser induced vaporization protocol (section 2.6.) the process-structure-performance relationship of such processes is missing. This makes applying laser technologies to meet demands of a specific application impossible. More specifically, definitive measurement of composition changes and characterization of microstructure and performance following laser processing have not yet occurred. Therefore, even the vaporization mechanism of section 2.6. and its relation to SME and PE performance cannot be made with the current understanding.
4. Only limited studies detail the corrosion performance and biocompatibility of laser processed NiTi where in general, improvements in corrosion and Ni ion release performance have been reported (section 2.7.1.). However, proposed mechanisms behind this performance including, enhanced surface condition, removal of contaminants and additional phases, and changes in Ni:Ti ratio have not been adequately investigated. A lack of surface characterization and inconsistencies in literature limits any validation of the above proposed mechanisms. A better understanding and sufficient level of confidence on the mechanisms behind the corrosion properties and biocompatibility of laser processed NiTi SMAs is therefore still required before they can be applied in medical applications.

The above findings regarding the laser processing of NiTi SMAs directly reflect the objectives of this research study, presented in section 1.2., and will therefore be addressed in the coming chapters.

3 Experimental Methods and Conditions

In this section the processing protocol and analysis of NiTi material is provided within the scope of applying these augmented SMA materials to medical device applications. Under this scope certain constraints were implied such as the specific materials chosen as well as the requirement of smooth, defect free surface finish following processing. In the medical industry standard PE material has a Ni composition of ~50.8 at. % and the thicknesses of these materials used in medical devices is usually < 700 µm. Also, Nd:YAG processing was carried out on both wire and sheet material with full and partial penetration successfully covering a range of processing scenarios believed to be most useful for medical device applications. It is expected that the processing protocol and theoretical concepts developed in this work are scalable to materials with different composition, geometries, and larger thicknesses. However, work was not carried out to investigate scalability and the manner at which these processes and theories scale may not be trivial.

3.1. Multiple memory actuation experiments

3.1.1. Material

Commercially available 410 µm (0.016 in.) diameter wire, manufactured by Memry Corporation was used in this study. The nominal composition for NiTi SMA wire was 55.9 wt.% (50.8 at.%) Ni and 44.1 wt.% (49.2 at.%) Ti. The wire material was thermomechanically processed by the material supplier to exhibit SME and PE properties. Prior to laser processing, the wire was chemically etched in a 7.5 vol.% HF, 20 vol.% HNO_3, balance H_2O solution to remove a thick black oxide layer; uniformly reducing the wire diameter to 400 µm.

3.1.2. Laser processing equipment and parameters for wire material

A LW50 A Miyachi Unitek pulsed Nd:YAG laser system with a 1.06 µm wavelength, 600 µm nominal spot diameter and top-hat spatial profile (Figure 30) was used in this work. This particular system was equipped with a power monitor allowing for accurate in-situ assessment of incident power output.

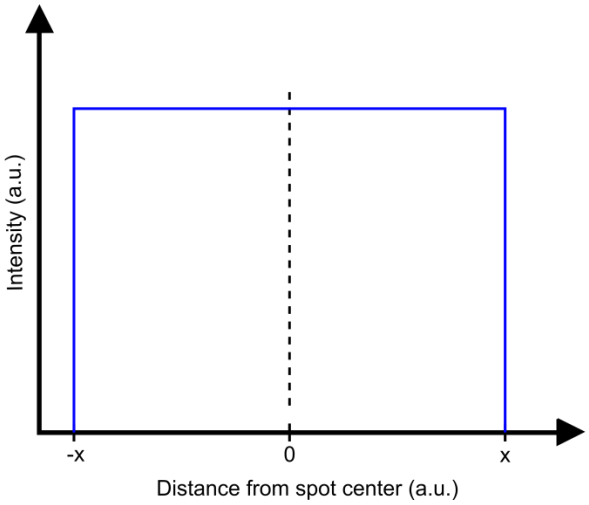

Figure 30: Top hat spatial profile of laser intensity (focused spot radius = x)

Laser processing of wire was performed with a spot size of 600 µm in order to ensure the full 400 µm diameter wire was irradiated with the incident beam. An automated fixture (i.e. BWH fixture) was used to index the wire during processing as shown in Figure 31. Argon shielding gas with a flow rate of 0.42 m^3/hr (15 CFH) was found to be sufficient to avoid oxidation during processing. Laser processing parameters (i.e. peak power, pulse shape, frequency etc.) were altered to control the transformation temperatures during processing. A 5 ms temporal pulse profile having a 1 ms up and down-slope was used with a 1.0 kW peak power as shown in Figure 32. These parameters were found to be sufficient to induce the required Ni vaporization while achieving full penetration. Overlapping the processed region by 75 % was identified as being the ideal condition for optimum surface finish while eliminating a brittle terminal solidification region.

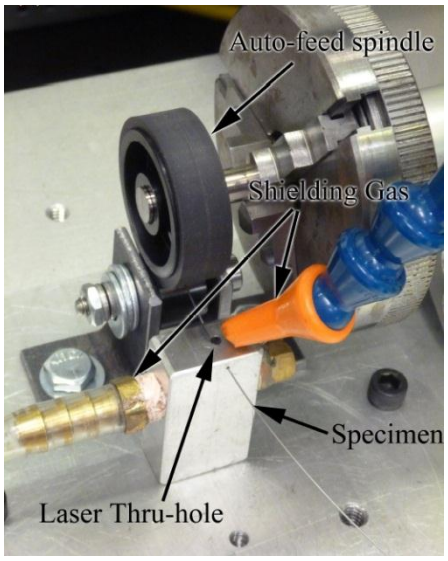

Figure 31: Laser fixture for processing NiTi wire. Laser irradiation was directed into the Ar filled cavity where the processing occurs. A drive roller type auto-feed system indexes the wire during processing.

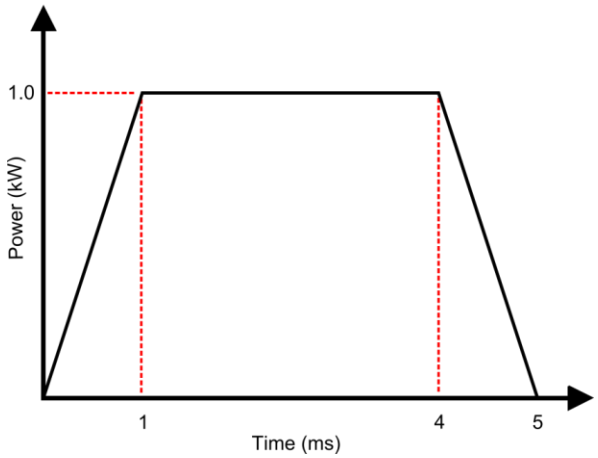

Figure 32: Laser processing schedule for processing 400 µm NiTi wire

3.1.3. Thermal analysis

A Thermal Analysis Q2000 DSC equipped with a refrigerated cooling system was used to identify the phase transformation temperatures of the as-received and laser processed materials. A modified version of the ASTM F2004-05 standard test method for transformation temperature of NiTi alloys by thermal analysis was adhered to. Testing temperatures ranged between -198 K (-75 ^{o}C) to 393 K (120 ^{o}C), controlled at a rate of 5 K/min. The start and finish transformation temperatures; austenite start (A_s), austenite finish (A_f), martensite start (M_s), and martensite finish (M_f) were determined as per the ASTM

standard using the TA Instruments Universal Analysis 2000 v4.5A software. Wire pieces having 3 mm length were cut and placed into the DSC pan for analysis.

3.1.4. Tensile testing

Deformation of the as-received and laser processed materials was assessed using a temperature chamber equipped Instron model 5548 micro-tensile tester having load and strain measurement accuracy of ± 0.4 % and ± 0.5 µm respectively. Test samples having a 30 mm length were loaded at temperatures below M_f of the as-received and laser processed materials (i.e. -50 and 30 °C) under an ASTM F2516-07 testing protocol at a rate of 0.8 mm/min. The tests performed at -50 °C were designed to mimic the conditions during initial straining of the actuator prior to actuation while the tests performed at 30 °C were representative of the condition of the laser processed region of the actuator following actuation of the as-received region.

3.1.5. Dynamic actuation and low cycle performance characterization

In order to characterize the SME of laser processed material a custom test set-up was constructed to characterize the performance of NiTi wire (i.e. linear actuator). A spring biased configuration was chosen, as illustrated in Figure 33, similar to that used in references [127-129]. To ensure that the wire was completely in the martensite phase prior to heating, dry ice was used; maintaining an ambient temperature below -50 °C. A pre-stress of 234 MPa (i.e. 3 kg-f load) was applied via the bias spring to achieve the required initial strain in the martensite phase to enable the SME. Actuation was achieved by resistive heating causing the wire NiTi material to change phases from martensite to austenite and subsequently actuate by recovering the initial strain induced by the bias spring. A constant voltage Sorensen XG 33-25 programmable direct current (DC) power supply was used to supply the required power. The displacement, load, and electrical resistance were measured during testing using a National Instruments PXI-1031 data acquisition (DAQ) module. The change in actuator length (i.e. displacement) was measured using a ± 0.2 µm sensitivity Heidenhain displacement sensor and the load was measured using a 500 N load cell.

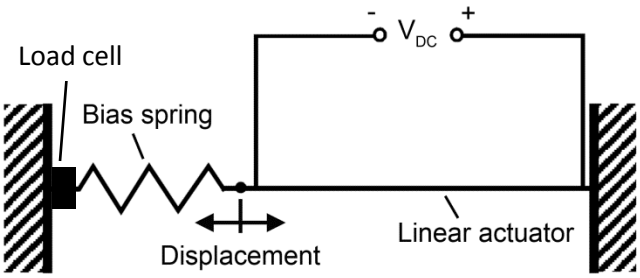

Figure 33: Illustration of the spring biased linear actuator test set-up (not to scale)

Low cycle actuation testing of the NiTi wire actuator was performed in the temperature chamber of the Instron micro-tensile tester at a constant temperature of -50 °C. The wire was actuated through 200 cycles consisting of a 10 second resistive heating segment where the temperature of the wire reached above the A_f followed by a 10 second cooling segment where the wire was allowed to cool below the M_f of both materials. A constant load of 234 MPa (i.e. 3 Kg-f load) was held by the cross-head while displacement was measured versus time. A 50 mm length of wire was used in cyclic testing due to a size limitation of the temperature chamber. The recoverable (ε_r) and residual (ε_p) strains were extracted after each activation cycle.

3.2. Combined laser processing, cold working and heat treating experiments

3.2.1. Material

A 0.37 mm thick by 12 mm wide SE508 NiTi strip manufactured by Nitinol Devices and Components (NDC) Inc. was used in this study. The nominal composition of this binary NiTi alloy was 55.8 wt.% (50.7 at.%) Ni and 44.2 wt.% (49.3 at.%) Ti with maximum oxygen and carbon contents of 0.05 and 0.02 wt.%, respectively. The as-received cold-rolled material was solutionized at 1073 K (800 °C) for 3.6 ks followed by water quench to remove any effects of past treatments during manufacturer. Prior to laser processing the NiTi strip was ultrasonicated for 2 minutes, flipping half way, in a 7.5 vol.% HF, 20 vol.% HNO_3, bal. H_2O solution to remove a thick black oxide layer. This chemical etching process uniformly reduced the thickness of the strips by 20 µm.

3.2.2. Laser processing equipment and parameters for strip material

The same Nd:YAG laser system outlined in section 3.1.2. was used for processing the NiTi strip. During laser processing, the top and bottom of the strips were shielded with argon gas to avoid excessive oxidation as shown in Figure 34. A flow rate of 14.2 L/min (30 CFH) was found to be sufficient as identified by a shiny metallic appearance. A pulsed laser protocol was utilized having a peak power of

0.8 kW and the pulse schedule shown in Figure 35a). This particular schedule allowed for full penetration through the NiTi strip while reducing the severity of the keyhole dimple at the center of each laser spot; a common artifact of pulsed laser processes. Rows of laser spots overlapped by approximately 50 % in the x- and y-directions were staggered adjacent to one another ensuring that the whole sample area was processed, as shown in Figure 35b).

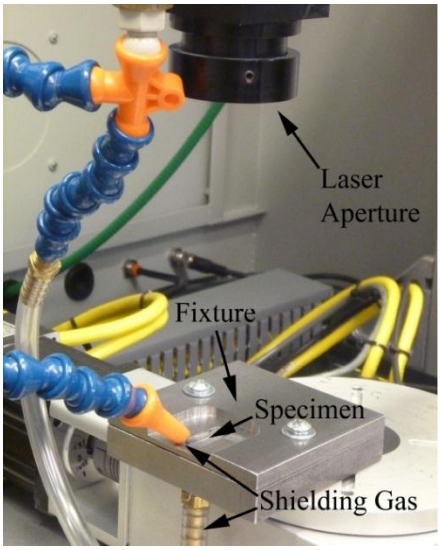

Figure 34: Laser set-up for processing NiTi strip. Strip material was clamped in fixture with Ar shielding on both the top and bottom to prevent oxidation.

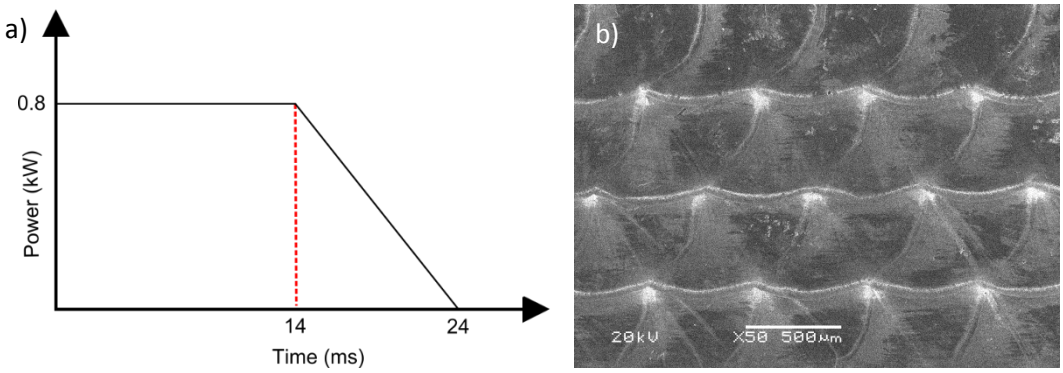

Figure 35: a) Laser pulse schedule for processing the NiTi strip and b) scanning electron microscopy (SEM) image of laser processed surface with 50 % overlap of pulsed laser spots in the x- and y-directions b)

3.2.3. Post-processing of laser processed NiTi material

Post-process cold rolling at 403 K (130 °C), reducing the sample thickness by 27 % (i.e. 350 ⟶ 255 µm), followed by annealing at 673 K (400 C) for 3.6 ks was performed on select specimen to improve both structural and therefore functional properties of the laser processed material. A cross-sectioned image of the base material and cold worked material is provided in Figure 36. As discussed in section 2.2.2.

cold work above 25 % and 1 hr heat treatments have been found to be ideal for improved structural and functional properties [4, 40, 41].

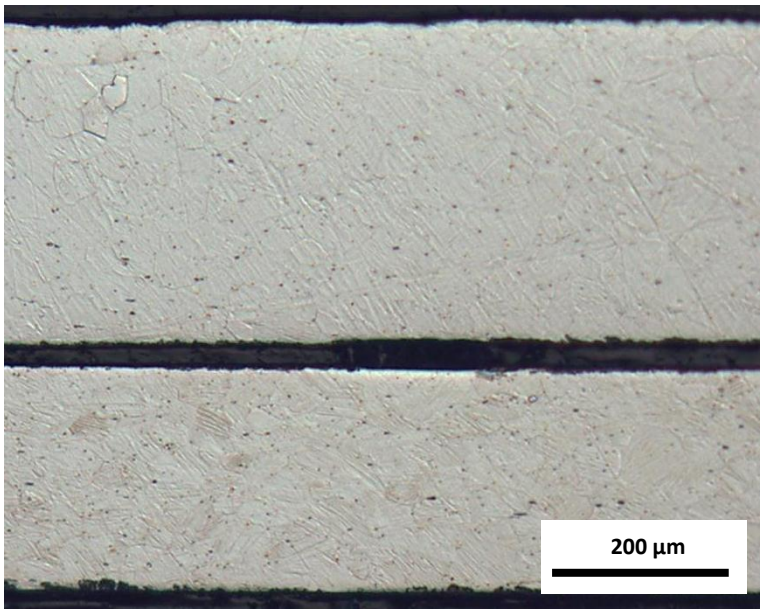

Figure 36: Cross-section of base material in a) as-received condition and b) cold rolled condition (27% reduction)

3.2.4. Chemical composition measurement

The chemical composition of a 100 x 100 µm area of each specimen were measured using micro-particle induced x-ray emission (micro-PIXE) spectroscopy by rastering a 3 MeV proton beam across cross-sectioned samples. The X-ray spectra were processed using the Guelph PIXE software package. A least-squares-fit to the spectrum was conducted to deduced X-ray intensities and convert to concentrations using National Institute of Standards and Technology (NIST) materials standards. Using this technique the Ni and Ti concentrations were captured with < ± 0.21 at.% measurement accuracy. The high sensitivity of micro-PIXE analysis over other techniques such as energy-dispersive x-ray spectroscopy (EDS) analysis owns to lower crystal charging from Bremsstrahlung radiation, significantly reducing background noise in the obtained x-ray spectra. The highest possible measurement accuracy was necessary, since changes in the order of a tenth of an atomic percent can lead to > 10 K variation in transformation temperatures of NiTi SMAs [12].

3.2.5. Microstructure characterization

The microstructure was characterized using optical microscopy (OM) and transmission electron microscopy (TEM). TEM techniques used includes: scanning transmission electron microscopy (STEM);

in-situ heating of the TEM specimen; EDS analysis; and selected area diffraction (SAD). A Jeol 2010F TEM/STEM field emission microscope operating at 200 kV and a Philips CM12 analytical TEM with a cooling/heating stage operating at 120 kV were used. Multiple TEM specimens were analyzed from each sample condition. One prepared using focused ion beam (FIB) and two prepared via jet-polishing. A Zeiss NVision 40 FIB was used to prepare the FIB specimen from cross-sectioned optical microscopy samples. The jet-polished specimen were prepared using a Struers, Tenupol 5 operating at 243 K (-30 °C) and 15 V, in a 25 % HNO_3 + 75 % CH_3OH solution.

3.2.6. Thermoanalytical analysis

For thermoanalytical analysis similar equipment and procedures as outlined in section 3.1.3. were used. Samples were mechanically punched to 3 mm diameter and placed in the DSC pan. Each sample condition was tested at least three times.

3.2.7. Monotonic and cyclic tensile testing experiments

The structural and functional properties were identified through tensile testing performed using similar equipment as outlined in section 3.1.4. Strips samples with a 1.5 mm width and 30 mm length were cut using wire electrical discharge machining (EDM) to minimize detrimental strain and thermal effects. Tensile tests were performed with a 20 mm gauge length and a strain rate of 0.8 mm/min at temperatures ranging from 293 – 363 K. Each sample condition was tested at least three times during the DSC and tensile testing experiments.

3.3. Surface characterization and corrosion performance experiments

3.3.1. Material

A 0.37 mm thick by 12 mm wide SE508 NiTi strip manufactured by Nitinol Devices and Components (NDC) Inc. was used in this study. The nominal composition of this binary NiTi alloy was 55.8 wt. % (50.7 at. %) Ni and 44.2 wt. % (49.3 at. %) Ti with maximum oxygen and carbon contents of 0.05 and 0.02 wt. %, respectively. The as-received material was in the cold-rolled state from the manufacturer. Prior to any testing, the NiTi strip was ultrasonicated for 2 minutes, flipping half way, in a 7.5 vol. % HF, 20 vol. % HNO_3, bal. H_2O solution to remove a thick black oxide layer. This chemical etching process uniformly reduced the thickness of the strips to 0.35 mm. The chemically etched state is referred to as CE for this study.

3.3.2. Laser processing equipment and parameters for strip material

The same Nd:YAG laser system outlined in sections 3.1.2. and 3.2.2. was used for processing the NiTi strip in these experiments. A pulsed laser protocol was utilized having a peak power of 0.8 kW and the pulse schedule shown in Figure 37a. The laser spots were overlapped by 56 % to ensure that the whole sample area was processed as illustrated in Figure 37b. Each spot was pulsed five times to achieve the desired thermomechanical properties through change in microstructure and bulk material composition. This material state will be referred to as laser processed (LP).

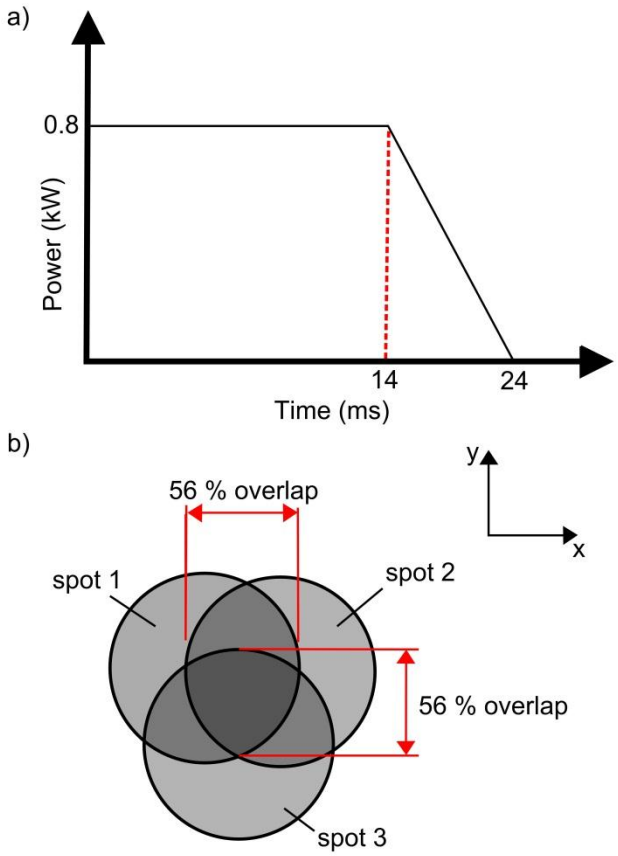

Figure 37: a) laser pulse schedule for partial penetration of NiTi strip, b) illustration of 56 % overlap of laser spot configuration allowing for the complete coverage of the desired sample area

3.3.3. Mechanically polished surface

Mechanical polishing was used to remove any effects of the differing surface topography and chemistry created from laser processing, to better characterize the bulk material. Strips were cut in 8 x 8 mm squares and progressively ground with 600, 800, 1200 coarse, and 1200 fine grit silicon carbide paper. Polishing was then performed with a 0.03 µm colloidal silica suspension and 30% hydrogen peroxide

mixture (9:1 ratio). This state will be referred to as laser processed and polished (LP-Pol). Extreme care was taken to use consistent grinding/polishing protocol for each individual specimen.

3.3.4. Material characterization

To characterize the thermoanalytical properties of the NiTi materials DSC analysis was performed as outlined previously in sections 3.1.3. and 3.2.6.

To observe the microstructure of the bulk material and the surface condition, OM was performed using an Olympus BX51M upright inspection and research microscope. The surface condition was characterized further using optical profilometry performed on a WYKO NT1100 optical profiler manufactured by Veeco having ±1 nm resolution. Three dimensional topographical surface maps of the CE, LP and LP+Pol samples and Ra roughness values were obtained from a 1.2 x 0.92 mm area. Analysis of surface characteristics after corrosion testing was performed with the use of a JEOL JSM-6460 scanning electron microscope (SEM) with a 20 kV electron beam.

For OM, sample cross-sections were progressively ground with 600, 800, 1200 coarse, and 1200 fine grit silicon carbide paper. Polishing was then performed with a 0.03 µm colloidal silica suspension and 30% hydrogen peroxide mixture (9:1 ratio). Subsequently a 15 s chemical etch in a 3 vol. % HF, 14 vol. % HNO_3, and bal. H_2O solution was applied.

3.3.5. Surface characterization

To characterize surface chemistry XPS analysis was conducted using a K-Alpha XPS manufactured by Thermo Scientific Inc. using monochromatized Al Kα1 radiation. The source was run at 15 kV and 72 W. The emitted photoelectrons were sampled from a 400 x 400 µm area. Sputtering was done with a 2 kV Ar+ ion beam rastered over a 2 x 2 mm area. Survey scans were taken at pass energy of 50 eV and a binding energy range of 0 – 1300 eV.

Surface composition depth profiling was achieved using AES. Auger analysis was performed using a PHI 660 scanning Auger microprobe. A 5 kV (~300 nA) electron beam rastered over a 100 x 100 µm area (1,000X) was employed for this investigation. Sputtering was performed using a 3 kV Ar+ ion beam rastered over 2 x 2 mm area. The sputter rate under these conditions was determined to be ~ 30 nm/min for a SiO_2 on Si layer (280 nA ion current). Sputtering rate for SiO_2 on Si substrate has been determined to be similar to TiO_2 [130]. The oxide thickness was estimated to be where the oxygen percentage dropped to half its maximum value.

Raman was performed to aid in identification of the surface species present as well as identify the degree of crystallinity of the oxide. Spectra were recorded using a Renishaw Ramanscope with a spatial resolution of < 1 cm^{-1}. This spectroscope was equipped with a He-Ne laser having a 633 nm wavelength and a 5 µm spot size.

3.3.6. Corrosion testing and Ni ion release measurement

Potentiodynamic corrosion tests were performed in a phosphate buffered saline (PBS) electrolyte (pH7.4) manufactured by MP Biomedicals using a 300 ml double walled corrosion cell as shown in Figure 38. A GAMRY Instruments potentiostat with Framework v4.35 software was used for controlling the tests. A three electrode configuration was used according to the ASTM F2129-08 standard for cyclic polarization testing. The reference electrode was a saturated calomel electrode (SCE) and the counter electrode was Pt mesh. The working electrode consisted of a custom sample holder, which exposed 0.25 cm^2 of the specimen surface area using an area limiting gasket. All tests were performed at 37 °C to simulate biological conditions. Before testing began, the solution was de-aerated with nitrogen for 30 minutes. The open circuit potential was measured up to one hour, or until it was stable within 0.05 mV/s. Testing was performed at a scan rate of 0.167 mV/s, starting at -0.5 V and increasing to 1.5 V. Scanning was automatically reversed if the current density reached 0.1 mA/cm^2. A minimum of three specimens was tested for each material condition and representative curves were provided herein.

Ni ion release measurements were made using a Prodigy ICP-OES manufactured by Teledyne Leeman Labs Company. A Ni ion lower limit of detection (LLOD) of 13.2 µg/L (13.2ppb) was determined during calibration. A surface area of 1.63 cm^2 was immersed in 15 ml of PBS solution for 7 days ± 1 hour at a temperature of 37 °C. Seven days is the amount of time specified by ISO 10271 Dental Metallic Materials – Corrosion Tests and previously used by D. Vojtech et al. [131]. Moreover, it was previously found by A. Michiardi et al. [132] that Ni ion release stabilized and dropped to almost zero after 5 days. The Ni concentration in the control sample, determined to be 16.3 (± 10.2) µg/L, was subtracted from the total Ni concentrations found for each sample. The results provided in this work were normalized by the particular surface area for each sample and were the mean values of three measurements.

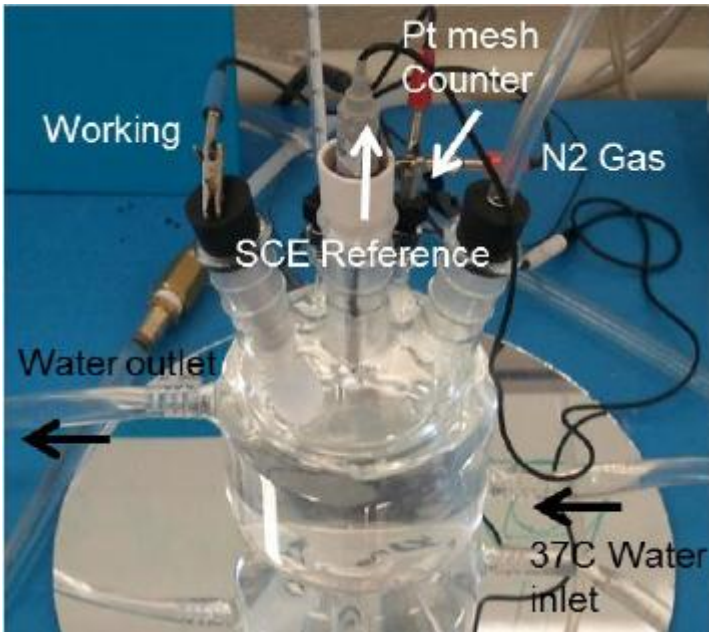

Figure 38: Cyclic potentiodynamic corrosion cell operating at 37 °C

4 Dynamic Actuation and Control of a Novel Laser-processed NiTi Linear Actuator

To assess the SME properties of laser processed NiTi material a spring biased multiple memory linear actuator was developed. The processing parameters were selected in order to establish two distinct actuations of the wire actuator; one resulting from the SME of the as-received region and the second from a laser processed region. A peak laser power of 1.0 kW with a 5 ms temporal pulse profile, outlined in section 3.2.2., was used in this work. Half of the 100 mm length of the wire actuator was processed as illustrated in Figure 39 a). An optical micrograph of the interface between the as-received and processed regions is provided in Figure 39 b). The work presented and described in this chapter has been previously published by Pequegnat et al. [133].

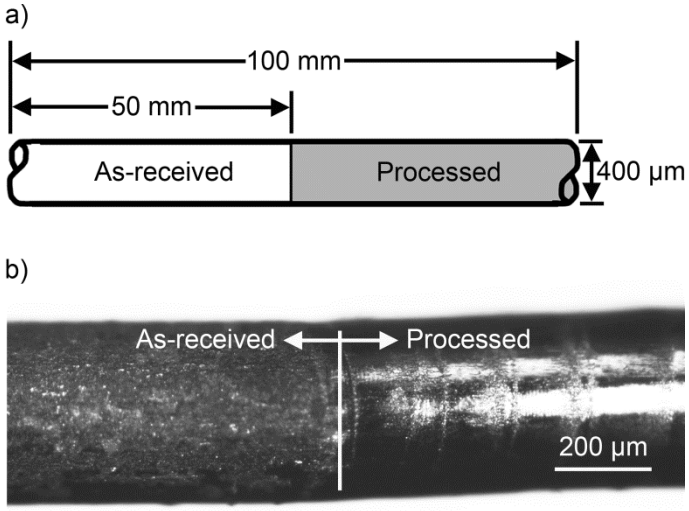

Figure 39: a) Schematic illustration of linear actuator (not to scale) and b) optical micrograph of interface between as-received region and laser processed region [133]

4.1. Transformation temperatures of processed wire

Differential scanning calorimetry results for both as-received and laser processed materials are shown in Figure 40. The A_s, A_f, M_s, and M_f phase transformation temperatures extrapolated from the DSC curves are summarized in Table 4. Transformation temperatures of the processed material increased significantly compared to the as-received material as expected following the laser induced vaporization protocol described in section 2.5. In this study the A_f and M_f temperatures were increased by 71.7 °C and 46.6 °C respectively. Hence, it was to be expected that during resistive heating less heat input (i.e. lower voltages) would be required to actuate the as-received region of the actuator compared to the laser processed region. For example once the A_f temperature of the as-received region (19.5 °C) has

been reached, 50 % of the wire will be in the austenite phase. Following further heating past the A_f temperature of the laser processed region (91.2 °C), the whole wire actuator will be in the austenite phase.

Table 4: Phase transformation temperatures (°C) from thermo-analytical DSC analysis [133]

	A_s	A_f	M_s	M_f
As-received Material	-22.3	19.5	9.8	-14.6
Processed Material	73.5	91.2	62.0	32.0

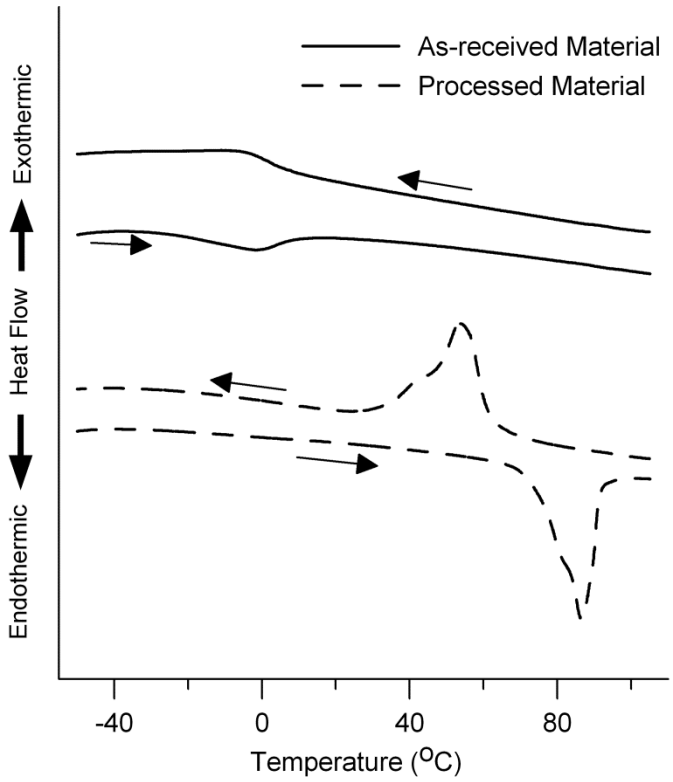

Figure 40: DSC data for as-received and laser processed materials [133]

4.2. Actuation and shape memory effect

Actuation was induced using a voltage profile which first increased from 0.5 V to 1.8 V then decreased back to 0.5 V while monitoring wire displacement. Voltage stepping of 0.05 V every 2 seconds was used to ensure steady heating and cooling, as shown in Figure 41 a). With increasing voltage, wire temperature surpassed A_f for the as-received and laser processed regions of the processed actuator, subsequent decrease in voltage induced cooling below M_f of both regions. Figure 41 b) shows the two distinct actuations in the displacement measurement for the laser processed actuator. Upon application of voltage, first the as-received region transformed from martensite to austenite causing the processed

actuator to initially recover 2.48 mm of strain. Increasing the voltage further triggered the second actuation and recovery of an additional 1.0 mm of strain from the laser processed region. As the voltage decreased the reverse effect was observed, first the processed region transformed from austenite to martensite followed by the same transformation in the as-received region. The bias spring facilitates straining the actuator first by 1.0 mm then by 2.48 mm as phase transformation to martensite takes place in the laser processed and the as-received regions, respectively. Also shown in Figure 41 b) is the displacement trend from a 100 mm as-received actuator that was subject to the same voltage profile. Only one actuation was observed however, 5.32 mm maximum displacement was achieved; a 34.6 % larger active strain than the laser processed actuator.

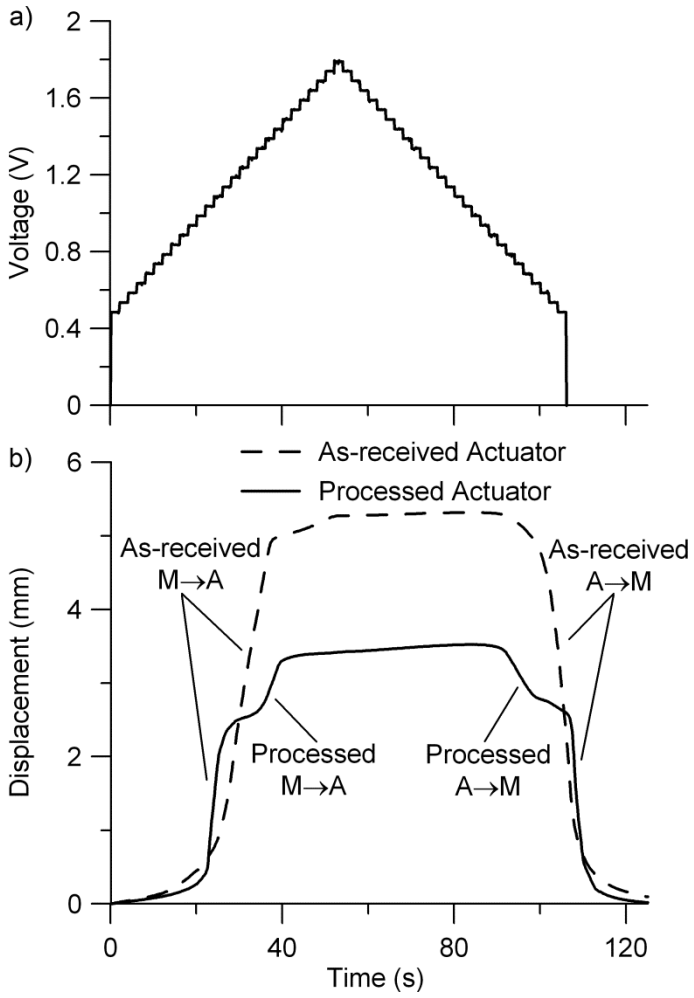

Figure 41: a) Voltage profile and b) displacement measurements [133]

Through laser processing, different regions of the actuator were 'programmed' to fully actuate giving the desired load and displacement at specific temperatures. The length (i.e. volume) of each of the

processed regions as well as the transformation temperature can be easily adjusted to obtain the desired response. Therefore, the need for partial transformation using minor hysteresis loops was not necessary for dynamic actuation. For example, a simple DC voltage profile such as that shown in Figure 42 a) was used with the two memory actuator developed in this study. In the first voltage pulse the voltage was increased to 1.4 V allowing for quick heating of the linear actuator and subsequently actuation of the as-received region. The voltage was then backed off slightly to 1.1 V maintaining a temperature just above the A_f of the as-received region. Following the first actuation a displacement of 2.48 mm was achieved yielding a 274 MPa stress. Next the voltage was increased to 1.8 V increasing the temperature above the A_f of the laser processed region, where the second actuation occurred. A total displacement of 3.48 mm was achieved yielding a fully actuated stress of 287 MPa. Two distinct changes in resistance were also clearly observed in the resistance measurement shown in Figure 42 c) where the resistance of the laser processed region behaves as expected during SME actuation. This change in resistance has proven to be useful when developing control systems for SMA actuators [128, 134].

As demonstrated, using a laser processed actuator greater control over the amount of actuation and the temperatures at which these actuations occur can now be achieved using simple control methods. Extraordinarily, laser processed actuators can now be actuated in a passive manner where the temperature of the ambient environment gives the desired dynamic response; enabling countless new applications for SMAs.

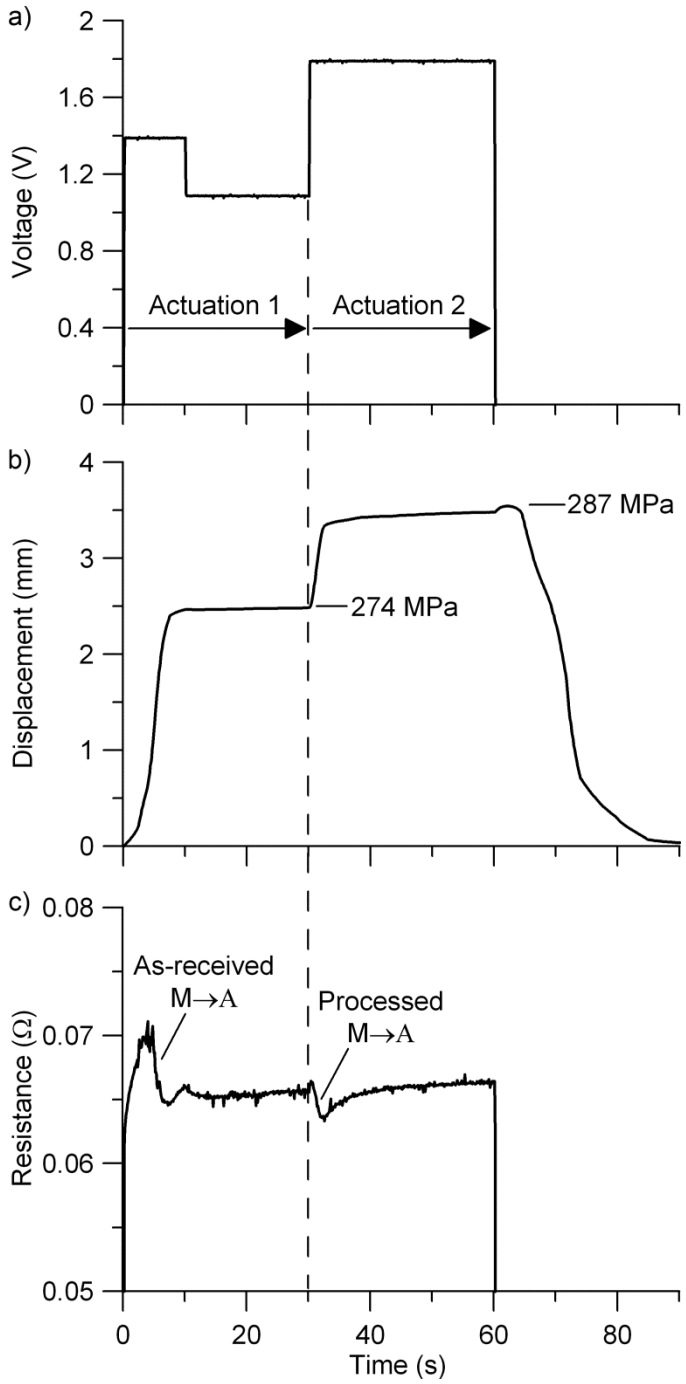

Figure 42: Dynamic actuation of a two memory laser processed linear actuator by resistive heating. a) DC voltage profile, b) actuation displacement, and c) resistance measurement [133]

4.3. Stress-strain behaviour and the detwinning of martensite

To better understand the effects of laser processing on the SME, monotonic tensile tests were performed. The results from tests performed at -50 °C, simulating the initial pre-straining of the processed actuator, are presented in Figure 43 a). The deformation behaviours of the martensite phase of as-received material and laser processed material are shown for up to 10 % strain. There are two notable differences in the stress-strain behaviour of the laser processed material compared to the as-received material. These differences include the absence of the serrated, flat 'Lüders-like deformation' and a substantially larger martensite reorientation or flow stress (i.e. σ_m of Figure 11) in the laser processed material.

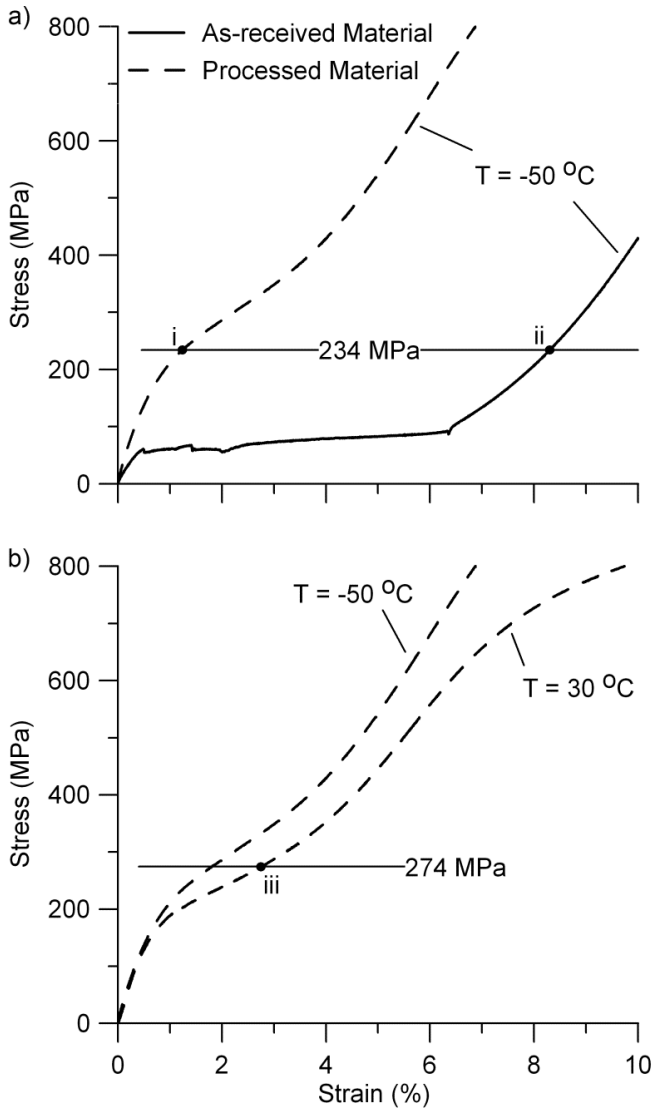

Figure 43: Detwinning of martensite in as-received and laser processed regions at -50 °C a), comparison of detwinning stresses and strains at -50 °C and 30 °C for laser processed material b) [133]

The presence of Lüders-like deformation in NiTi alloys is the result of sudden reorientation of martensite during deformation resulting in the propagation of a macroscopic strain band [135] similar to that discussed in section 2.2.2. during the austenite to SIM transformation. This reorientation of martensite consists of neighbouring martensite variants becoming twin related, propagation/migration of the interface between neighbouring variants, and further detwinning of the reoriented martensite variants as discussed in section 2.2.1. [4, 38]. Once the stress exceeds the barrier stress for martensite reorientation the stress drops slightly and remains almost constant creating the stress-plateau as observed in the stress-strain curve for the as-received material in Figure 43 a) [38, 136]. The ability of a strain band to propagate and lead to a stress-plateau is heavily dependent on the texture of the NiTi alloy [38, 135, 137]. After initiation of the strain band no additional stress is necessary for propagation if a majority of the twinned martensite variants have a habit plane in the same direction as the local strain band [135]. The local stress concentration adjacent to the strain band is therefore sufficient to cause propagation. Liu et al. [137] found when deforming martensite in the rolling direction that a stress-plateau was possible. Murasawa et al. [135] showed similar results with rolled NiTi sheet that had been heat treated below 400 °C, where it was identified that the strain band and habit plane both exist at -55° and +55° to the loading direction. Therefore, it was deduced that during loading parallel to the drawing direction of the as-received wire the texture of the material was such that the formation and propagation of a strain band was possible leading to the stress-plateau observed during the deformation of the martensite structure (Figure 43 a)). In fact, Frick et al. [57] showed that the texture of cold drawn is ideal for tensile loading, leading to the formation of a flat long stress-plateau during the detwinning of martensite.

The absence of the Lüders-like deformation in the laser processed material was also attributed to texture effects. Since the laser processed material had solidification type microstructure the texture was expected to be significantly different from the as-received drawn wire. The sloped strain-hardening behaviour observed in Figure 43 a) for the laser processed material was a result of the inability to form and propagate a macroscopic strain band. When the priority habit planes exist in several different angles relative to the loading direction, a single flow stress for martensite reorientation does not exist, and therefore the sudden appearance of a stress-plateau is not observed [135]. Increasing stresses are necessary to reorient martensite variants having different angles from the loading direction leading to the strain-hardening effect as observed for the laser processed material in Figure 43 a). Murasawa et al. [135] and Liu et al. [137] obtained similar strain-hardening trends during the tensile testing of NiTi sheet

having a recrystallized texture and when loading in the transverse direction to the rolling direction, respectively.

The greater σ_m of the laser processed material shown in Figure 43 a) was a result of the martensite in the laser processed material being more stable at -50 °C than that in the as-received material. Since the reorientation of martensite is dependent on the movement of mobile defects, such as interfaces between neighbouring variants and twins which occur by thermal activation mechanisms, higher stress is required to cause reorientation. Miyazaki et al. [30] showed that the flow stress increases with decreasing temperature below M_f. Since the difference between the test temperature of -50 °C and M_f of the laser processed material was 46.6 °C (or 57 %) greater than that of the as-received material, a larger σ_m was expected.

4.4. Effect of martensite properties on actuator performance and SME

The strain-hardening behaviour of the laser processed material and higher σ_m had a large effect on the active strain in the as-received and processed regions of the actuator. As denoted by (i) and (ii) in Figure 43 a), the amount of initial strain in the processed and as-received regions following the 234 MPa pre-stress were 1.2 % and 8.3 % respectively. The amount of strain experienced during the deformation of martensite is directly related to the magnitude of active strain possible via the SME [34]. Therefore, a greater displacement was expected during actuation of the as-received region of the actuator as observed in Figure 41 b) and Figure 42 b). From the activation of the as-received region 71.3 % of the actuator's active strain was recovered. Following actuation of the as-received region the temperature of the actuator was above 19.5 °C, the A_f temperature of the as-received material, and the stress reached 274 MPa. Therefore, the properties of the laser processed region must be considered under these conditions. Tensile tests performed at 30 °C for the processed material are therefore more representative at this stage of actuation. Since the stress has increased in the actuator following the first actuation and σ_m has decreased due to temperature effects, the strain in the laser processed region has increased to 2.8 % as indicated by (iii) in Figure 43 b). The initial 2.8 % strain in the laser processed region was 25 % of the total initial pre-straining in the actuator, corresponding well with the 28.9 % recovery of active strain following the actuation of the laser processed region (Figure 41 b) and Figure 42 b)). Hence, the interactions between the two different regions of the processed actuator having different thermomechanical properties becomes apparent and the smaller active strain compared to the as-received actuator (Figure 41 b)) was explained. This result highlights new design considerations that must be taken into account when applying laser processing to NiTi SMAs.

4.5. Cyclic SME performance

The cyclic performance of NiTi SMAs, although not discussed until this point, is of great interest due to historically poor performance [46]. During processing of SMAs for actuation applications it is critical to overcome the continual build-up of residual strain (ε_p) during cyclic actuation to ensure consistent performance over the component's service life. The results from the 200 cycle actuation test are shown in Figure 44. The ε_p in the laser processed actuator caused by cyclic degradation was found to stabilize after approximately 150 cycles. Similar results have previously been presented in literature where cyclic degradation accumulated during each loading cycle will stabilize between 100 – 200 cycles [138-140]. This stabilization is the result of the reorientation/stabilization of preferred martensite variants and development of dislocations during early cycles. Different thermomechanical treatments have been found to affect how quickly this stabilization process occurs as discussed by Sofla et al. [139]. More notably, the ε_r remains almost unchanged after 200 cycles where only a 0.6 % decrease was measured from the first and last cycle. Therefore, the low cycle performance of the laser processed material was comparable to traditional SMA materials.

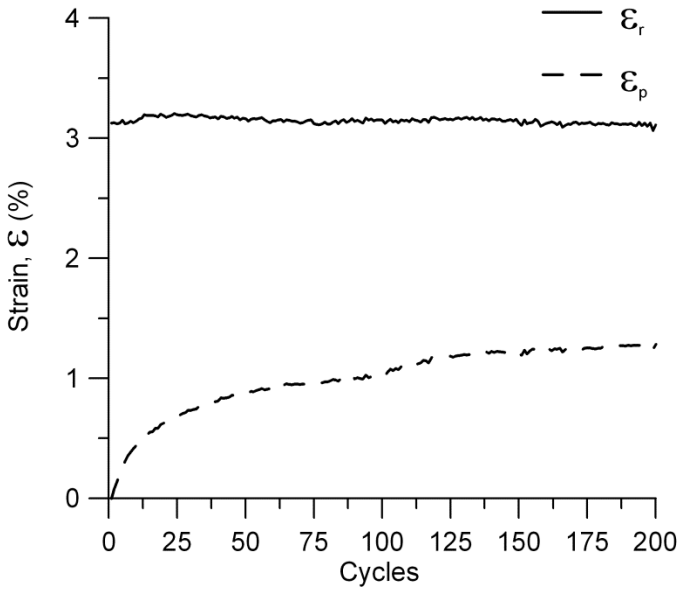

Figure 44: Recoverable strain (ε_r) and residual strain (ε_p) measured during cyclic actuation testing [133]

4.6. Chapter summary

In this chapter, a laser processing technology was demonstrated to improve the functionality of a NiTi wire linear actuator by augmenting the SME properties. The addition of a second memory allowed for two distinct actuations using controlled resistive heating. The performance of this novel wire actuator was characterized and a better understanding of the SME properties of laser processed material was

obtained. Tensile tests identified significant differences in the stress-strain behaviour during the deformation of martensite in the as-received and laser processed materials. Lüders-like deformation did not occur in the laser processed material. Instead, strain-hardening took place during the reorientation of martensite. Also, the σ_M was found to be substantially higher for the laser processed material due to higher phase transformation temperatures and the inherent temperature dependence of martensite stability. It is evident that more work is necessary to understand this laser process in order to select application specific phase transformation behaviour. Relationships between the process, structure and performance must be drawn before laser processes can be utilized to create useful devices.

5 Tuneable NiTi Shape Memory Alloy Functional Properties Through Combined Laser Processing, Cold work and Heat Treatment

In this study we explore the effects of Nd:YAG laser processing combined with subsequent cold work and heat treatment for the first time. Precision control in manufacturing becomes increasingly complex following such a combined thermomechanical processing protocol; recall sections 2.3. – 2.6. Successful application was only possible with complete understanding of the process, structure and performance relationship and development of necessary correlations. Therefore, this study was focused on quantifying changes in composition and characterizing the microstructure of processed NiTi material. Correlations between the microstructure and performance metrics such as phase-transformation characteristics and tensile performance were also made. Specific focus was directed to enhancing the structural and functional properties of laser processed materials to demonstrate unique performance offerings realized through application of this novel combination of SMA processing techniques. Recall the post-processing protocol used in this study included 27 % cold work (i.e. reduction in thickness) followed by subsequent heat treatment for 3.6 ks at 673 K (400 ^{o}C).

5.1. Results

5.1.1. Composition analysis

The number of pulses per laser spot was found to be the best method for controlling changes in transformation temperatures using vaporization based laser processing protocol [72]. In this study using micro-PIXE analysis the composition change with each laser pulse was measured, clearly identifying the relationship between the number of laser pulses parameter and resulting Ni:Ti ratio of the bulk material, shown in Figure 45. The base material (BM) Ni composition was measured to be 50.8±0.21 at.% which agreed well with the nominal composition of 50.7 at.% provided by the material manufacturer. The slope of the linear fit indicated that after each laser pulse the Ni composition decreases by 0.16 at.% implying precision control of the process and resulting alloy composition. Composition homogeneity was also investigated by taking composition measurements from three different regions of the single pulse laser spot, as illustrated in Figure 45. The composition within the laser spot was found to be uniform where an average composition of 50.71±0.03 at.% Ni.

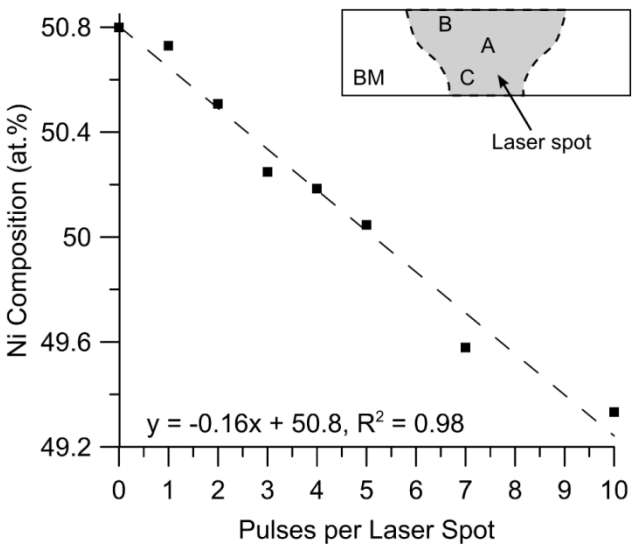

Figure 45: Ni composition versus number of pulses per laser spot, measured at location A of the inset illustration using micro-PIXE with an error of ± 0.21 at. %. Measurements were also taken at points B and C to asses composition homogeneity within laser spot

For the remainder of this study it was necessary to overlap laser spots to ensure that the whole sample area was processed. The 1 pulse per spot (1P) and 2 pulses per spot (2P) laser parameters were selected because with overlapping in both the x- and y-directions, the final composition change in the sample was significantly higher than that of the single spot results provided in Figure 45. Avoiding a Ti-rich alloy was desired to prevent the formation of Ti-rich intermetallics such as Ti_2Ni, which can lead to embrittlement and solidification cracking [141]. In both the 50% overlapped 1P and 2P conditions the composition remained Ni-rich with measured Ni concentrations of 50.46±0.15 at.% and 50.16±0.15 at.% respectively.

5.1.2. Thermoanalytical characteristics

The DSC results from the BM, 1P, 1P with cold work (1P+CW), 1P with cold work and heat treatment (1P+CW+HT), 2P, 2P with cold work (2P+CW), and 2P with cold work and heat treatment (2P+CW+HT) samples are provided in Figure 46. The BM sample undergoes transformation between the parent, B2 austenite phase and the B19', martensite phase (Figure 46a)). Although two sets of phase transformation peaks were observed on both heating and cooling they were both identified as resulting from B19' ↔ B2 transformations due to large peak to peak hysteresis (i.e. > 25 K) between each set of phase transformation peaks [142, 143]. There are several mechanisms that could result in multiple martensite transformations in the BM sample as identified in references [60, 142, 143]. The 1P and 2P laser processed sample exhibit single stage transformation with measured peak to peak hysteresis of 26.4±1.7 K and 33.2±1.6 K respectively (Figure 46 b) & e)). The transformation temperatures increase

after laser processing with the 2P sample having the highest transformation temperatures (Table 5). Increasing phase transformation temperatures and hysteresis with decreasing Ni-content was expected and agrees well with literature [12, 48].

After cold rolling the phase transformation peaks of the 1P+CW and 2P+CW samples become shallow and wide while shifting to lower temperatures (Figure 46 c) & f)). A second peak also appears on the cooling portion of the curve. Shallow and wide phase transformation peaks are typical to cold worked microstructures since heterogeneity in internal stresses is created which broadens the range of transformation energy required for complete phase transformation [59, 60]. Large dislocation density has also been shown to suppress martensitic phase transformation all together, reducing heat of transformation [60].

Following heat treatment of the cold rolled samples the phase transformation peaks for 1P+CW+HT and 2P+CW+HT samples narrow, increase in intensity, and shift to higher temperatures (Figure 46 d) and g)). This is typically observed following a recovery and/or recrystallization process [144, 145]. Shifts in phase transformation temperatures to higher temperatures can however also be attributed to a decrease in the matrix Ni content through precipitation of Ni-rich, Ni_4Ti_3 intermetallics [146]. Partial cycle DSC scans confirmed the secondary phase transformation peak on the cooling curve as R-phase transformation due to the small peak to peak hysteresis (4.2 K) between the B2 → R and B19' → B2 phase transformations [142, 143]; shown in Figure 47 for the 1P+CW+HT sample. The phase transformation peaks in Figure 46 were therefore labeled accordingly.

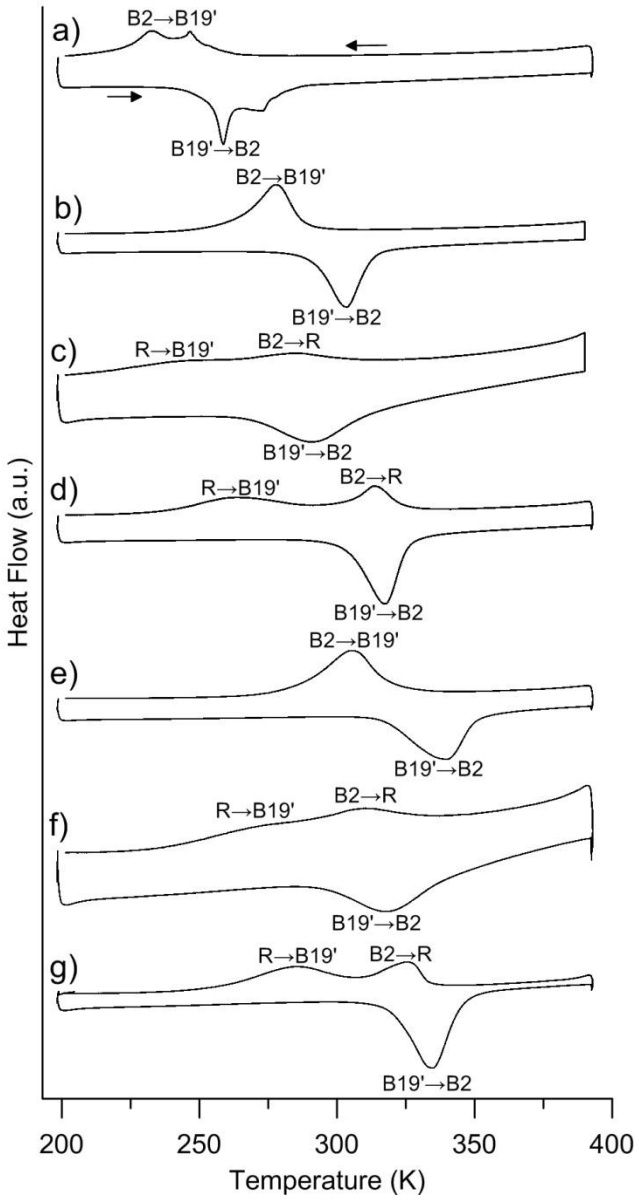

Figure 46: Differential scanning calorimetry results for a) base material (BM) sample, b) 1 pulse (1P) sample, c) 1 pulse with cold work (1P+CW) sample, d) 1 pulse with cold work and heat treatment (1P+CW+HT) sample, e) 2 pulse (2P) sample, f) 2 pulse with cold work (2P+CW) sample, and g) 2 pulse with cold work and heat treatment (2P+CW+HT) sample.

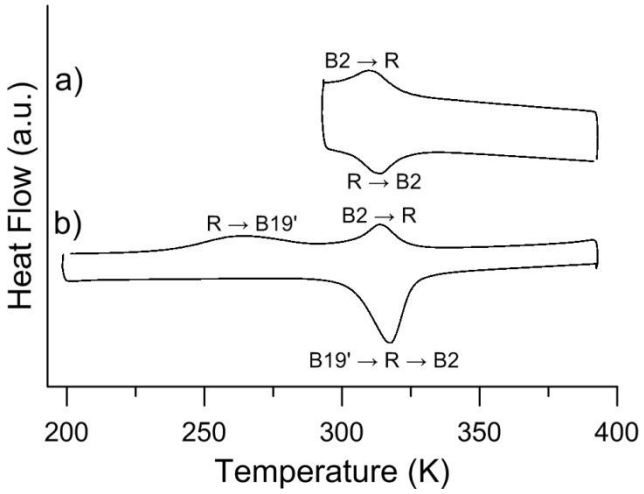

Figure 47: a) 1 pulse with cold work and heat treatment (1P+CW+HT) partial DSC scan between 293 and 393 K and b) full cycle DSC scan, identifying secondary peak as an R-phase transformation peak on the cooling curve

Table 5: Average phase transformation temperature for BM, as-processed and processed, cold worked and heat treated samples (K)

	R_s	R_f	M_s	M_f	A_s	A_f
BM	N/A	N/A	258.2±4.3†	218.7±3.4†	253.7±0.4†	284.1±2.1†
1 Pulse	N/A	N/A	291.6±3.2	263±2.4	293.2±2.2	317±3.5
2 Pulse	N/A	N/A	321.4±2.8	281±2.9	315.5±1.8	350±3.1
1P+CW+HT	326.1±0.8	305.4±1.1	281.2±5.1	231.7±6.7	300.2±2.3	326±1.1
2P+CW+HT	334.6±0.8	-- ‡	-- ‡	262±9.6	319.1±2.4	348.3±1.6

†Two sets of B2 ↔ B19' phase transformation peaks were overlapping and therefore were considered to be one large peak when recording phase transformation temperatures

‡B2 ↔ R and R ↔ B19' peaks overlap and therefore phase transformation temperature was not measured

5.1.3. Functional properties

Representative results from cyclic tensile testing, performed up to 6 % strain at temperatures of 293, 333, and 353 K are provided in Figure 48 for the as-processed 1P and 2P tensile specimen. At 293 K both the 1P and 2P specimen were in the B19' martensite phase (Table 5). Therefore, upon loading deformation of the tensile specimen proceeds by detwinning of the martensite phase and this strain was not recovered upon unloading (Figure 48 a) and d)). Subsequent heating of the specimen above the A_f temperature however did lead to the recovery of strain due to SME. The extent of the strain recovered

was measured and illustrated with an arrow and circle symbol on the x-axis of Figure 48. At 333 K the 2P sample was still in the martensite phase due to higher A_s temperature (Table 5) and therefore behaved similarly to the specimen tested at 293 K. The average residual strain following the SME was found to be below 0.9 % for both the 1P and 2P specimen. Above the A_f temperatures of the 1P (326±1.1 K) and 2P (348.3±1.6 K) samples the tensile specimen deformed plastically and the residual strain was greater than 3.5 % following unloading of the stress (Figure 48 b), c) and f)).

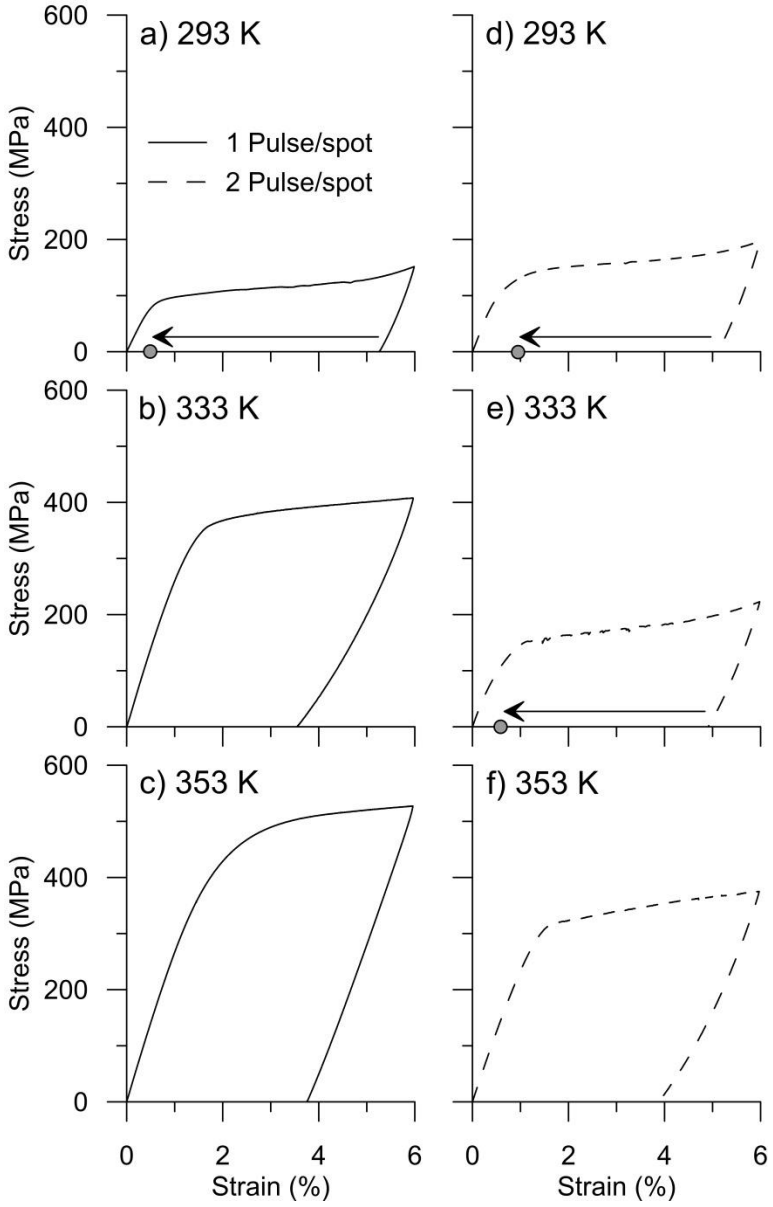

Figure 48: Representative results for the cyclic tensile testing of as-processed material performed at 293, 333, and 353 K. Curves a), b) and c) correspond to the 1P sample while curves d), e) and f) correspond to the 2P sample. The arrow and circle symbol denote the average strain recovered due to the SME upon heating the samples above their respective A_f temperature.

Representative results from cyclic tensile testing of the 1P+CW+HT and 2P+CW+HT tensile specimen are provided in Figure 49. The most notable change in cyclic tensile performance was that the tensile specimen exhibit PE when cycled at temperatures above their respective A_f phase transformation temperatures (Figure 49 b), c), g) and h)). Therefore, cold rolling and heat treatment restored the PE property of the previously laser processed SMA. A minimum average residual strain of 0.35 % was achieved with the 1P+CW+HT specimen at 333 K (Figure 49b). Following a Clauseus-Clapeyron relation (equation (1)) the PE plateau stress increases with temperature at a rate within the 3 – 20 MPa/°C range as sited in section 2.2.2. As a result, for both the 1P+CW+HT and 2P+CW+HT specimen the PE plateau stress becomes quite high at 363 K and the return plateau was found to become sloped (Figure 49 g) and h)). The sloped return plateau was also accompanied by a larger residual strain. This phenomenon had previously been observed when the temperature at which the critical stress for permanent slip becomes lower than the stress to form stress induced martensite (i.e. M_d) was exceeded as shown in Figure 8 [30, 147].

At temperatures below A_f the 1P+CW+HT and 2P+CW+HT samples behave similarly to the as-processed samples, as shown in Figure 49 a), d) and e). At 353 K the 2P+CW+HT specimen exhibits both SME and PE (Figure 49 f)) due to incomplete phase transformation to the high temperature B2 austenite phase at the test temperature (Figure 46). The residual strain after SME recovery of the cold worked and heat treated specimen was less than 1.2 %, slightly higher than that of the as-processed material.

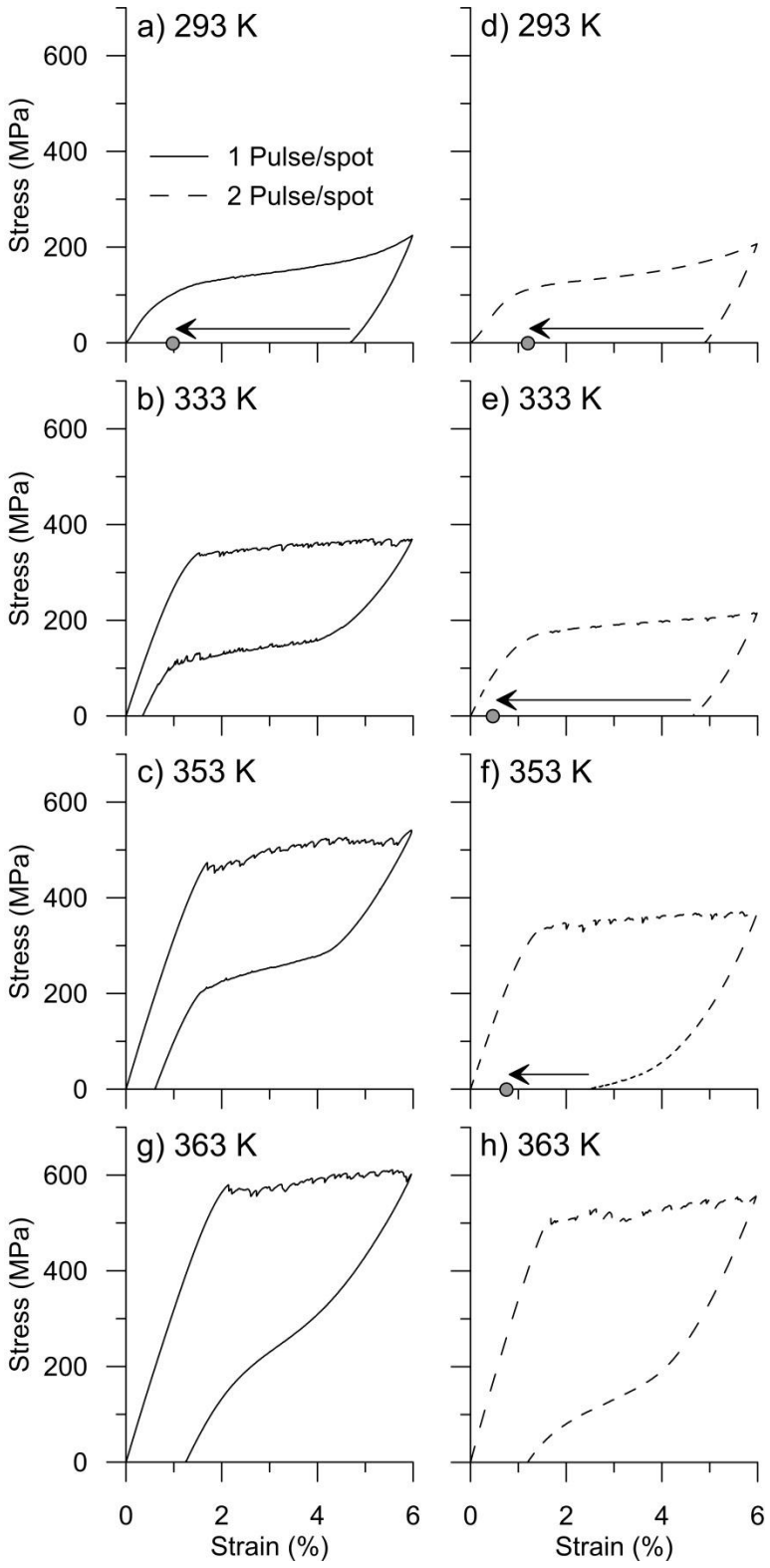

Figure 49: Representative results from cyclic tensile testing of cold worked and heat treated laser processed material performed at 293, 333, 353, and 363 K. Curves a), b) and c) correspond to the 1P+CW+HT sample while curves d), e), f) and g) correspond to the 2P+CW+HT sample. The arrow and circle symbol denote the strain recovered due to the SME upon heating the samples above their respective A_f temperatures.

5.1.4. Mechanical Properties

To determine the yield stress, ultimate tensile stress, and failure strain, tensile specimens were pulled to failure. Representative tensile test results for BM and the as-processed specimen (i.e. 1P and 2P) are provided in Figure 50 a). The results for the cold worked and heat treated specimen (i.e. 1P+CW+HT and 2P+CW+HT) are provided in Figure 50 b). Each of the curves in Figure 50 a) were quite different from one another. This was however expected since the phase transformation characteristics of the BM, 1P, and 2P samples varied (Figure 46). In fact, the BM sample was in the austenite phase at the test temperature of 293 K (20 °C) and the observed plateau resulted from the formation of stress induced martensite (SIM) while the 1P and 2P samples were in the martensite phase and the stress plateau resulted from the detwinning of the martensite phase. In general as-processed material was found to exhibit the largest strains at failure however they also had the lowest yield strengths (< 300 MPa) and ultimate tensile stresses (~500 MPa). Following subsequent cold rolling and heat treatment the yield stress of the laser processed material was improved significantly, where yielding was not observed to begin up to the failure load (Figure 50 b)). The shape of the 1P+CW+HT and 2P+CW+HT curves were very similar as both materials were in the martensite phase. However, the 2P+CW+HT sample had lower ultimate tensile strength and strain at failure. Both the 1P+CW+HT and 2P+CW+HT samples exhibited a more brittle like failure.

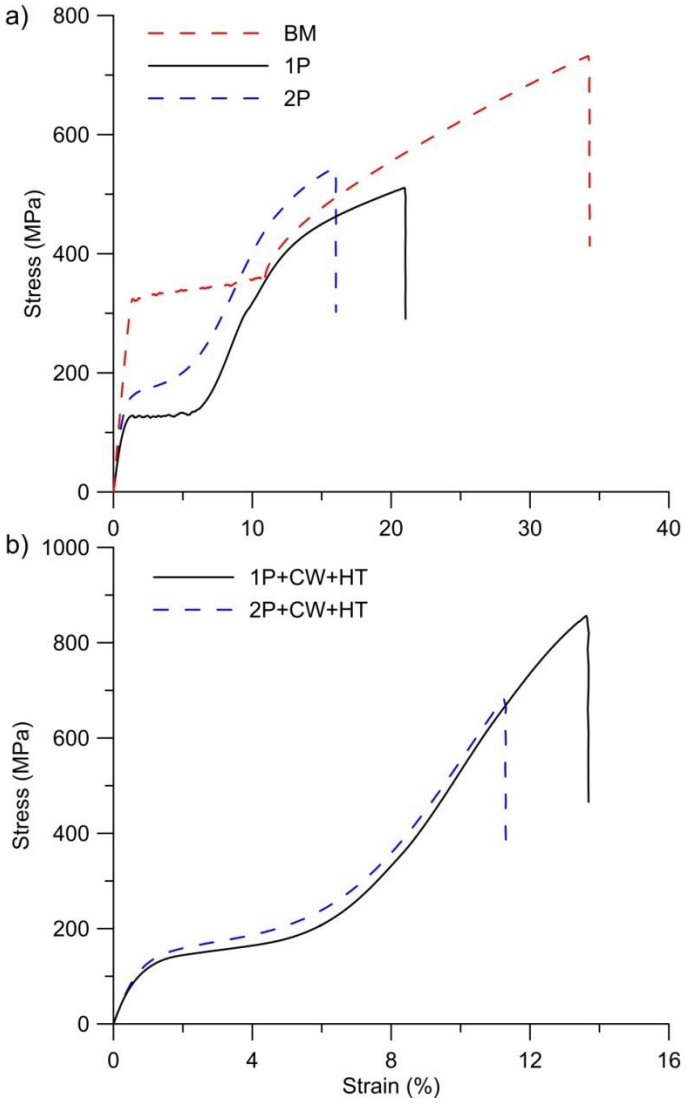

Figure 50: Tensile testing to failure at 293 K. As-received and as-processed sample conditions (BM, 1P and 2P) a), cold worked and heat treated sample conditions (1P+CW+HT and 2P+CW+HT) b)

5.1.5. Microstructure

The BM was found to have large (20 – 50 µm) equiaxed B2 austenite grains as shown in Figure 51 a). Large equiaxed grains are typical of annealed NiTi material [146]. Ti_2Ni inclusions were identified throughout the BM microstructure as indicated by an arrow in Figure 51 a) and shown at higher magnification in Figure 51 c). Selected area diffraction patterns were used to confirm the structure of the inclusions to be Ti_2Ni (Figure 51 d)). Energy dispersive x-ray spectroscopy analysis identified the average composition to be 65.34±0.67 at.% Ti, 32.35±0.84 at.% Ni and 2.31±1.27 at.% O. Oxygen has been found to be soluble in Ti_2Ni and not NiTi hence, the small amount found during EDS analysis [12].

The presence of the Ti-rich Ti_2NiO_x inclusions resulted from the casting process and they are commonly found in NiTi material [6].

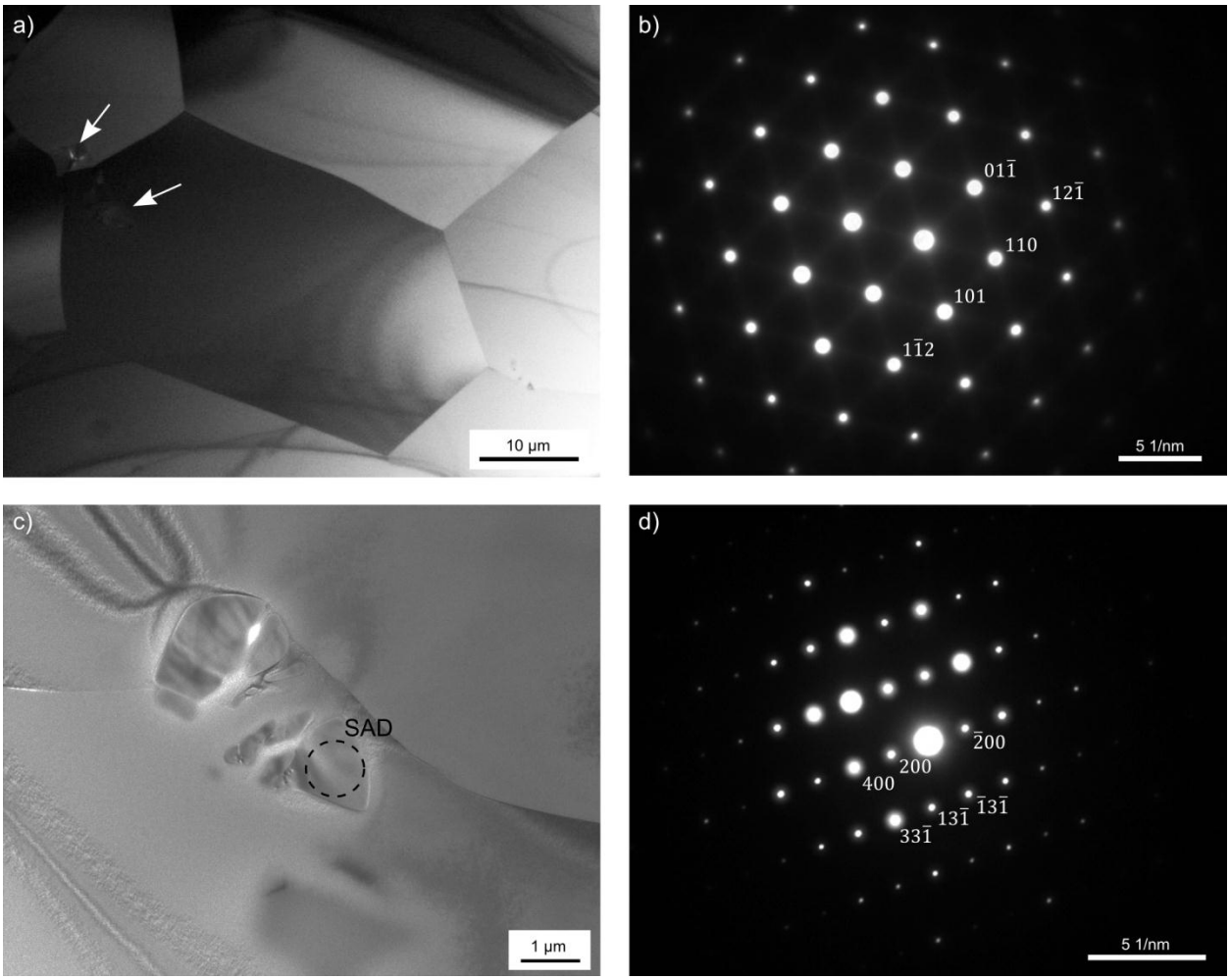

Figure 51: Microstructure of BM identified through bright field TEM images and SADPs. a) Large equiaxed B2 austenite grains with Ti_2NiO_x inclusions (marked with arrows), b) SADP B2 austenite $[\bar{1}11]$ zone axis, c) Ti_2NiO_x inclusion in B2 matrix, d) SADP for Ti_2Ni FCC structure $[013]$ zone axis

After laser processing the solidification structure was quite different from the BM microstructure as shown in OM images Figure 52 a) to d) for the 1P and 2P samples. Large columnar dendritic parent grains were observed growing from the edge of the laser spot towards the center; typical for a pulsed laser process [74, 89]. Epitaxial growth during solidification can be seen from the edge of the overlapping laser spots (Figure 52 a) and b)). Surface relief was observed due to the presence of martensite lathes in the 1P sample as indicated by arrows in Figure 52 a) and c). These martensite lathes were only observed in certain areas due to an incomplete martensitic phase transformation at room temperature (298 K); post-mechanical grinding and polishing of the sample. The 2P sample however

etched darker as the whole sample contained a martensite lathe relief pattern resulting from completed martensitic transformation. Also, an increase in the amount of the dark etching phase was observed in the 2P sample (Figure 52 d)). From TEM analysis the large prior austenite grains identified in Figure 52 were found to contain many different martensite variants due to self-accommodation of stresses (Figure 53 a) and b)) [4]. In general, the phases identified via SADP analysis validated the DSC peaks identified in Figure 47. The 1P sample contained domains of both the B19' and B2 phases, again due to incomplete transformation at the test temperature (298 K) consistent with the OM findings (Figure 52). The 2P sample was in the B19' martensite phase as shown in Figure 53 b). The B19' martensite phase was observed by twinning in TEM images and SADP of the 2P specimen shown in Figure 53 c). Moreover, with heating twinned martensite variants disappeared as they transformed to the B2 austenite phase as shown in Figure 10 d) and e) at temperatures of 298 K and 373 K respectively, confirming large parent grains in the laser processed material.

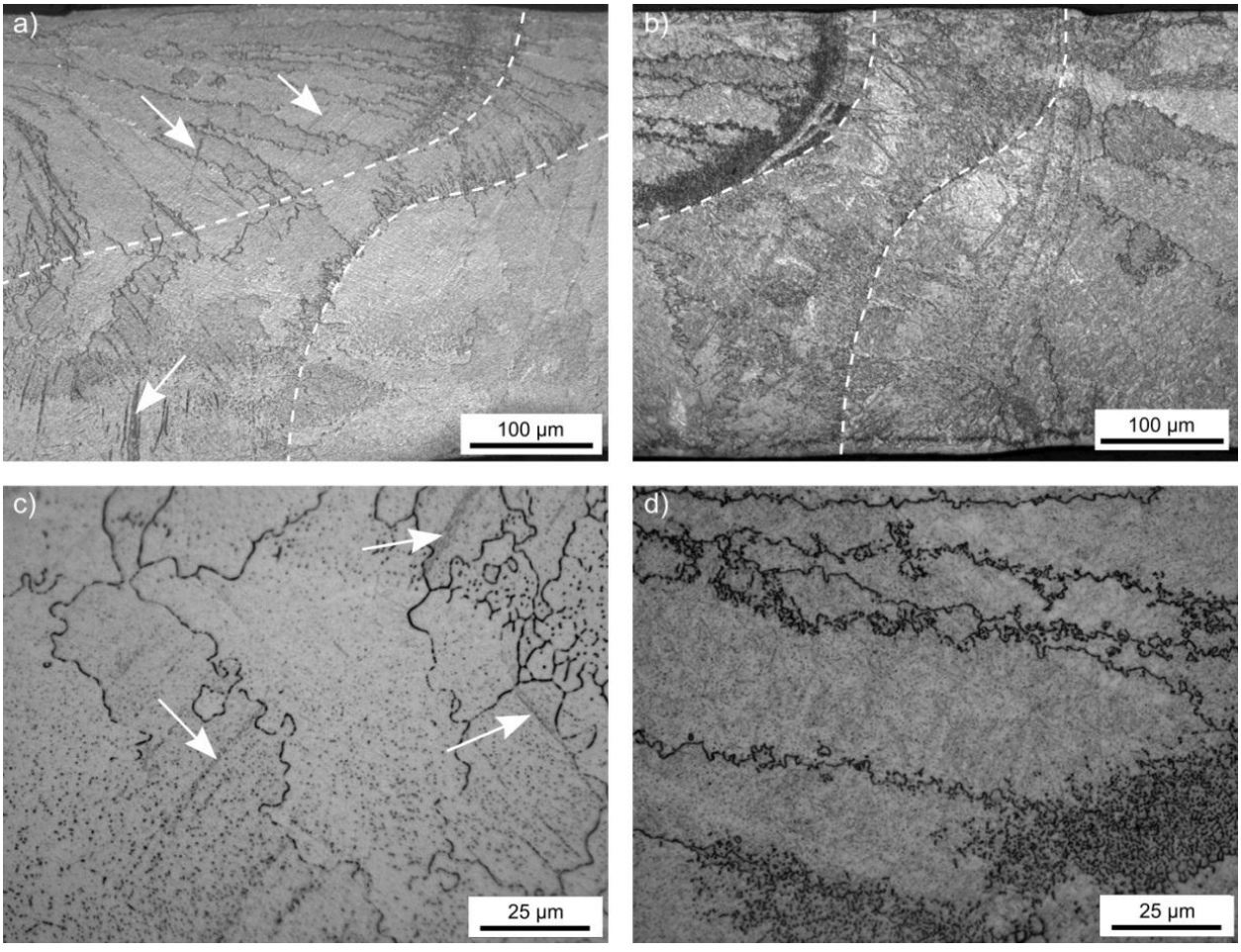

Figure 52: Low magnification OM image of a) 1P sample and b) 2P sample. High magnification OM images of c) 1P and d) 2P samples. Dashed lines indicate boundaries between overlapping laser spots

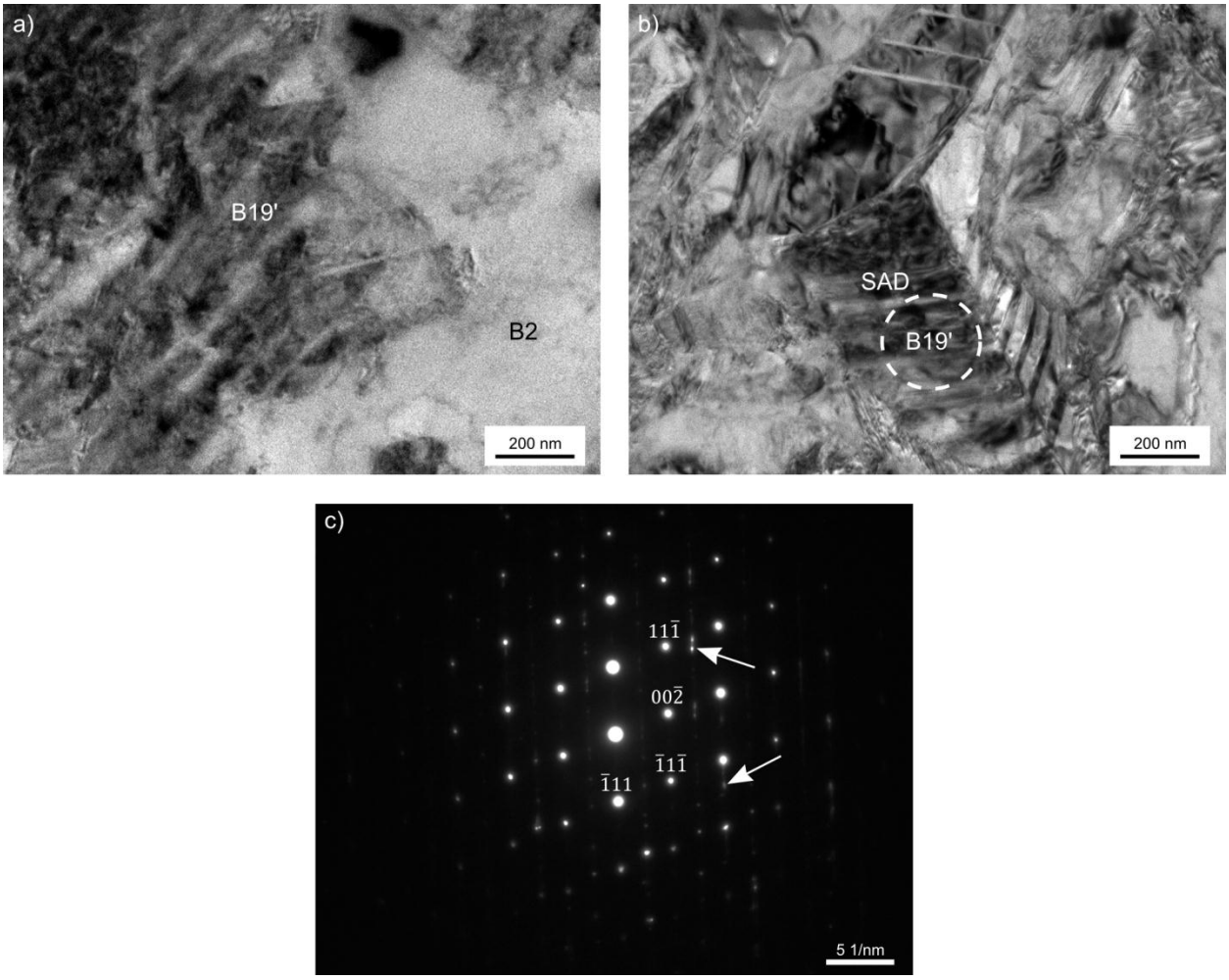

Figure 53: Microstructure laser processed 1P and 2P samples. a) Bright field TEM image 1P sample and b) 2P sample, c) SADP of twinned B19' martensitic structure $[110]$ zone axis

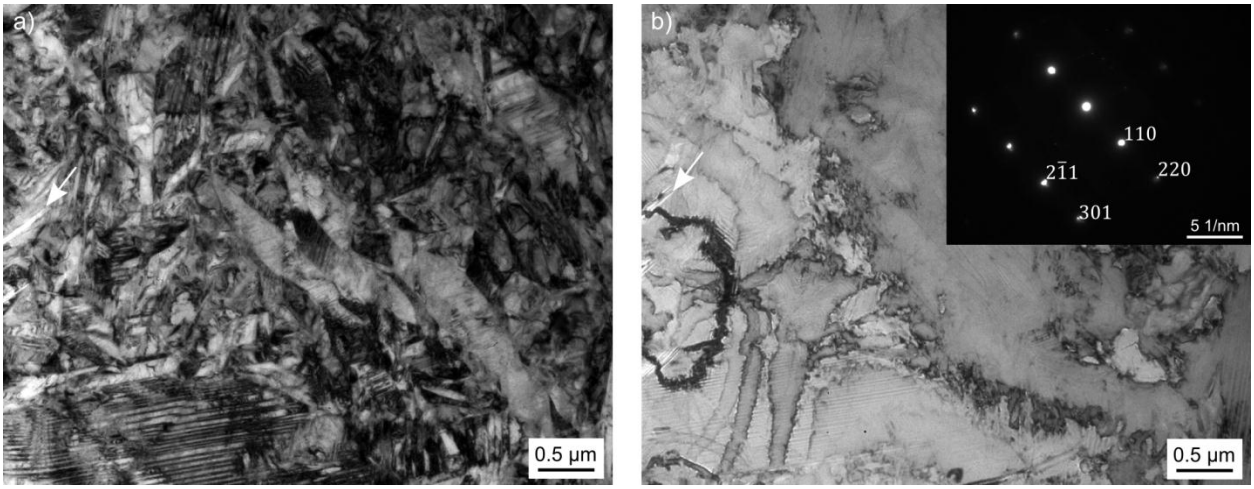

Figure 54: a) Low magnification bright field TEM image of 2P sample at 298 K and b) at 373 K (inset SADP of B2 austenite structure $[\bar{1}13]$ zone axis). Arrows indicates identifying feature between figures a) and b)

The large Ti_2NiO_x inclusions found in the BM (Figure 51 c)) were not found in the laser processed material as they were likely dissolved during laser melting. Instead, fine Ti_2Ni and Ti_2NiO_x precipitates were found primarily at the boundaries between dendritic grains due to micro-segregation using STEM (Figure 55 a)) having average composition of 61.22±2.68 at.% Ti, 32.41±3.13 at.% Ni and 6.37±3.2 at.% O. This finding agrees well with the optical micrographs of Figure 52 where etching preferentially dissolved the Ti_2NiO_x phase. Through EDS analysis fine (< 100 nm) Ti-rich precipitates having an average composition of 80.49±8.3 at.% Ti, 4.93±5.53 at.% Ni, and 14.51±6.51 at.% O were also observed as shown in Figure 55 b). These precipitates were not identified explicitly in this study but were also observed in a laser welding study by Shloβmacher et al. [82]. In contrast, Ni-rich precipitates were not identified in as-laser processed material. Due to the composition being near stoichiometric NiTi in the laser processed material and high cooling rates inherent to the pulsed laser process the Ni_4Ti_3 precipitates did not form. Similar results were found by Kompatscher et al. [149] in solutionized and quenched near equiatomic NiTi.

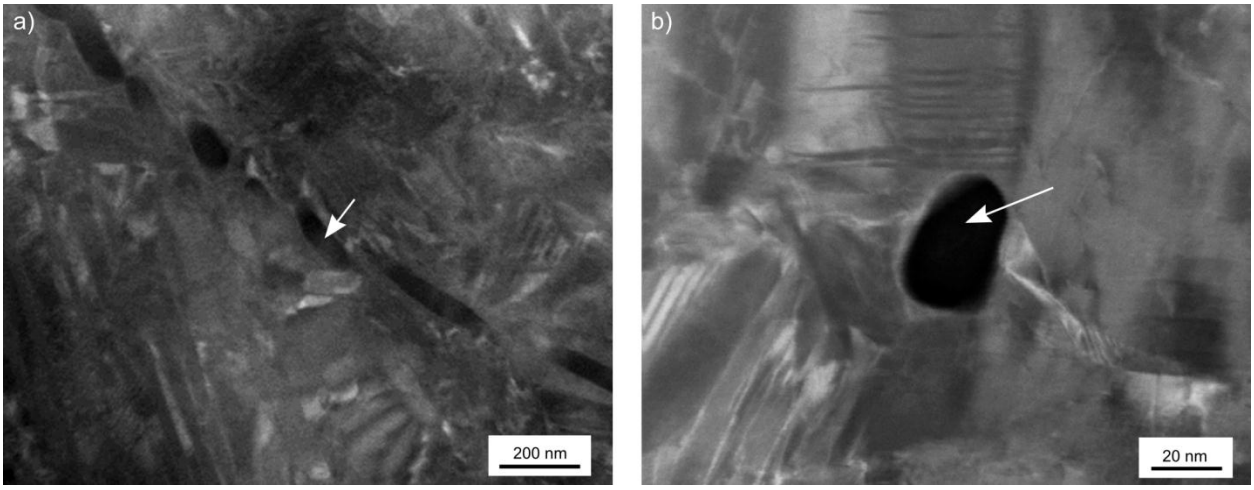

Figure 55: Precipitates identified using STEM analysis. a) Image of Ti_2Ni precipitate (59.8 at.% Ti and 40.2 at.% Ni) at grain boundary in 2P sample and b) Ti-rich inclusion (84.5 at.% Ti, 1.7 at.% Ni, and 13.8 at.% O) in 2P sample. Arrows indicate location of EDS analysis

Following cold rolling and heat treatment of the laser processed material; fine martensite variants were found to reside in large elongated parent grains. R-phase was identified through the DSC results of Figure 46 and SADPs taken during TEM analysis of the 1P+CW+HT specimen (Figure 56 a) and b)). Typical $1/3\langle 111\rangle_{B2}$ superlattice reflections originating from the R-phase [28, 150] were clearly observed in Figure 56 b). R-phase and fine B19' martensite variants are typically found in cold worked and heat treated materials [4, 28]. Dislocations and fine coherent Ni_4Ti_3 precipitates combined with the large transformation strains of the B19' martensite phase prevent large variants from forming while

promoting the formation of R-phase due to an inherently lower transformation strain as discussed in section 2.1.1. [151]. The fine structure of the cold worked and heat treated specimen made microstructural analysis difficult as shown in Figure 56c) for the 2P+CW+HT specimen. From SADP analysis of the fine structured regions, nano-crystallites were identified having specific texture, likely inherited from the parent grain [152, 153]. Diffractions spots form B19' martensite and R-phase were identified along with some extra spots which were attributed to fine oxide inclusions. Also, arched spots indicated the strained state of the crystal lattice.

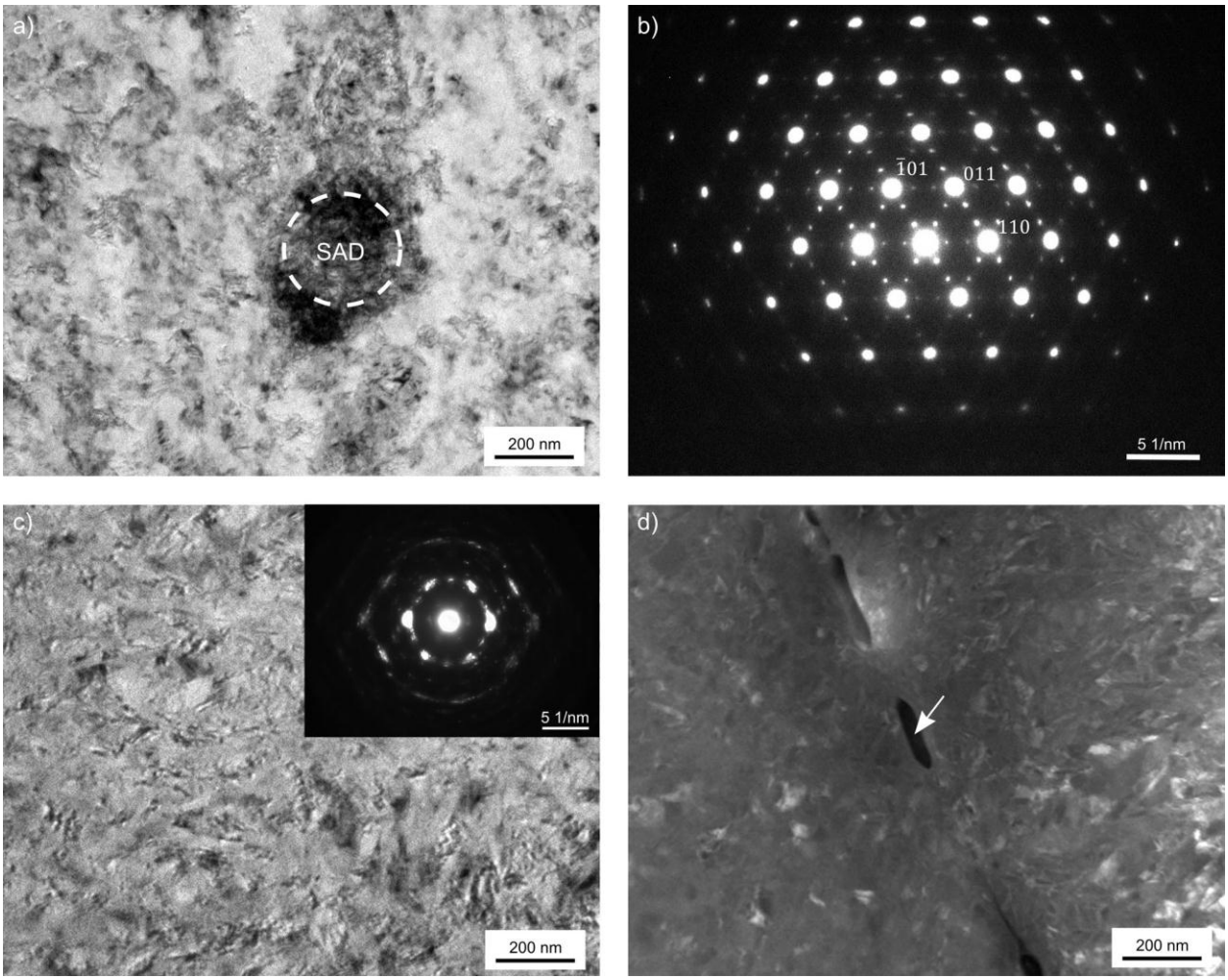

Figure 56: Microstructure of 1P+CW+HT and 2P+CW+HT samples. a) Bright field TEM micrograph of 1P+CW+HT specimen, b) SADP of R-phase ($[1\bar{1}1]$ zone axis) in 1P+CW+HT specimen, c) bright field TEM micrograph of 2P+CW+HT specimen (SADP inset image), and d) STEM image of Ti_2NiO_x (63 at.% Ti, 31.8 at.%Ni, and 5.2 at.% O) precipitate at prior dendritic grain boundary

The Ti_2NiO_x precipitates were again observed at the prior dendritic grain boundaries as shown in Figure 56 d). They were however partially broken up and displaced due to the cold working. Even solutionizing heat treatments are unable to dissolve Ti_2Ni precipitates due to their inherent stability [154], hence it

was expected they would remained after cold rolling and 673 K heat treatment. The Ti-rich phase was found to remain seemingly unaffected. Ni_4Ti_3 precipitates were still not observed in the cold rolled and heat treated laser processed material even though the 3.6 ks, 673K aging has been shown in several other studies to produce fine coherent precipitates (10 – 30 nm) in near equiatomic NiTi alloys [58, 144, 151].

5.2. Discussion

With the results presented in this study we can now discuss critical relationships between the laser, cold rolling, and heat treatment processes and the resulting microstructure and performance. Using in depth understanding of this combination of processing techniques and the relationships developed herein it was demonstrated how tunable, locally graded functional properties were embedded in monolithic NiTi SMA materials.

5.2.1. Phase transformation temperature versus composition relationship

Laser induced vaporization occurs due to the high temperatures reached within the laser spot [100-102]. Since Ni has a higher vaporization pressure than Ti (Figure 21) it was deduced that the flux of the Ni alloying constituent leaving the molten NiTi pool will be greater than that of Ti. As a result the overall Ni composition of the re-solidified NiTi material will have reduced as suggested in section 2.6. Through accurate measurement of the composition in this study via Micro-PIXE spectroscopy the vaporization mechanism behind augmented transformation temperatures has now been definitively proven. Surprisingly, with each laser pulse a precisely controlled decrease in Ni composition was possible (i.e. -0.16 at. % Ni/laser pulse) as identified in Figure 45. If we now plot the change in composition after each laser pulse (i.e. 1 – 10 pulses per spot) against the respective M_s transformation temperature we observe the relationship between the phase transformation characteristics of pulsed laser processed material and Ni:Ti ratio, shown in Figure 57. This relationship for NiTi SMAs has been identified as critical for meeting application specific performance demands and therefore the basis behind thermodynamics based models, such as those developed by Tang [48] and more recently by Frenzel et al. [12] shown in Figure 14. For the Ni-rich laser processed samples (i.e. 1 – 5 pulses per spot), as the Ni composition increases, M_s decreases at a rate of -72.36 K/at.% Ni. This result agrees very well with -83 K/at.% Ni found by Frenzel et al. [12]. The 10.64 K/at.% Ni discrepancy between the results of Figure 57 and the model created by Frenzel et al. [12] can be explained by oxygen and carbon pick-up which was not accounted for in this work. Multiple melt procedures are traditionally used to homogenize NiTi material composition but with each melt the cumulative amount of oxygen and carbon picked-up increases [12].

It is logical to assume that a similar phenomenon occurs during multiple laser pulses. Increasing oxygen and carbon content leads to an overall increase in the Ni-content of the matrix through the formation of Ti_2NiO_x and TiC, resulting in decreased M_s and hence would lead to a shallower slope to the trend observed in Figure 57. Once the laser process material became Ti-rich (i.e. > 5 pulses per spot) the M_s temperature was found to stabilize at 338 K (65 °C) due to Ti saturation (Figure 57). With decreasing the Ni:Ti ratio further, Ti_2Ni is precipitated while the matrix composition remains constant resulting in no change in the M_s phase transformation temperature [12, 48]. The critical relationship between Ni concentration and phase transformation temperatures has therefore been proven using NiTi alloys created by laser induced vaporization in this study.

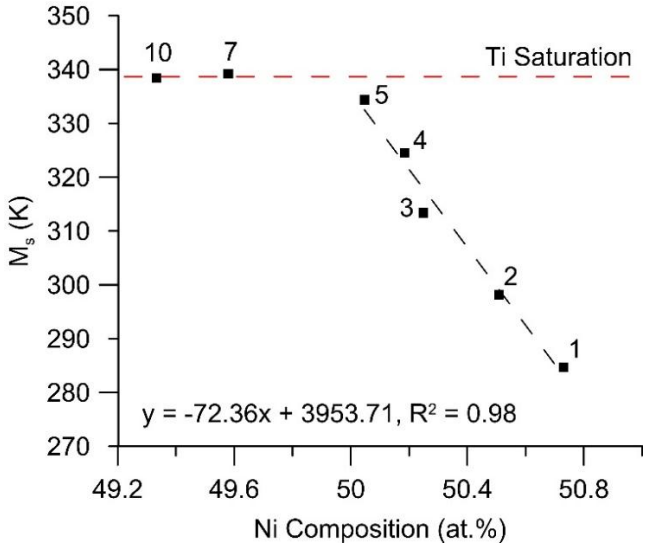

Figure 57: M_s phase transformation temperature versus Ni composition of the single laser spot 1-10 pulse samples. Number of laser pulses per spot identified above each respective data point

Through adjusting laser parameters such as, peak power, pulse time the temperatures within the laser spot as well as the interaction mode between the laser energy and the material (i.e. conduction or keyhole mode) will change, affecting vaporization flux. This effect has been modeled by He et al. [100, 101] and Jandaghi et al. [102] for the conduction and keyhole laser modes respectively. Therefore it is proposed that by using combinations of laser parameters and pulsing schedules, any desired composition in a binary NiTi component can be achieved with great compositional and positional precision, further highlighting the great potential of the now proven laser induced vaporization process.

5.2.2. Relationship between structural and functional properties of laser processed NiTi

Previous studies characterizing structural and functional properties of laser processed NiTi alloys exclusively investigated laser welds [82-89, 148]. In each of these studies during cyclic tensile testing

yielding takes place in the laser processed region resulting in increased residual strain. The effects of past material treatments such as cold work and precipitation hardening were lost following the thermal cycles of laser processes, reducing the yield stress [82, 84, 87]. As shown in Figure 48 a), 6d) and 6e), both the 1P and 2P as-processed materials exhibited SME at temperatures below their respective A_s phase transformation temperatures with less than 0.9 % residual stress. However, when cycled above their A_f temperatures significant plastic deformation occurred and PE was not possible with residual strains greater than 3.5%. From Figure 50 it was observed that the yield strength of the 1P and 2P as-processed material was between 300 and 350 MPa. The PE plateau stress was therefore higher than the critical stress to induce slip (i.e. yield stress) resulting in the permanent deformation of the tensile specimen (Figure 48 b), c) and f)). A similar phenomenon was observed by Shloβmacher et al. [148] who conducted the only other study investigating the tensile performance of a completely laser processed specimen. Without cold work and/or fine coherent Ni-rich, Ni_4Ti_3 precipitates, which have been shown to be very effective at blocking dislocation motion in NiTi alloys [46], the yield stress of laser melted material was therefore too low for PE to occur, as illustrated in Figure 9. Since the martensite detwinning stresses of the 1P and 2P samples (< 200 MPa) were observe to be below the yield stress of the material (Figure 50 a)), the SME property of as-laser processed material could however still be utilized. Similar findings were arrived at by Tuissi et al. [87] regarding the ability to use laser welded NiTi for low stress SME applications as well as in Chapter 5 in developing the laser processed linear actuator. Limitations in functionality of as-laser processed material have therefore now been identified where only the SME is possible in as-laser processed material because the martensite detwinning stress remains below the yield stress.

In addition to reducing the yield stress, laser processing has also been shown to reduce the ductility of NiTi alloys [82-85]. The columnar dendritic microstructure with Ti_2Ni and Ti_2NiO_x intermetallics populating the grain boundaries has been cited as the mechanism behind reduced ductility and partially brittle failure of laser processed NiTi alloys [86]. These Ti_2Ni and Ti_2NiO_x phases were observed in the laser processed material in this study (Figure 55 a) and Figure 56 d)) therefore explaining reductions in ultimate tensile strength and failure strain observed in Figure 50 a). The 2P sample was observed to have a relatively larger amount of Ti_2Ni and Ti_2NiO_x intermetallics (Figure 52 b)) likely resulting from lower Ni:Ti ratio and higher oxygen pick-up [12]. Therefore, it was not surprising that the strains at failure were observed to be lowest in the 2P specimen. However, the maximum strain at failure was always above 10% strain for the as-processed material (Figure 50) indicating that full use of the SME was possible, since the maximum recoverable strain of polycrystalline NiTi SMAs is approximately 8 % [44].

5.2.3. Effects of post-process cold work and heat treatment

It has become quite clear that in order to improve the functional performance of laser processed NiTi SMAs the yield strength must be increased. Post-processing heat treatment at 673 K (400 °C) for 3.6 ks was shown by Yan et al. [88] to improve fatigue properties of laser welded NiTi. Similarly, heat treatments at 623 k (350 °C) for 3.6 ks were shown by Chan et al. [89] to improve the structural and PE properties. In both of the aforementioned cases, improvements in fatigue and functional performance were attributed to precipitation hardening effects resulting from coherent Ni_4Ti_3 precipitates. Heat treatments at higher temperatures (i.e. > 723 K) however were found to have little to no effect due to the substantially larger size of the precipitates formed [89]. It has been found that Ni_4Ti_3 precipitates lose their coherency and therefore their effectiveness at blocking dislocation motion when they reach sizes greater than 150 – 300 nm [57] depending on degree of cold work, where this critical size has been suggested by Treppmann et al. [155] to decrease with increasing cold work.

In this work, cold rolling was performed by reducing the thickness of the laser processed NiTi material 27 % before the 673 K (400 °C), 3.6 ks heat treatment. The combination of cold work and ageing heat treatments is most effective at increasing the critical stress to induce slip (i.e. yield strength), as summarized by Otsuka and Ren [4]. The resulting combination of work-hardening and precipitation hardening allows for more perfect SME and PE properties, larger ranges of temperatures at which PE can occur [4], and more stable performance in low cycle experiments (Figure 44) [35, 133]. As shown in Figure 49 b), c), g), and h), following cold work and heat treatment the 1P+CW+HT and 2P+CW+HT laser processed materials again exhibit PE. Therefore, the post-processing treatment effectively restored the PE properties of the laser processed material. The SME and PE performance of the 1P+CW+HT and 2P+CW+HT materials was however not perfect. Residual strains upwards of 1.2 % were found to result from both the SME and PE at the temperatures tested (Figure 49). From the metallurgical analysis, Ni_4Ti_3 precipitates were not identified. It is therefore possible that the post-processing schedule in this study was therefore a cold work and 673 K (400 °C), 3.6 ks anneal opposed to an aging heat treatment. Miyazaki et al. [50] was able to achieve SME and PE properties in a Ti-rich, 49.8 at. % Ni cast alloy using a similar cold work and anneal protocol. The near equiatomic compositions of Ti – 50.46±0.15 at.% Ni and Ti – 50.16±0.15 at.% Ni of the 1P and 2P specimen may have contributed to Ni_4Ti_3 precipitates not forming in laser processed material [149]. In creating a functionally graded laser processed material it would therefore be beneficial to start off with a material with higher Ni content and fine tune the functional and structural properties using the final aging step of the combination processing protocol. This may also mitigate the formation of Ti-rich intermetallics that form due to microsegregation. It is

also known that a partially recrystallized structure with grain sizes in the order of 10 – 20 nm is ideal for PE with limited residual strains [152]. Although a fine partially recovered structure was identified after cold work and heat treatment in this study (Figure 56), fine recrystallized grains were not observed throughout the whole microstructure. Recrystallization was therefore in the early stages, likely having only occurred in the highest energy regions.

With optimization of the combined laser, cold work and heat treatment protocol it is expected that the functional performance of laser-processed NiTi material can be improved even further. It is proposed that by investigating different heat treatment temperature and times, precipitation of Ni_4Ti_3 precipitates will be found to occur. Also, introducing recrystallization heat treatments (e.g. at 873 K) at intermediate steps [58] in the cold working process will add grain refinement to the list of strengthening mechanisms applied to the laser processed material.

5.2.4. Unique performance offerings

It has been shown in several studies that through locally modifying the composition and/or microstructure of NiTi SMAs unique performance offerings can be realized. For example, Meng et al. [69] showed unique two-way SME actuation through partial laser annealing of NiTi strip, Daly et al. [70] laser alloyed Cu into NiTi strip locally augmenting phase transformation characteristics and tuning hysteresis, and finally the performance of multiple memory materials that exhibit multiple shape changes have been realized through the vaporization based laser processing protocol studied herein [71, 133]. All of the aforementioned studies however lack complete understanding of process and resulting structure. Therefore, the performance of the laser processed NiTi SMA was not ideal. For example, the PE property could not be achieved. Using the unique combination of laser processing plus post-process cold work and heat treatment in this study, two additional unique and desirable performance offerings via laser processing can now be achieved: 1) synergistic SME and PE and 2) multiple PE stresses in monolithic components.

Proof of concept showing a monolithic component with both PE and SME properties was demonstrated by creating a tensile specimen containing equal lengths of 1P+CW+HT and 2P+CW+HT processed material. This specimen was pulled to 8 % strain at a temperature of 333 K (60 °C) as shown in Figure 58 a). A combined effect of the SME from the 2P+CW+HT portion of the gauge length (Figure 49 e)) and the PE response of the 1P+CW+HT portion of the gauge length (Figure 49 b)) therefore occurs in zones (i) and (ii), respectively. Through introducing both SME and PE properties into a monolithic NiTi component a ‘self-biasing’ mechanism was achieved. The PE portion of the component can be used to store energy

created by the shape change of the SME region. With this mechanism the use of an independent biasing component (i.e. the spring in Chapter 4) [133] is no longer necessary for cyclic SME actuation. This 'self-biasing' concept allows for unprecedented functional performance of monoclinic SMA components, greatly increasing their functionality.

In Figure 58 b) multiple PE plateaus were achieved by processing only half of the gauge length followed by cold rolling and heat treatment. Zone (i) of Figure 58b) therefore corresponds to the PE response of the 1P+CW+HT condition (Figure 49b)) while zone (ii) represents the PE response of BM that has been cold worked and heat treated (BM+CW+HT). The protocol presented in this work provides an effective method to the locally tune PE stresses. This will greatly enable SMA based medical device technologies taking advantage of the biomimetic stress profiles by allowing for varying PE stresses throughout the component.

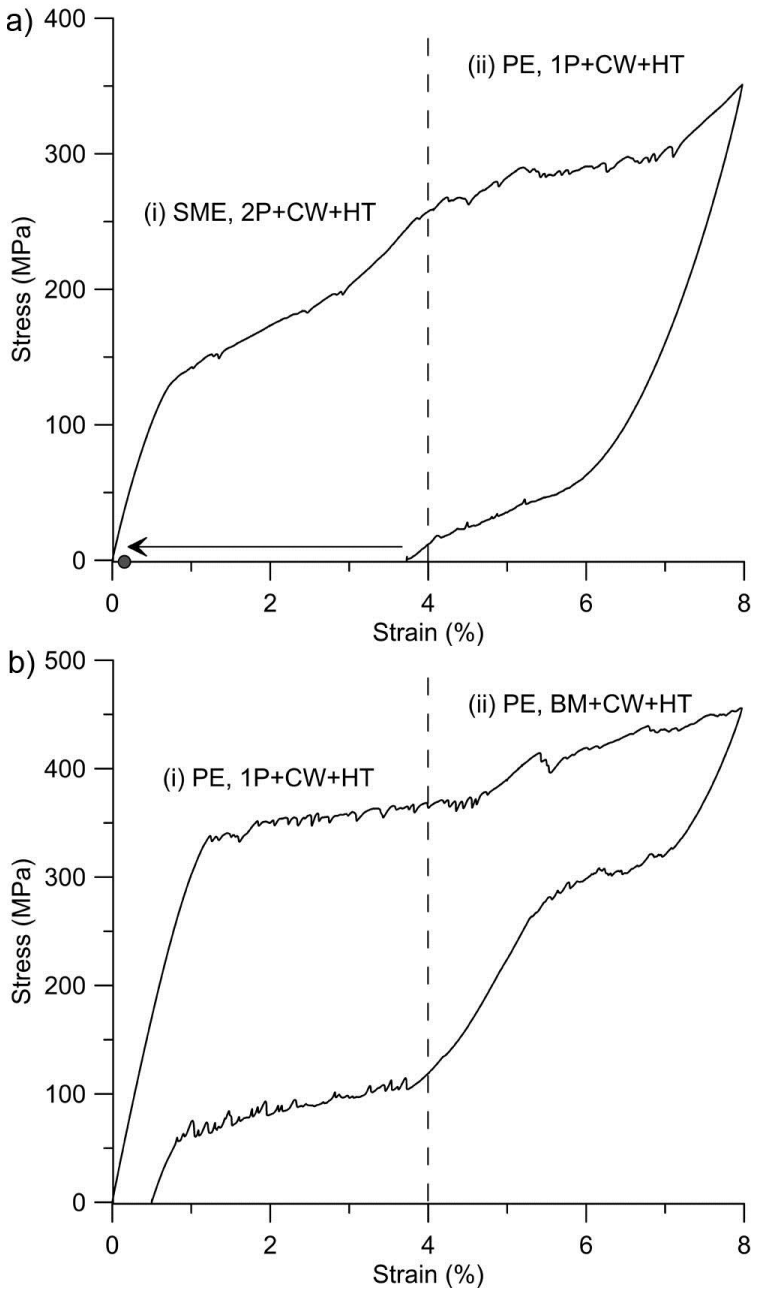

Figure 58: a) Half PE and half SME (i.e. 1P & 2P+CW+HT at 333 K), b) two PE plateaus (i.e. BM+CW+HT & 1P+CW+HT at 333K)

5.3. Chapter summary

In this chapter progress was made in the understanding of the laser induced vaporization process and the importance of post-processing techniques including cold work and heat treatment. The vaporization mechanism was finally confirmed using the high measurement accuracy of micro-PIXE spectroscopy. Remarkably, through accurate composition measurement great precision of the vaporization

mechanism with respect to the number of laser pulses per spot parameter was identified. This highlights the potential of this technology in locally tuning functional properties of monolithic NiTi components.

Combining local augmentation of transformation temperatures via the laser induced vaporization with post-processing cold work and heat treatment was found to restore the yield strength of laser processed material. As a result of the improved structural properties the PE property of laser processed material was observed for the first time.

Critical relationships developed between the process conditions, microstructure and SME, PE and mechanical performance provide a platform for further optimization of the combined laser processing and post-process techniques. The results from this study therefore promise substantial improvements in performance with further optimization of the post-processing protocol for example by precipitating Ni_4Ti_3 precipitates, creating favorable crystal texture and refining parent austenite grains.

6 Effects of Laser Processing on Surface Characteristics of NiTi Shape Memory Alloys

The aim of the present study was to investigate the corrosion and Ni ion release performance of pulsed Nd:YAG laser processed NiTi. Specific focus was directed on characterizing changes in surface characteristics and modification to the bulk material composition and microstructure. The contributions of this study aid in forming a more solid understanding of aspects surrounding the corrosion and biocompatibility performance of laser processed NiTi materials that have been inadequately addressed in literature to date; discussed in section 2.7.1. Note that the definition of biocompatibility used here pertains to a device that is passive in nature, meaning it does not interact with the living tissue or cells.

6.1. Results

In this comprehensive study the results presented below were obtained from experiments carefully designed to systematically uncover the bulk material properties of the CE, LP and LP-Pol samples, followed by their resulting surface conditions, and finally their corrosion and Ni ion release performance. First the bulk material was characterized using DSC analysis to identify the effects of laser processing on the thermoanalytical properties of the SMA as well as give insight into changes in Ti/Ni ratio. Optical microscopy was then used to understand the microstructure and identify secondary phases which may contribute to changes in the stability of the oxide layer. Next the surface characteristics of the CE, LP, and LP-Pol materials were fully characterized using optical profilometry, XPS, AES, and Raman spectroscopy to determine roughness, identify surface species present, and characterize the oxide thickness and degree of crystallinity, respectively. Finally, the performance of each of the NiTi samples was assessed using cyclic potentiodynamic corrosion testing and ICP-OES for identifying Ni ions released, allowing for further discussion on the process, property, and performance relationship as it applies to laser processed NiTi SMAs.

6.1.1. Thermal Analysis

From the DSC results shown in Figure 59 a) it was observed that following laser processing two sets of phase transformation peaks were present. The first set of peaks, at lower temperatures, corresponds to the BM and heat affected zone (HAZ) adjacent to the laser processed material. The second set of higher temperature peaks corresponds to the Ni depleted laser processed material; discussed in section 2.6. Figure 59 b) shows the location of the LP and BM/HAZ regions in the laser processed material. The phase transformation temperatures and peak to peak hysteresis are provided in Table 1. Large hysteresis

between phase transformation upon heating and cooling is typical of B2 austenite ↔ B19' martensite transformations in a binary NiTi alloy [142].

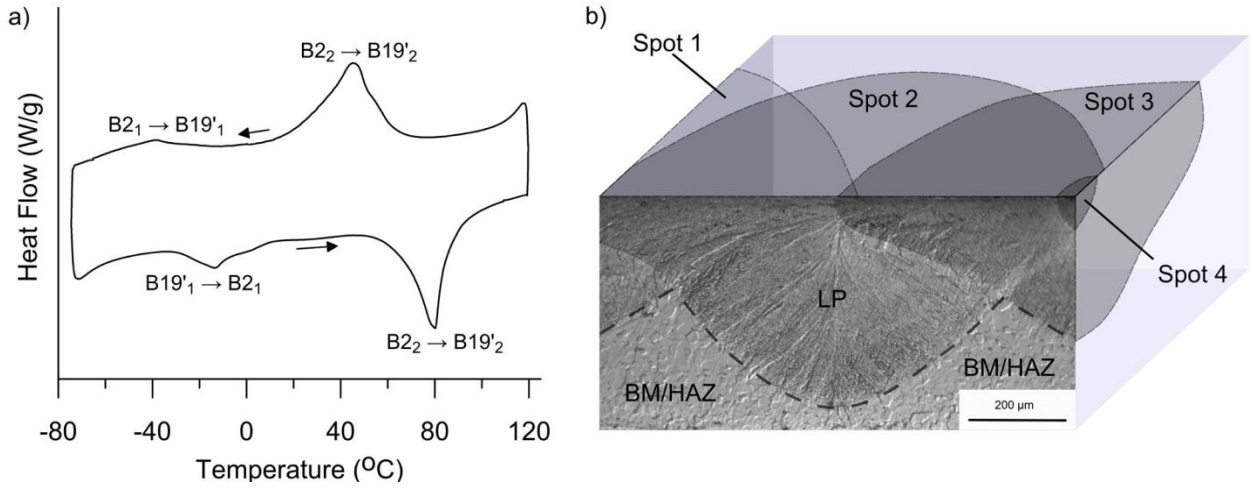

Figure 59: a) Differential scanning calorimetry (DSC) results for laser processed NiTi material and b) cross-sectional image of processed sample identifying the LP and BM/HAZ regions

Table 6: Transformation temperatures and hysteresis (i.e. measured peak to peak) from DSC analysis (°C)

	A_s	A_f	M_s	M_f	Hysteresis
BM/HAZ ($B2_1 \leftrightarrow B19'_1$)	-30.7	2.8	-21.6	-55.5	25.4
LP ($B2_2 \leftrightarrow B19'_2$)	59.6	87.8	64.9	19.5	35.1

6.1.2. Microstructure

The microstructure of cross-sectioned BM (i.e. CE) and LP material is provided in Figure 60. The BM showed an equiaxed grain structure (Figure 60a) with many large dark etching inclusions. These inclusions are common in NiTi alloys and have previously been identified as carbon and oxygen based inclusions resulting from the ingot casting process discussed in section 2.1. [79]. Within the solidified laser spot epitaxial growth of grains growing from the laser spot edge toward the center was observed (Figure 60 b) and c)). The aforementioned large inclusions were not present in the LP region; however, they were still detected adjacent to the laser spot in the HAZ (Figure 60 b)). High temperature thermal cycles during processing induced partial recrystallization in the HAZ as shown in Figure 60 b), where fine grains were identified (Figure 60 a)). At higher optical magnification, a finer secondary dark phase was observed within the LP region as shown in Figure 60 d). These phases were more prominent in the regions where multiple laser spots overlap. They result from microsegregation of Ti between dendritic grains during solidification, forming the Ti-rich Ti_2Ni phase as identified in Chapter 5. This phase is known

to have limited solubility of oxygen [12]. During pulsed laser processes oxygen pick up leads to the formation of Ti_2NiO_x even in Ni-rich alloy as shown in Chapter 5, since oxygen is not soluble in the NiTi matrix [12].

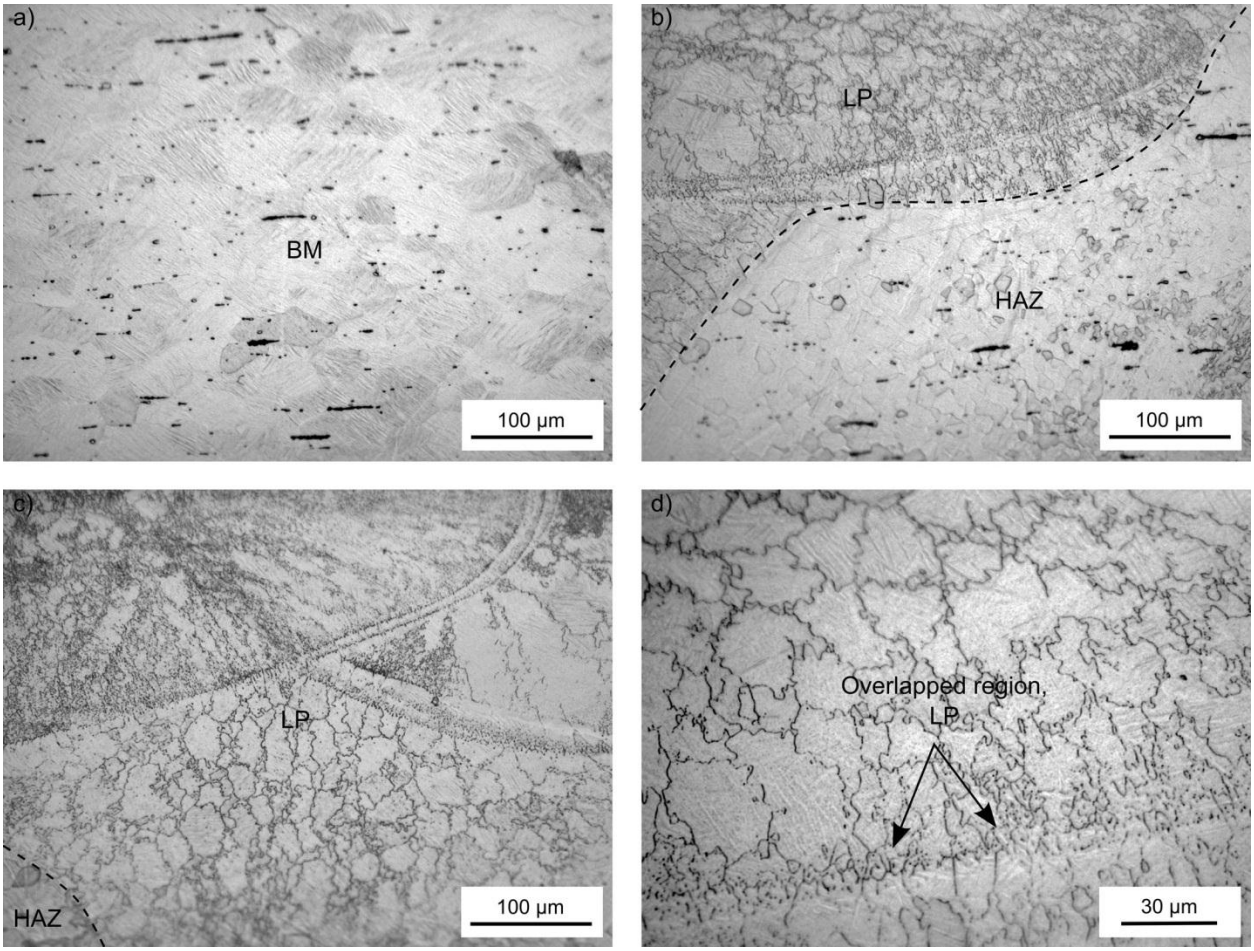

Figure 60: Microstructure of cross-sectioned samples. a) BM (i.e. CE), b) edge of LP region and HAZ, c) overlapped laser spots, and d) high magnification image of LP region.

6.1.3. Optical microscopy and surface profiling

Surface micrographs of the CE and LP samples are shown in Figure 61. Topographical maps are also provided in Figure 62 for each of the sample surface conditions. The CE sample appeared to be relatively rough and with many pits. In contrast, the dendritic solidification structure of the LP material was smoother at a microscopic scale; however there are large peaks and valleys between the overlapping laser spots. Although the smoothest surface observed was from the LP-Pol sample, slight surface relief was still observed in the optical micrograph shown in Figure 61 c); likely due to thermoelastic phase transformation following mechanical grinding and polishing. The surface roughness, Ra, was measured to be 1.63 µm, 2.43 µm and 0.01 µm for the CE, LP, and LP-Pol samples respectively (Figure 62).

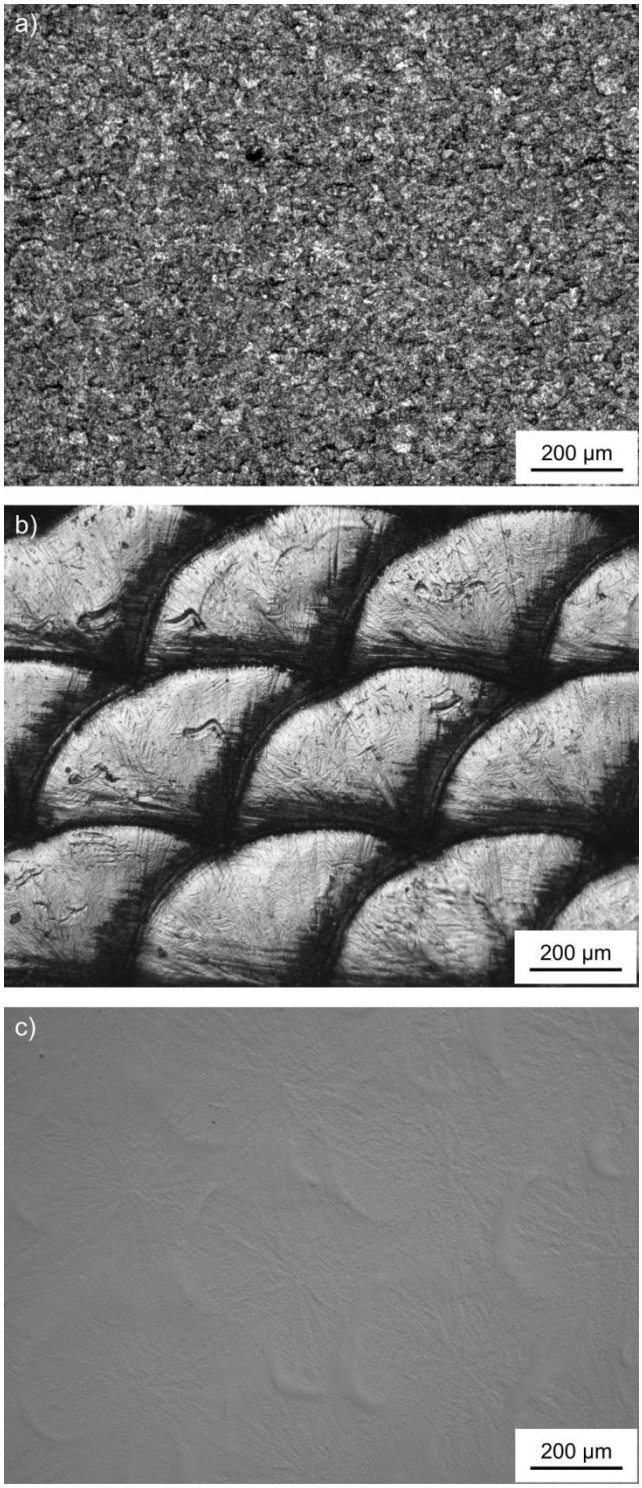

Figure 61: Optical micrographs of a) CE, b) LP and c) LP-Pol surfaces

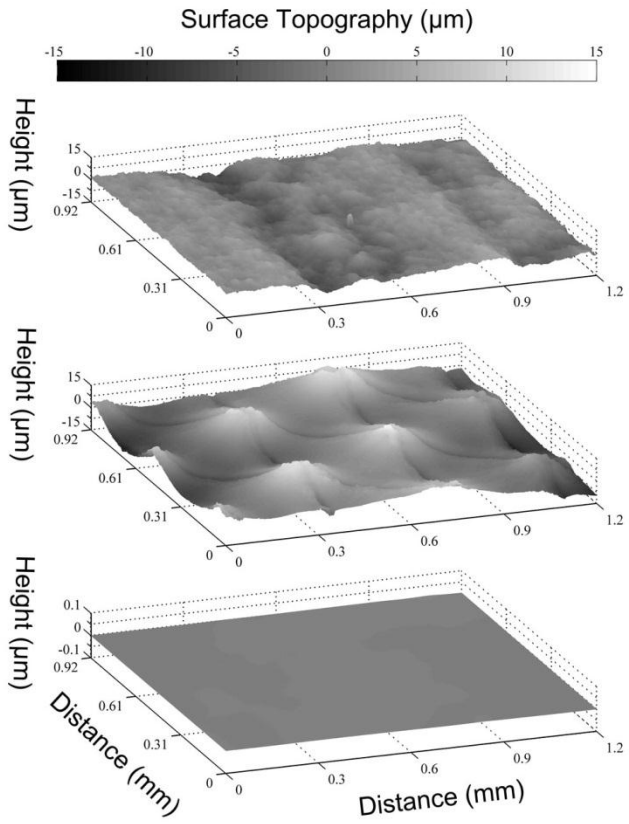

Figure 62: 3D topographical surface maps for a) CE (Ra = 1.63 µm), b) LP (Ra = 2.43 µm) and c) LP-Pol (Ra = 0.01 µm) samples. Special thanks to Andrew Michael and Jeff Wang for assisting with surface topography measurement.

6.1.4. Surface Chemistry and Depth Profile

A combination of XPS, AES, and Raman spectroscopy was implemented to identify the structure and chemistry of the different NiTi surfaces. First, XPS results for each of the samples are presented in Figure 63 to Figure 65. The identified species and their respective binding energies are summarized in Table 7 to aid in further discussion.

Table 7: Species identified via XPS analysis on the CE, LP and LP-Pol surfaces and their respective binding energies (eV)

	Peak Energy (eV)	Constituent	Present in Sample		
			CE	LP	LP-Pol
Ni	852.68	Ni $2p^{2/3}$	yes	yes	yes
	855.66	Ni_2O_3	no	yes	no
	859.51	sat. Ni $2p^{2/3}$	yes	yes	yes
Ti	454.85	Ti $2p^{2/3}$	yes	yes	yes
	458.76	TiO_2 $2p^{2/3}$	yes	yes	yes
	460.48	Ti $2p^{2/3}$	yes	yes	yes
	464.40	TiO_2 $2p^{2/3}$	yes	yes	yes
Oxygen	530.24	TiO_2	yes	yes	yes
	532.40	C=O, C-O, OH-Ti-OH	yes	yes	no
	533.76	H_2O-Ti-H_2O	no	no	yes
Carbon	285.17	C-C	yes	yes	yes
	286.63	C-O	yes	yes	yes
	288.32	C=O	yes	yes	yes

Figure 63 shows the XPS depth profile of the CE sample. Trace amounts of elemental Ni were observed on the surface with increased intensity at longer etch times. Titanium was primarily in the form of TiO_2 with a shift to metallic Ti as etch depth increased. Oxygen was mostly in the form of metallic oxide (TiO_2) with some carbon bonding or possible metallic hydroxides on the surface.

Surface XPS analysis of the LP sample, shown in Figure 64, also contained trace amounts of elemental Ni, however Ni_2O_3 was also identified. Although at a binding energy of 855.66 eV constituents other than Ni_2O_3 are possible, the known presence of a black plume deposited on the surface during laser processing [72] suggests that it was in fact Ni_2O_3. Furthermore, the intensity of elemental Ni increased with etch depth; however Ni_2O_3 was not detected below the surface. Titanium on the surface also formed an oxide in the form of TiO_2, which shifted to metallic Ti deeper into the sample surface. A relatively more gradual change from TiO_2 to metallic Ti is indicative of a thicker oxide layer. Oxygen was mostly in the form of metallic oxide (TiO_2) with some carbon bonding or possible metallic hydroxides on the surface, similar to the CE sample (Figure 63).

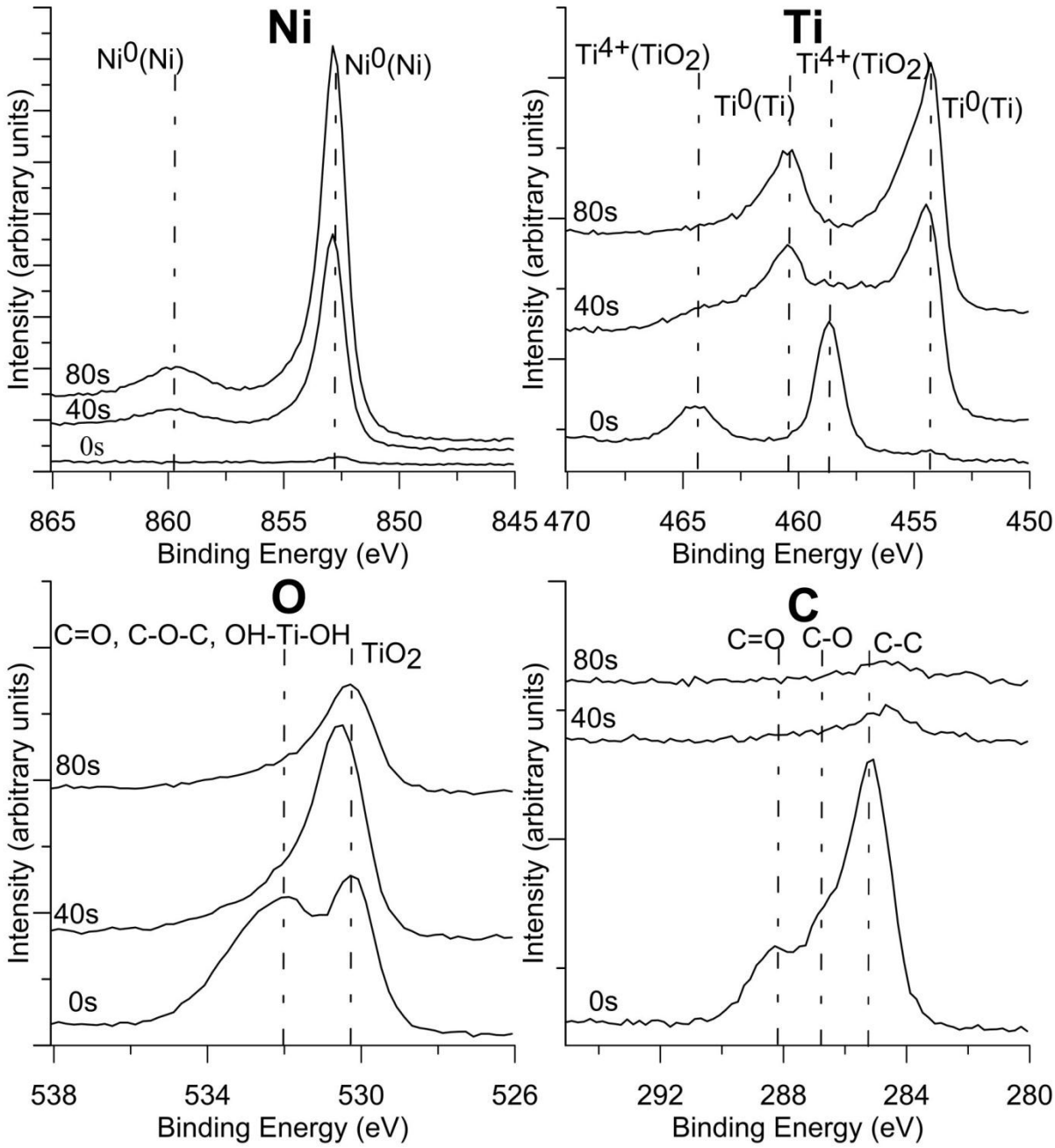

Figure 63: XPS depth profile of the CE sample at 0s, 60s and 80s etch times. Special thanks to Andrew Michael for assisting with XPS analysis.

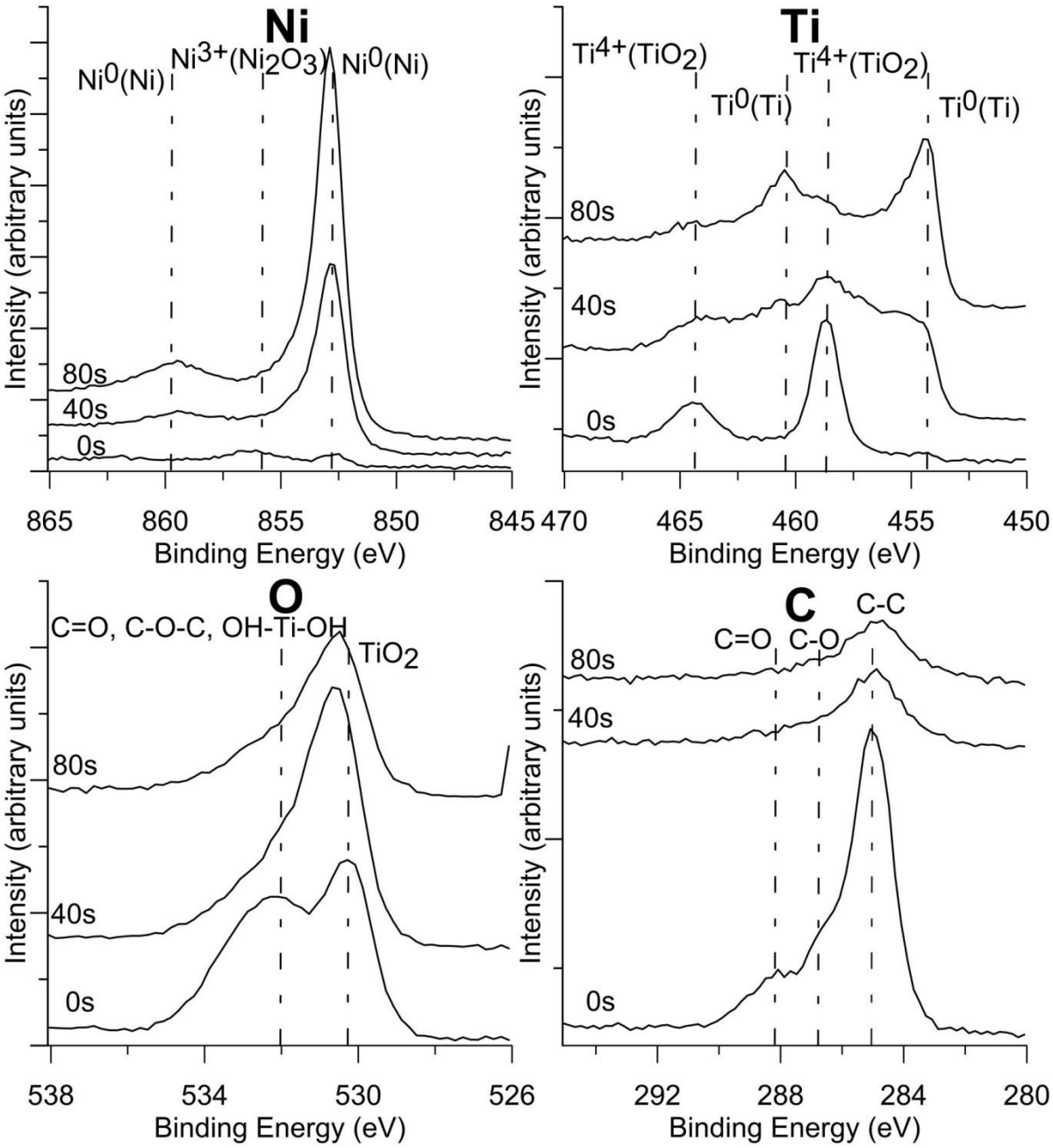

Figure 64: XPS depth profile of the LP sample at 0s, 60s and 80s etch times. Special thanks to Andrew Michael for assisting with XPS analysis

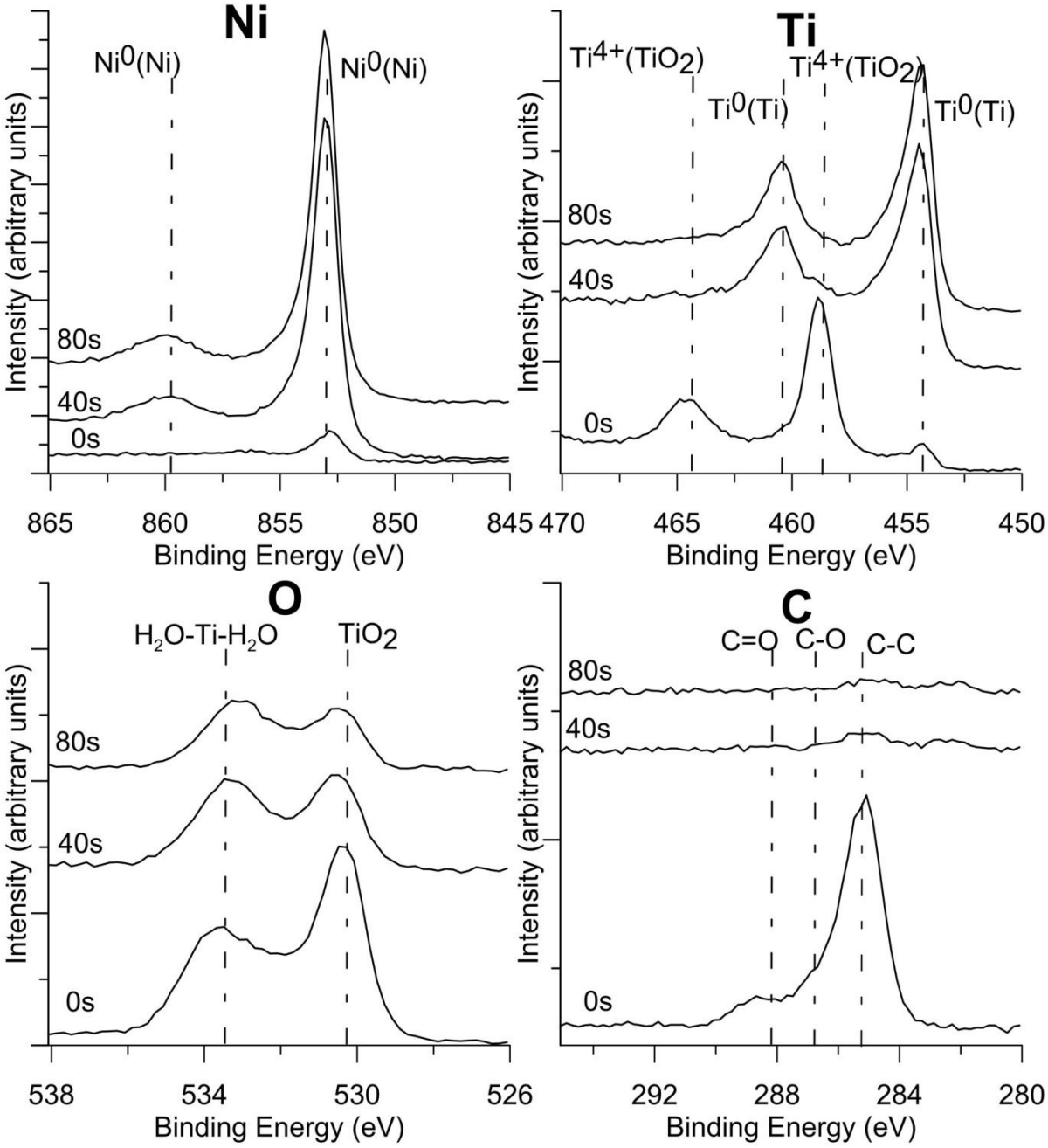

Figure 65: XPS depth profile of the LP-Pol sample at 0s, 60s and 80s etch times. Special thanks to Andrew Michael for assisting with XPS analysis

Analysis of the LP-Pol, shown in Figure 65, identified a greater amount of elemental Ti and Ni on the surface compared to the CE and LP samples. Titanium was primarily in the form of TiO_2 and shifted to metallic Ti as depth increased. A more rapid change from TiO_2 to metallic Ti was indicative of a thinner oxide layer compared to both the CE and LP samples. Oxygen was mostly in the form of metallic oxide

(TiO_2), however some hydrated Ti from polishing was observed; in agreement with previous studies investigating mechanically polished NiTi surfaces [119].

The AES depth profile of the C, O, Ni and Ti signals for all samples are shown in Figure 66. These graphs plot relative atomic concentration as a function of SiO_2 etch time. The oxide thickness for the CE and LP samples were 11.5 nm and 13.5 nm, respectively. In contrast, the oxide thickness for the LP-Pol sample was about half that of CE and LP samples, near 6 nm. No significant Ni enrichment of the surface interior was identified in any of the samples. Thick oxides must be present to begin to observe this Ni enriched layer [156]. The oxygen and carbon levels remain quite high in the extreme surface interior/bulk of the CE sample compared to that in the laser processed samples. This could be an artefact of higher contaminant levels (i.e. large TiC and Ti_2NiO_x inclusions) resulting from the material manufacturing process [79].

From the Raman spectrometry results given in Figure 67, the degree of crystallinity of the surface oxide was identified. It was observed that the CE and LP-Pol samples had an amorphous surface oxide by the absence of measured Raman bands. For the LP sample, an amorphous surface oxide was also identified within a laser spot (LP1 region, Figure 67 b)). However, adjacent to where the laser spots overlap, in an approximately 20 µm wide band (LP2 region, Figure 67 b)), some degree of crystallinity was observed. The low intensity, broad nature of the measured Raman bands in this LP2 region can result from the thin nature of the oxide layer and/or low degree of crystallinity respectively [157], making definitive crystal structure identification difficult. From past literature it has been shown that TiO_2 in either the Rutile and Anatase crystal structures and even $TiNiO_3$ have been identified on the surface of NiTi [157, 158]; each of which have Raman bands which may contribute to the trend identified in Figure 67.

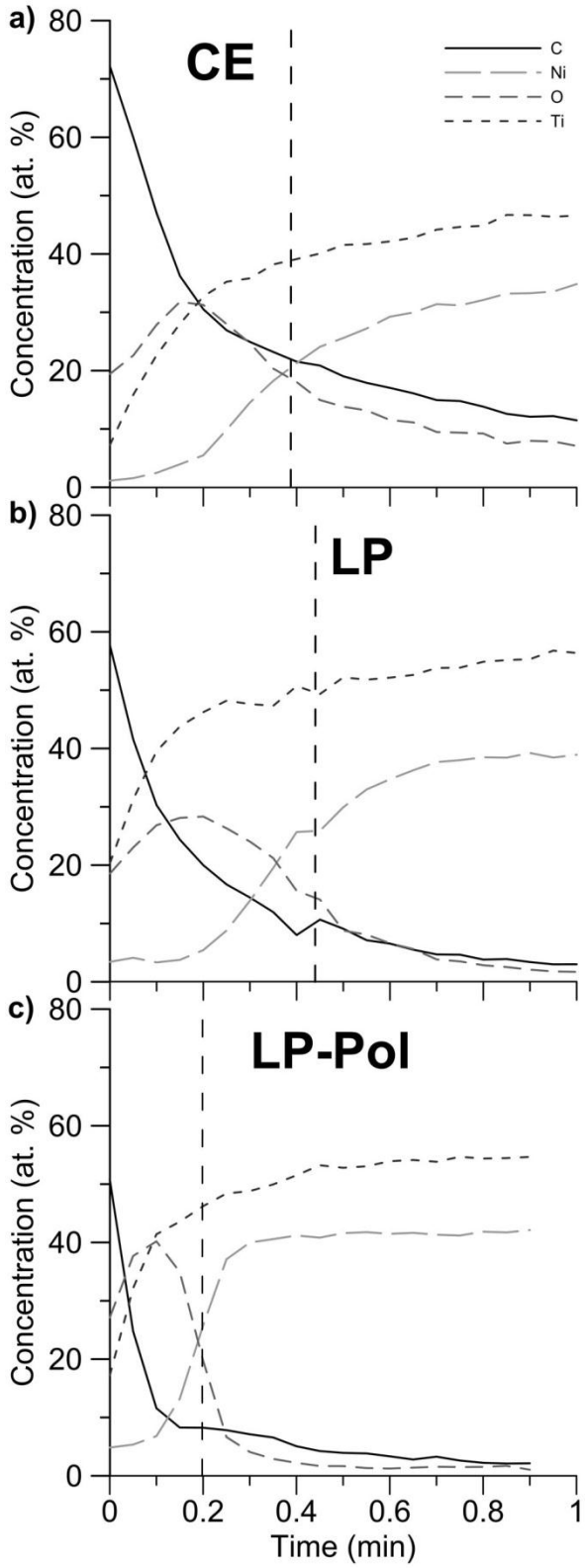

Figure 66: Auger depth profiles for a) CE, b) LP, and c) LP-Pol samples. The vertical dashed line corresponds to the approximated oxide thickness. Special thanks to Andrew Michael for assisting with AES analysis.

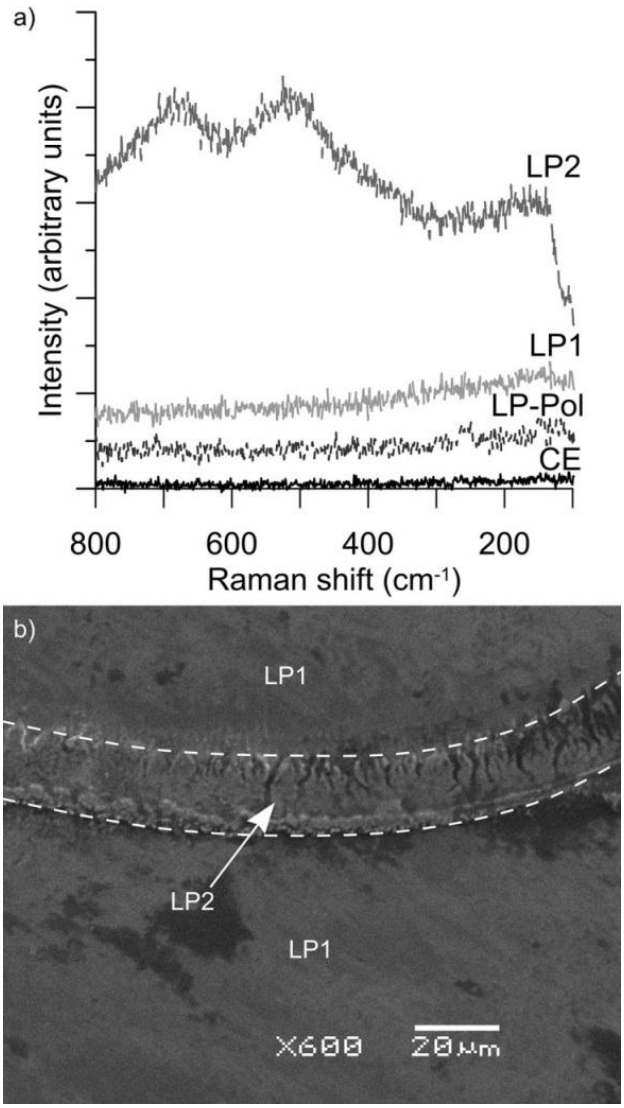

Figure 67: a) Raman spectra for 800 – 100 cm^{-1} wavenumber survey, and b) SEM image of the LP2 region where adjacent laser spots overlap (located between the dashed lines). Special thanks to Andrew Michael for assisting with Raman analysis.

6.1.5. Cyclic Potential Polarization and Ni ion release

Representative cyclic potential polarization curves for each of the samples are shown in Figure 68. Breakdown potential of the LP sample was lower than both the CE and LP-Pol sample, as it broke down and corroded at a significantly lower potential (i.e. ~550 mV). Each sample had a similar current density ranging between $7x10^{-7}$ and $7.5x10^{-7}$ A/cm^2 in the passive region of the curve, indicating similar rates of metal dissolution. Spikes in the current density were observed in the CE curve, which likely correspond to rapid pitting and re-passivation. The equilibrium corrosion potentials were found to vary by > 100 mV for all tests.

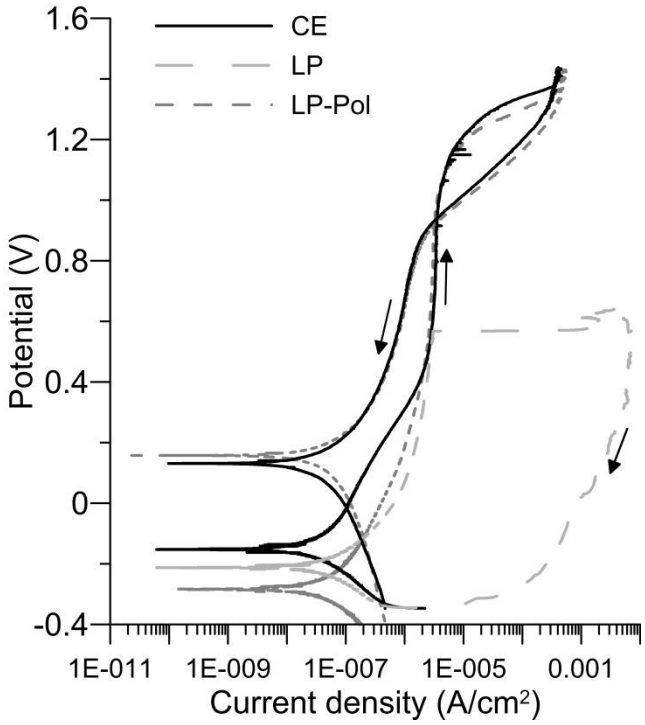

Figure 68: Representative potentiodynamic cyclic polarization curves for CE, LP and LP-Pol samples. Special thanks to Andrew Michael and Jeff Wang for assisting with electrochemical corrosion testing.

Scanning electron micrographs of the NiTi surface following the potentiodynamic cyclic polarization tests are provided in Figure 69. The CE and LP-Pol samples showed uniform pitting across the surface; shown in Figure 69 a) and c). Pit defects observed in the LP-Pol sample were much smaller compared to the CE sample. In the LP sample, only few areas exhibited extensive localized corrosion, as shown in Figure 69 b). It was noted that localized corrosion in the LP samples was preferential where the laser spots overlap each other, as illustrated by the dashed lines in Figure 69 b). Therefore corrosion originated in the LP2 region adjacent to each pulse (Figure 67 b)).

Aside from the corrosion performance, the amounts of Ni ions released into the PBS solution after 7 days for the CE and LP-Pol samples were below the detection limit of 13.2 µg/L (13.2 ppb). However, Ni ion release for the LP samples was 12.3 µg/L, after subtracting the Ni concentration measured in the control.

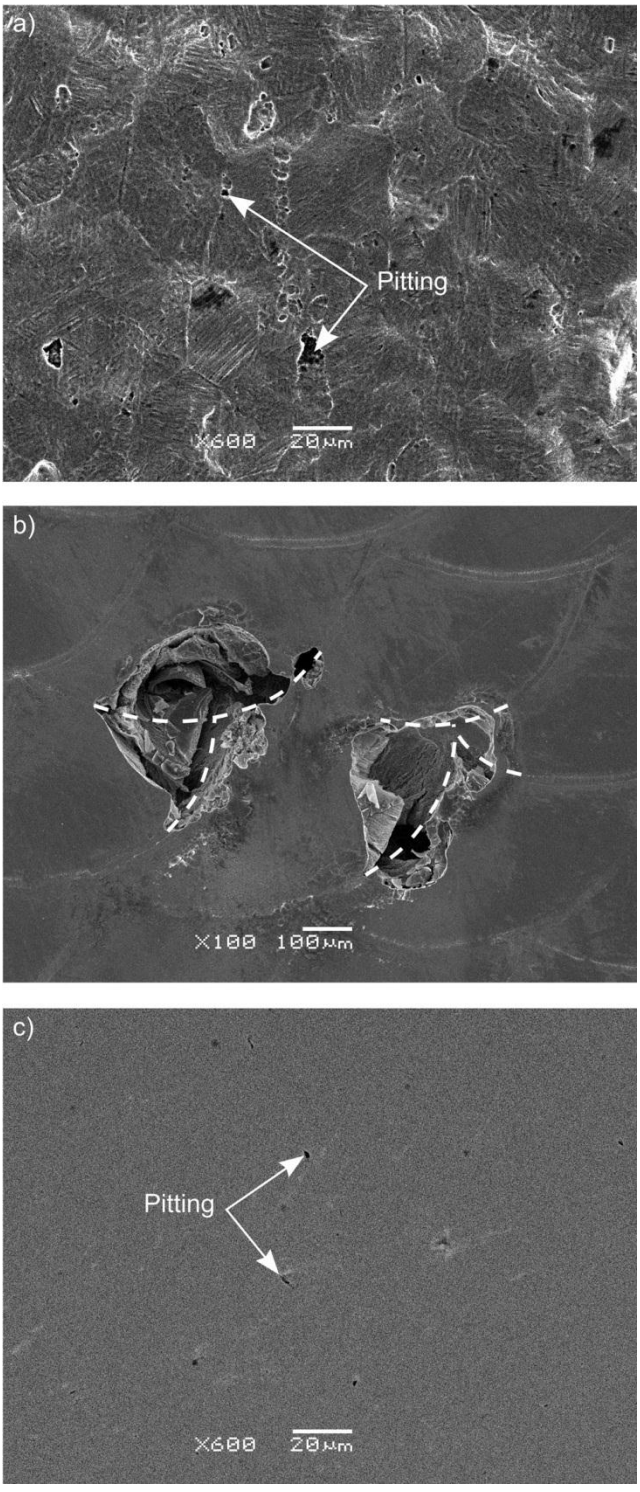

Figure 69: SEM images of corroded surfaces: a) CE; b) LP; and c) LP-Pol

6.2. Discussion

6.2.1. Effects of Laser Processing on Surface Characteristics

The corrosion performance and biocompatibility of NiTi SMAs are strongly linked to factors such as chemical composition, oxide thickness, surface chemistry, and roughness [69, 77, 80, 81, 122, 159]. It is therefore necessary to further discuss the effects of laser processing on these material characteristics.

Chemical composition plays a particularly important role in the formation of chemical species on a materials surface, where amorphous TiO_2 is preferred over mixtures of Ni- and Ti-oxides and the presence of elemental Ni is undesirable all together [119-121]. Following laser processing the bulk material composition drastically changes. Moreover, in the current work laser processing parameters were selected to induce preferential vaporization of Ni, leaving a Ni depleted region in the bulk material. Although this change in composition was small, evidence of preferential vaporisation can be observed in the DSC results shown in Figure 59, where the Ni depleted LP material exhibited higher phase transformation temperatures. Specifically, the 86.5°C increase in the M_s transformation temperature (Table 6) can be used to estimate the change in local bulk chemical composition using the thermodynamic models shown in Figure 14 [12, 48]. A decrease in the Ni composition of 0.48 at.% was predicted using Tang's model (i.e. 180 ° change / at.% Ni) [48] and an even larger decrease of 1.04 at.% Ni was predicted using the more recent model presented by Frenzel et al. [12] (i.e. 83 ° change / at.% Ni). An increase in bulk material Ti/Ni ratio following laser processing was suggested by Man et al. [80] to be one of the mechanisms behind improved corrosion performance of laser surface melted NiTi SMAs. A higher bulk Ti/Ni ratio was implied to correlate with an improvement of Ti/Ni ratio at the material surface, leading to the formation of a more robust TiO_2 oxide. To investigate this mechanism further and for better comparison with literature [160], the Ti/Ni ratios measured via AES analysis were plotted as a function of depth in Figure 70. Higher Ti/Ni ratios observed in the CE and LP samples reflect Ni depletion that occurs during the chemical etching and laser processing procedures respectively [130, 161]. The LP and CE samples had similar Ti/Ni ratios on the surface, however the LP sample did in fact show a slightly higher maximum ratio and the ratio remained higher to a greater depth. This suggests that more Ni was removed from the surface during laser processing compared to chemical etching and correlates well with greater oxide thickness identified on the LP sample (Figure 66). The LP-Pol sample however, had a much lower Ti/Ni ratio and reached bulk concentrations sooner than both the CE and LP samples.

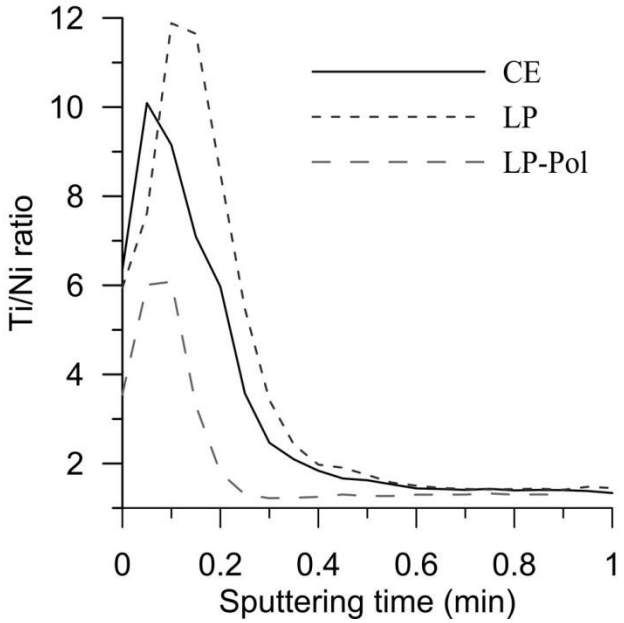

Figure 70: Ti/Ni ratio depth profiles measured via AES analysis for the CE, LP and LP-Pol samples

Now with a better understanding of the composition of the bulk material and the subsurface layers, it is essential to discuss the oxide species that form on each respective substrate as well as other importance surface characteristics, such as surface roughness and degree of crystallinity of oxides. In this study, the CE sample was selected as the baseline since chemical etching was already a necessary step to remove the thick black oxide prior to NiTi medical device deployment, to clean the surface and build TiO_2 while leaching out Ni [130, 161]. Furthermore this black oxide has also been shown to cause embrittlement of the laser processed region [74]. After etching, the CE samples had a rough pitted appearance with a roughness value, Ra of 1.63 µm (Figure 61 and Figure 62). The surface chemistry of the CE sample was similar to that found in literature [130] where amorphous TiO_2 oxide was found to preferentially form with only trace amounts of elemental Ni present (Figure 63 and Figure 67).

In contrast to the CE samples, the LP samples were subjected to several high power density laser pulses. However, aside from the presence of Ni_2O_3, surface chemistry was similar to the CE sample (Figure 63 and Figure 64). Since Ni_2O_3 was no longer detectable after a 20s sputter during XPS analysis it was only present on the top most surface layer and was presumed to result from condensation of Ni-rich plume during laser processing [72]. The LP sample oxide was formed on top of the re-solidified material and subjected to several heating cycles as adjacent laser spots were made. These subsequent thermal cycles can contribute to thickening the oxide. The LP material exhibited only a slightly thicker oxide layer (13.5 nm) than the CE specimen (11.5 nm). The Ar shielding used in the laser process prevented excessive

oxide growth by limiting the oxygen available for reaction. Thermal cycles experienced during processing in the LP samples however, may have resulted in the ~20 µm wide LP2 region, having a higher degree of crystallization, adjacent to each laser spot as shown in Figure 67.

The LP-Pol sample showed higher amounts of elemental Ti and Ni on the surface compared to the LP and CE samples (Figure 65). The increase in elemental Ti was due to only partial oxidation of Ti in air at room temperature [119]. Partial oxidation also contributed to the lowest Ti/Ni ratio, shown in Figure 13, while forming the thinnest oxide layer of 6 nm. This higher elemental Ni concentration can be attributed to mechanical polishing procedure not selectively removing Ni, while acid etching and laser processing do so through leaching [130, 161] and vaporization (Chapter 5) mechanisms respectively. Mechanical polishing did however, decrease the surface roughness to Ra = 0.01 µm from a Ra value of 2.43 µm (Figure 62) and facilitated the formation of a favourable uniform, amorphous oxide on the surface (Figure 67).

6.2.2. Corrosion and Ni Ion Release Performance

It has previously been shown that chemical etching produces a surface that is highly resistant to both general and pitting corrosion [161, 162]. The CE sample tested in this study showed the best corrosion resistance through cyclic polarization testing. When considering only the increase in Ti/Ni ratio and oxide thickness, the LP sample could be expected to have similar performance as the CE sample. Moreover, according to literature, laser surface melting can improve corrosion performance [80, 81]. However, the LP samples exhibited a breakdown potential of about half that of the CE and LP-Pol samples (~ 500 mV) as well as exhibiting the highest Ni ion release of 12.3 µg/L.

There are several factors that contribute to the decreased breakdown potential and increase in Ni ions released from the LP sample. The re-melted surface of the laser spot was relatively smooth compared to the roughness values of the CE material, which has been suggested in several studies [77, 79-81] to contribute to an improve corrosion behaviour of laser processed NiTi; discussed in section 2.7.1. However, micro-crevices also formed at the intercept of four laser spots (Figure 62) along with a region of higher crystallinity adjacent to each laser spot (Figure 67). This topography lead to the highest overall roughness measured of all three samples. Since localized corrosion was observed to occur where the laser spots intercept (Figure 69 b)), micro-crevices and partially crystalline oxide in the LP2 region were concluded to play a critical role in degrading corrosion performance. Another possible contribution to decrease corrosion resistance and increased Ni ions released was the presence of Ni_2O_3 on the top surface of the LP samples. Previous studies have shown that a homogeneous oxide is more stable than a

heterogeneous oxide [119]. A mixture of oxides can lead to a segregation of species that leaves the oxide layer more susceptible to corrosion. In addition, an amorphous oxide layer is also more stable and corrosion resistant [119].

As mentioned above, a higher Ti/Ni ratio suggests the formation of a more robust protective oxide layer however, in the bulk material this can also lead to the formation of secondary phases between dendrites due to microsegregation. In laser surface melting Man et al. [80] and Cui et al. [81] both imply Ni constituent loss due to vaporization and they identified the Ti_2Ni, Ti-rich phase using X-ray diffraction in the laser melted region. Secondary phases, Ti_2Ni and Ti_2NiO_x were also identified at prior parent grain boundaries due to microsegregation and oxygen pick-up in Chapter 5. The secondary phases identified in the LP cross-sectioned sample (Figure 60) were therefore, also Ti_2Ni or Ti_2NiO_x. The presence of inclusions on the surface of NiTi also affects the homogeneity/uniformity and therefore stability of the oxide layer [120]. In addition, Ni-rich regions form around Ti-rich phases leading to the presence of elemental Ni and increased Ni ion release [120].

After mechanical polishing, the LP-Pol sample had comparable corrosion resistance as the CE sample. Similar results were also observed from the Ni ion release test where both the CE and LP-Pol samples produced no detectable amount of Ni ions after a 7 day immersion in PBS solution. Mechanical polishing of the laser processed material removes any undesirable surface topography, crystallized oxides, and Ni_2O_3 species. The thin amorphous oxide with lower Ti/Ni ratio (Figure 66 and Figure 70) was found to have improved corrosion and Ni ion release performance. These results suggest that changes to the bulk material from laser processing such as, increased Ti/Ni ratio and the formation of Ti_2Ni and Ti_2NiO_x phases at dendritic grain boundaries did not significantly affect the corrosion resistance of the bulk material. The change in corrosion resistance observed in the LP material comes from one or more characteristics present on the top-most surface which can be removed via post-processing procedures such as mechanical polishing.

6.2.3. Laser processed NiTi as a Biomaterial

Just as in other NiTi processing techniques, the corrosion and biocompatibility of laser processed NiTi surfaces can vary depending on many factors as discussed in section 2.7. The current study showed, contrary to other laser processing studies examining laser surface melting [80, 81] or laser welding [76-78, 126], that the corrosion performance and Ni ion release levels were not improve immediately after processing; in line with the findings of Chan et al. [75].

Even though a decrease in breakdown potential was observed in the current study, the magnitude was still on par with stainless steel [118] and the metal dissolution rate remained unchanged in the passive region. Moreover, based on the number of days tested and volume of PBS solution used in the Ni ion release test, the average Ni ion release rate of as-laser processed material (LP) was negligible compared to the daily dietary intake of 300 -500 µg/day [163], the critical concentration for allergic response of 600 – 2500 µg/day [164], and the in vitro cytotoxicity limit of 30 ppm [165]. So taken in context, although the corrosion and ion release performance of the LP sample was lower compared to the other sample conditions analysed in this study, the performance in general was still good. For example in less demanding medical applications such as minimally invasive surgical tools, which have relatively short service lives and limited exposure to patients, the performance of as-laser processed materials could be acceptable. Moreover, it was shown that for more demanding biocompatibility applications such as, implantable medical devices, laser processed NiTi SMAs can also be used as long as the effects of processing on the surface characteristics are well understood and if necessary, an appropriate post-laser-process surface treatment is utilized.

6.3. Chapter summary

In this chapter the surface of laser processed NiTi material was characterized through comprehensive spectrographic analysis and roughness measurement. Past theories regarding the corrosion and Ni ion release properties of laser processed NiTi, presented in section 2.7.1. were tested. It was identified that detrimental surface characteristics such as increased roughness, crystallinity, and presence of volatile oxide species, overshadowed any possible performance improvements from a decreased Ni:Ti ratio or inclusion dissolution.

Laser processed samples were shown to have acceptable corrosion and ion release performance having breakdown potentials comparable to stainless steel and Ni ion release levels below biologically harmful levels. Post-laser process mechanical polishing (i.e. LP-Pol sample) was found to improve corrosion performance comparable to that of the CE control sample. Therefore, confidence in applying laser processing protocol to medical device applications was restored. With a solid understanding of the surface conditions of the laser processed material and if necessary application of an appropriate post-process surface treatment excellent corrosion and Ni ion release properties can be achieved.

7 Conclusions and future outlook

In the current thesis work pulsed Nd:YAG processing of binary, near equiatomic NiTi SMAs was explored. More specifically, several novel laser processing protocols for increasing functionality, the dynamic actuation and control, the process–structure–performance relationship, and the corrosion and Ni ion release of laser processed NiTi SMAs were investigated. Identification of critical post-processing techniques for improving performance and functionality were also addressed. Fundamental understanding of novel laser processing and post-laser processing techniques, as well as in the design and control of laser processed components was achieved through this work.

The following sections contain the major conclusions from this work and detail recommendations for future research direction.

7.1. Conclusions

7.1.1. Dynamic actuation and control of a novel laser-processed NiTi linear actuator

In this work a state-of-the-art laser processing technology was demonstrated to improve the functionality of a NiTi wire linear actuator for the first time. The addition of a second memory allowed for two distinct actuations using controlled resistive heating. The performance of this novel linear actuator was characterized and a better understanding of the results has been obtained. The main findings were as follows:

1. Laser processing enabled the modification of thermomechanical properties in a monolithic NiTi SMA. Compared to the as-received material, the transformation temperatures were increased after laser processing allowing for the development of a two memory linear actuator.
2. Dynamic actuation was achieved using resistive heating and the simplicity of the DC control method was demonstrated. Dynamic activation of SMAs via a passive control method is now possible substantially broadening possible NiTi SMA applications.
3. Tensile tests identified significant differences in the stress-strain behaviour during the deformation of martensite in the as-received and laser processed materials. Lüders-like deformation did not occur in the laser processed material. Instead, strain-hardening took place during the reorientation of martensite. Also, the σ_M was found to be substantially higher for the laser processed material due to higher phase transformation temperatures and the inherent temperature dependence of martensite stability.

4. The interaction between the two different regions of the linear actuator was identified during each stage of actuation. The substantially lower σ_M of the as-received material led to a much larger active strain in the as-received region. Following activation of the as-received region, the stress and temperature in the laser processed region changed with increasing pre-strain, complicating the determination of total active strain. New design considerations for laser processed NiTi SMAs were therefore identified.
5. From cyclic actuation testing ε_p was found to stabilize after approximately 150 cycles while ε_r remained almost constant over all 200 cycles demonstrating expected NiTi SMA low cycle behaviour.

7.1.2. Tuneable NiTi shape memory alloy functional properties through combined laser processing, cold work and heat treatment

Utilizing a novel combination of laser induced vaporization, cold working and heat treatment, increased functionality and unique performance offerings of monolithic NiTi SMA components were demonstrated. In this study the composition, microstructure, and performance of processed binary NiTi alloys were characterized allowing for the realization of critical relationships between the processing protocol and resulting microstructure and material performance. The most significant findings of this study include:

1. Using a pulsed vaporization based laser processing protocol the composition, microstructure and therefore functional properties can be locally tailored. A linear relationship between Ni:Ti ratio and the number of laser pulses per spot parameter (- 0.16 at. % Ni/laser pulse) was realized. The change in composition correlated well with changes in phase transformation temperatures, proving the previously proposed relationship between elemental Ni content and M_s temperature for binary NiTi SMAs. The precise nature of laser induced vaporization therefore allowed for embedding a tuneable local gradient of composition and microstructure in NiTi components.
2. The SME of NiTi SMAs in the as-laser processed condition was found to be possible due to the martensite detwinning stress being lower than the yield stress. Also, maximum strains at failure were found to be greater than 10 % allowing for full range of SME in polycrystalline NiTi SMAs.
3. Post-laser processing cold rolling (i.e. 27 % thickness reduction) followed by a 673 K (400 °C) for 3.6 ks anneal restored the PE property of laser processed material through increasing yield strength. Ni-rich Ni_4Ti_3 precipitates however, were not identified using this combined laser processing, cold rolling and heat treatment processing protocol.

4. Two unique and highly desirable performance offerings were identified using the novel combination of laser processing, cold work and heat treatment. The first unique property demonstrated was synergistic response of adjacent SME and PE regions and the second was the addition of multiple PE stress plateaus. Having both SME and PE in a monolithic NiTi SMA component allows for a 'self-biasing' mechanism where the PE region stores the energy created during SME allowing for cyclic actuation. This 'self-biasing' effect enables new actuation applications to be realized, especially in small scale micro-actuation. Multiple PE components are also immediately applicable to current medical device technologies such as guide wires, catheters, stents and orthodontic arch wires.

7.1.3. Effects of laser processing on surface characteristics of NiTi shape memory alloys

The current study systematically investigated the corrosion performance and Ni ion release performance of a laser processed NiTi. Surface conditions, including, chemistry, oxide thickness, composition, microstructure, and roughness were thoroughly characterized. The most significant findings of this study included:

1. Laser processing removed large TiC, Ti_2Ni, and Ti_2NiO_x inclusions present in the base material. Fine Ti_2Ni and Ti_2NiO_x secondary phases were however identified at dendritic grain boundaries in the solidification structure. As observed through the excellent resistance to pitting corrosion and non-detectible amounts of Ni ions released from the LP-Pol samples, these secondary phases were however not found to significantly affect the corrosion performance.
2. Superficial surface conditions such as large peaks and valleys between laser pulses, the presence of a crystalline oxide region adjacent to each laser spot, and Ni_2O_3 oxide resulting from plume deposited on the surface led to local breakdown of the LP samples and higher cumulative amount of Ni ions released. Following mechanical polishing of the LP material the corrosion performance and Ni ion release performance was therefore found to be restored.
3. A decrease in bulk material Ni composition on the order of 0.48 – 1.04 at. % following laser processing had insignificant effects on corrosion performance and Ni ion release compared to surface characteristics induced by the pulsed laser process.
4. The corrosion resistance and amount of Ni ions released from pulsed Nd:YAG laser processed NiTi SMAs remained acceptable. However, with appropriate post processing treatments such as mechanical polishing the performance can be greatly improved, allowing for their utilization in a wider range of medical applications.

7.1. Future outlook

1. Low cycle performance of as-laser processed wire was shown to behave as expected with ε_r remaining constant over 200 cycles and ε_p became stable after just 150 cycles in Chapter 4. However, the fatigue performance of such laser processed material has yet to be determined. If such laser processed components are going to be applied their service life must be considered. For example, a surgical tool for minimally invasive surgery may be used < 100 times before it is discarded however, implantable arterial stents must survive up to 10^8 low strain loading cycles induced by the beating heart [166]. From the current results, the as-laser processed material could be used for low cycle life devices however, systematic SME and PE fatigue testing must be undertaken before they can be applied to high cycle applications with confidence.
2. The post-processing techniques applied in Chapter 5 restored PE through increasing yield stress however, this protocol was not optimized. More research into the optimization of the combined laser, cold work, and heat treatment processes is necessary to achieve the greatest possible increase in performance and functionality. Specific areas for improvement may include: i) selecting heat treatment parameters that produce Ni_4Ti_3 precipitates since these precipitates have been cited as the most effective way to improve structural and functional properties [57] and ii) investigation into the evolution of texture during each processing step since crystal texture plays a critical role in deformation behaviour [38, 57, 135, 137].
3. More complex ternary NiTi alloys offer performance benefits such as the reduced hysteresis offered by NiTiCu which is currently used in many orthodontic applications such as for arch wires or higher transformation temperatures offered by NiTiPd or NiTiZr alloys [167-170]. The laser induced vaporization protocol is based on the vapor pressure of the different elements in the molten pool as detailed in section 2.6. The flux of the different elements leaving the molten pool will therefore determine the final properties of the ternary NiTi alloy. Research into this area could yield some very interesting performance offerings that have not yet been realized.
4. Numerical modeling of the vaporization process in NiTi alloys based on the work of He et al. [100, 101] and Jandaghi et al. [102] would be a huge asset when seeking to apply laser induced vaporization to real life SMA applications. Using the composition measurement such as the results obtained in Chapter 6, a model could be created to predict the effects of different laser parameters on the change in Ni:Ti ratio, theoretically enabling the selection of combinations of subsequent laser pulses to achieve any desired phase transformation temperature.

5. Understanding of the effects of laser processing on corrosion performance has been greatly improved with the discovery that superficial surface defects dictate the corrosion and Ni ion release behaviour in Chapter 6. With this knowledge other post-processing treatments that remove these superficial defects such as chemically etching or combinations of chemical etch and water boiling or autoclaving also have great potential to improve performance and should be considered. Moreover, since NiTiCu ternary alloys are heavily used in the orthodontic industry the effects of laser processing on the corrosion performance and ion release of these ternary alloys should also be addressed.

8 Contributions to research and development

8.1. Articles published in refereed journals

1. Khan, M.I., **Pequegnat, A.**, Zhou, Y.N. (2013) Multiple Memory Shape Memory Alloys. *Advanced Engineering Materials*. **15**(5):386-393 (PhD work).
2. **Pequegnat, A.**, Huang, Y.D., Khan, M.I., Zhou, Y. (2012) Effects of electrolyte on hardening in laser hole sealing of commercially pure grade 1 titanium. *Journal of Materials Processing Technology*. **212**(10):2012-2019 (PhD work).
3. Huang, Y.D., **Pequegnat, A.**, Khan, M.I., Zhou, Y. (2012) Laser hole sealing of commercially pure grade 1 Titanium. *Journal of Laser Applications*. **24**: 032010 (PhD work).
4. Daly, M., **Pequegnat, A.**, Zhou, Y., Khan, M.I. (2013) Fabrication of a novel laser processed NiTi shape memory microgripper with enhanced thermomechanical functionality. *Journal of Intelligent Materials Systems and Structures*. **24**(8):984-990 (PhD work).
5. **Pequegnat, A.**, Daly, M., Wang, J., Zhou, Y., Khan, M.I. (2012) Dynamic actuation of a novel laser processed NiTi linear actuator. *Smart Materials and Structures*. **21**(9):094004 (PhD work).
6. Daly, M., **Pequegnat, A.**, Zhou, N., Khan, M.I. (2011) Enhanced thermomechanical functionality of a laser processed hybrid NiTi-NiTiCu shape memory alloy. *Smart Materials and Structures*. **21**(4): 045018 (PhD work).
7. Tam, B., **Pequegnat, A.**, Khan, M.I., Zhou, (2012) Y. Resistance micro-welding of Ti-55.8 wt. % Ni Nitinol wires and the effects of pseudoelasticity. *Metallurgical Materials Transaction A*. **43**(8): 2969-2978 (PhD work).
8. Huang, Y. D., **Pequegnat, A.**, Zou, G. S., Feng, J. C., Khan, M. I., Zhou, Y. (2012) Crossed-wire laser microwelding of Pt-10% Ir to 316 LVM stainless steel Part II: Effect of orientation on joining mechanism. *Metallurgical Materials Transactions A*. **43**(4): 1234-1243 (PhD work).
9. Zou, G. S., Huang, Y. D., **Pequegnat, A.**, Li, X. G., Khan, M. I., Zhou, Y. (2012) Crossed-wire laser microwelding of Pt-10% Ir to 316 LVM stainless steel Part I: Mechanism of joint formation. *Metallurgical Materials Transactions A*. **43**(4): 1223-1233 (PhD work).
10. Huang, Y.D., **Pequegnat, A.**, Feng, J.C., Khan, M.I., Zhou, Y. (2011) Resistance microwelding of crossed Pt-10Ir and 316 LVM stainless steel wires. *Science and Technology of Welding & Joining*. **16**(7): 648-656 (PhD work).

11. **Pequegnat, A.**, Kim, H. J., Mayer, M., Zhou, Y., Persic, J., Moon, J. T. (2011) Effect of gas type and flow rate on Cu free air ball formation in thermosonic wire bonding. *Microelectronics Reliability*. **51**: 43-52 (Master's work).
12. Song, W. H., Hang, C., **Pequegnat, A.**, Mayer, M., Zhou, N. Y., Song, Y. K., Persic, J. (2009) Comparison of insulated with bare Au bonding wire: HAZ length, HAZ breaking force, and FAB deformability. *Journal of Electronic Materials*. **38**(4): 834-842 (Master's work).
13. **Pequegnat, A.**, Hang, C. J., Mayer, M., Zhou, Y., Moon, J. T., Persic, J. (2009) Effect of EFO parameters on Cu FAB hardness and work hardening in thermosonic wire bonding. *Journal of Materials Science: Electronic Materials* **20**: 1144-1149 (Master's work).
14. Huang, H., **Pequegnat, A.**, Chang, B. H., Mayer, M., Du, D., Zhou, Y. (2009) Influence of superimposed ultrasound on deformability of Cu. *Journal of Applied Physics* **106**: 113514-1 to 112514-6 (Master's work).

8.2. Articles in-press

1. Panton, B., **Pequegnat, A.**, Zhou, Y. Dissimilar Laser Joining of NiTi SMA and MP35N wires. Submitted to *Metallurgical and Materials Transactions A,* Aug. 15, 2013: Manuscript No. E-TP-13-1142-AR (PhD work).

8.3. Conference papers and presentations

1. **(Keynote)** Zhou, Y., **Pequegnat, A.**, Khan, M.I. Recent Advances in Laser Welding of Nitinol Shape Memory Alloys. *ASM International Conference on Shape Memory and Superelastic Technologies (SMST 2014), Pacific Grove, California, USA, May 12-16th.*
2. **(Invited) Pequegnat, A.**, Gerlich, A.P., Biro, E. (2013) Canadian trends in welding and joining technology. *Canadian Welding Bureau (CWB), CanWeld 2013 conference, Niagara Falls, Ontario, Canada, Oct. 28-29th* (PhD work).
3. **Pequegnat, A.**, Huang, Y.D., Khan, M.I., Feng, J.C., Zhou, Y. (2012) Laser hole sealing of CP titanium for medical device applications. *First International Nano- & Micro-joining Conference, Beijing, China, Dec. 4-6th* (PhD work).
4. **Pequegnat, A.**, Zhou, Y. (2012) Effects of welding on NiTi shape memory alloy functional properties. *International Institute of Welding (IIW) 2012 conference, SC-MICRO: select committee on research developments and applications in micro- and nano-joining technologies, Denver, Colorado, July 8-13th* (PhD work).

5. **Pequegnat, A.**, Vlascov, M., Daly, M., Zhou, Y., Khan, M.I. (2011) Dynamic actuation of a multiple memory material processed Nitinol linear actuator. Proc. of the *ASME 2011 Conference on Smart Materials, Adaptive Structures and Intelligent Systems*, *Phoenix, Arizona*: 4994 (PhD work).
6. Daly, M., **Pequegnat, A.**, Zhou, N., Khan, M.I. (2011) Fabrication of a novel monolithic NiTi based shape memory microgripper via multiple memory material processing. Proc. of the *ASME 2011 Conference on Smart Materials, Adaptive Structures and Intelligent Systems, Phoenix, Arizona*: 4903 (PhD work).
7. **Pequegnat, A.**, Mayer, M., Persic, J., and Zhou, Y. (2009) Accelerated characterization of bonding wire materials. Proc. of *International Microelectronics and Packaging Society (IMAPS) 42nd International Symposium on Microelectronics*, San Jose, CA, U.S.A.: 367-373 (Master's work).

8.4. Book chapters

1. **Pequegnat, A.**, Zhou, Y. (2013) Crossed wire bonding of Pt to stainless steels. Published in: *Joining and Assembly of Medical Materials and Devices* (Eds. Zhou, Y., Breyen, M.), Woodhead Publishing, Cambridge, UK.

References

1. Buehler, W.J., Gilfrich, J.W., Wiley, R.C. (1963) Effect of low-temperature phase changes on the mechanical properties of alloys near composition TiNi. **34**(5):1475-1477.

2. Chang, L.C., Read, T.A. (1952) Plastic deformation and diffusionless phase changes in metals - The Gold-Cadmium beta phase. **191**:147-152.

3. Burkart, M.W., Read, T.A. (1953) Diffusionless phase change in the Indium-Thallium system. **197**:1516-1524.

4. Otsuka, K., Ren, X. (2005) Physical metallurgy of Ti-Ni-based shape memory alloys. *Progress in Materials Science*. **50**:511-678.

5. Jani J.M., Leary M., Subic A., Gibson M.A. (2014) A review of shape memory alloy research, applications and opportunities. *Materials and Design* **56**:1078-1113.

6. Duerig, T.W., Melton, K.N., Stockel, D., Wayman, C.M. *Engineering Aspects of Shape Memory Alloys*. Butterworth-Heinemann Ltd., Oxford, U.K., 1990.

7. Duerig T, Pelton A, Stöckel D. (1999) An overview of Nitinol medical applications. *Materials Science and Engineering A* **273-275**:149-160.

8. Frank, T.G., Xu, W., Cuschieri, A. (2000) Instruments based on shape-memory alloy properties for minimal access surgery, interventional radiology and flexible endoscopy. *Minimally Invasive Therapy and Allied Technologies*. **9**(2):89-98.

9. Smith, C., Villanueva, A., Joshi, K., Tadesse, Y., Priya, S. (2011) Working principle of bio-inspired shape memory alloy composite actuators. *Smart Materials and Structures*. **20:**012001.

10. Keefe, A.C., et al. (2007) Development of a shape memory alloy heat engine through experiment and modeling. Proc. of the ASME 2011 Conference on Smart Materials, Adaptive Structures and Intelligent Systems, Phoenix, Arizona, USA.

11. Massalski, T.B., Okamoto, H., Subramanian, P.R. *Binary Alloy Phase Diagrams*. ASM International, Novelty, OH, USA, 1990.

12. Frenzel J, George EP, Dlouhy A, Somsen Ch, Wagner MF-X, Eggeler G. (2010) Influence of Ni on martensitic phase transformation in NiTi shape memory alloys. *Acta Materialia* **58**:3444-3458.

13. Hall, P.C. (2000) Resistance welding Ti-rich Nitinol wire. Proc. of the international conference on Shape Memory and Superelastic Technologies (SMST), Pacific Grove, California, USA.

14. Huang, X. & Liu, Y. (2001) Effect of annealing on the transformation behavior and superelasticity of NiTi shape memory alloy. *Scripta Materialia* **45**, 153-160.

15. Frick, C.P., et al. (2005) Thermal processing of polycrystalline NiTi shape memory alloys. *Materials Science and Engineering A* **405**, 34-49.

16. Otsuka, K., Wayman, C.M. *Shape Memory Materials*. Cambridge University Press, Cambridge, U.K., 1999.

17. Lagoudas, D.C. *Shape Memory Alloys*. Springer, New York, NY, USA, 2008.

18. Philip, T.V., Beck, P.A. (1957) CsCl-type ordered structures in binary alloys of transition elements. Transactions AIME. **209**:1269-1271.

19. Otsuka, K., Sawamura, T., Shimizu, K. (1971) Crystal structure and internal defects of equiatomic TiNi martensite. Physica status solidi (a). **5**(2):457-470.

20. Gupta, S.P., Johnson, A.A. (1973) Morphology and crystallography of β' martensite in TiNi alloys. *Materials Transactions, The Japan Institute of Metals*. **14**:292-302.

21. Onda, T., Bando, Y., Ohba, T., Otsuka, K. (1992) Electron microscopy study of twins in martensite in a Ti-50.0at%Ni alloy. *Materials Transactions, The Japan Institute of Metals*. **33**:354-359.

22. Ling, H.C., Roy, K. (1981) Stress-induced shape change and shape memory in the R and martensite transformations in equiatomic NiTi. *Metallurgical and Materials Transactions A.* **12**(12):2101-2111.

23. Honma, T., Matsumoto, M., Shugo, Y., Nishida, M., Yamazaki, I. In: Kimura, H., Izumi, O., ed. (1980) Proc. of the4th international conference on Titanium, Kyoto, AIME:1455.

24. Ren, X., Miura, N., Zhang, J., Otsuka, K., Tanaka, K., Koiwa, M., Suzuki, T., Cumlyakov, Yu.I., Asai, M. (2001) A comparative study of elastic constants of Ti-Ni-based alloys prior to martensitic transformation. *Materials Science and Engineering A*. **312**:196-206.

25. Dlougy, A., Khalil-Allafi, J., Eggeler, G. (2003) Multiple-step martensitic transformations in Ni-rich NiTi alloys – an in-situ transmission electron microscopy investigation. *Philosophical Magazine*. **31**(3):339-363.

26. Nam, T.H., Saburi, T., Shimizu, K. (1990) Cu-content dependence of shape memory characteristics in Ti-Ni-Cu alloys. *Materials Transactions*. **31**(11):959-967.

27. Ren, X., Otsuka, K. (1998) The role of softening in elastic constant c_{44} in martensitic transformation. *Scripta Materialia*. **38**(11):1669-1675.

28. Wu SK, Wayman CM. (1989) On the reciprocal lattice of the "premartensitic" R-phase in TiNi shape memory alloys. *Acta Metall*urgica **37**(10):2805-2813.

29. Ren, X., Miura, N., Zhang, J., Otsuka, K., Tanaka, K., Koiwa, Suzuki, T., Chumlyakov, Y.I., Asai, M. (2001) A comparative study of elastic constants of Ti-Ni-based alloys prior to martensitic transformation. *Materials Science and Engineering A*. **312**:196-206.

30. Miyazaki, S., Otsuka, K., Suzuki, Y. (1981) Transformation pseudoelasticity and deformation behavior in a Ti-50.5at%Ni alloy. *Scripta Metallurgica.* **15**:287-292.

31. Miyazaki, S., Kawai, T., Otsuka, K. (1982) On the origin of intergranular fracture in β phase shape memory alloys. *Scripta Metallurgica*. **16**:431-436.

32. Miyazaki, S., Kohiyama, Y., Otsuka, K. (1990) Effects of several factors on the ductility of the Ti-Ni alloy. *Materials Science Forum*. **56-58**:765-770.

33. Otsuka, K., Shimizu, K. (1986) Pseudoelasticity and shape memory effects in alloys. *International Metals Reviews*. **31**(1):93-114.

34. Miyazaki, S., Kimura, S., Otsuka, K., Suzuki, Y. (1984) The habit plane and transformation strains associated with the martensitic transformation in Ti-Ni single crystals. *Scripta Metallurgica*. **18**:883-888.

35. Miyazaki, S., Igo, Y., Otsuka, K. (1986) Effect of thermal cycling on the transformation temperatures of Ti-Ni alloys. *Acta Metallurgica*. **34**(10):2045-2051.

36. Piao, M., Otsuka, K., Miyazaki, S., Horikawa, H. (1993) Mechanism of the A_s temperature increase by pre-deformation in thermoelastic alloys. *Materials Transactions, Japan Institute for Materials*. **34**(10):919-929.

37. Hamilton, R.F., Sehitoglu, H., Chumlyakov, Y., Maier, H.J. (2004) Stress dependence of the hysteresis in single crystal NiTi alloys. *Acta Materialia*. **52**(11):3383-3402.

38. Liu, Y., Xie, Z., Van Humbeeck, J., Delaey, L. (1998) Asymmetry of stress-strain curves under tension and compression for the NiTi shape memory alloys. *Acta metallurgica.* **46**(12):4325-4338.

39. Miyazaki, S., Otsuka, K., Wayman, C.M. (1989) The shape memory mechanism associated with the martensitic transformation in Ti-Ni alloys – I. Self-accommodation. *Acta Metallurgica*. **37**(7):1873-1884.

40. Saburi, T., Nenno, S., Nishimoto, Y., Zeniya, M. (1986) Effects of thermo-mechanical treatment on the shape memory effect and the pseudoelasticity of Ti-50.2 Ni and Ti-47.5 Ni-2.5 Fe alloys. *Tetsu-to-Hagané (The Iron and Steel Institute of Japan)*. **72**(6):571-578.

41. Nagasawa, A., Ishino, Y., Enami, K., Abe, Y., Nenno, S. (1974) Reversible shape memory effect. *Scripta Metallurgica*. **8**(9):1055-1060.

42. Šittner, P., Liu, Y., Novák, V. (2005) On the origin of Lüders-like deformation of NiTi shape memory alloys. *Journal of the Mechanics and Physics of Solids*. **53**(8):1719-1746.

43. Shaw, J.A., Kyriakides, S. (1997) On the nucleation and propagation of phase transformation fronts in a NiTi alloy. *Acta Materialia*. **45**(2):683-700.

44. Plietsch, R., Ehrlich, K. (1997) Strength differential effect in pseudoelastic NiTi shape memory alloys. *Acta Meterialia*. **45**(6):2417-2424.

45. Brinson, L.C.L., Schmidt, I., Lammering, R. (2004) Stress-induced transformation behavior of a polycrystalline NiTi shape memory alloy: micro and macromechanical investigations via in situ optical microscopy. *Journal of the Mechanics and Physics of Solids.* **52**(7):1549-1571.

46. Pelton, A.R., DiCello, J., Miyazaki, S. (2000) Optimisation of processing and properties of medical grade Nitinol wire. *Minimally Invasive Therapy Allied Technologies.* **9**(1):107-118.

47. Favier, D., Liu, Y., Orgéas, L., Sandel, A., Debove, L., Comte-Gaz, P. (2006) Influence of thermomechanical processing on the superelastic properties of a Ni-rich Nitinol shape memory alloy. *Materials Science and Engineering A*. **429**:130-136.

48. Tang, W. (1997) Thermodynamic study of the low-temperature phase, B19' and martensitic transformation in near equiatomic Ti-Ni shape memory alloys. *Metallurgical Materials Transactions A.* **28A**:537-544.

49. Hodgson, D., Russell, S. (2000) Nitinol melting, manufacture and fabrication. *Minimally Invasive Therapy and Allied Technologies.* **9**(2):61-66.

50. Miyazaki, S., Ohmi, Y., Otsuka, K., Suzuki, Y. (1982) Characteristics of deformation and transformation pseudoelasticity in Ti-Ni alloys. *Journal de Physique Colloques.* **43**(C4):255-260.

51. Ren, X., Otsuka, K. (2000) Why does the martensitic transformation remperature strongly depend on composition? *Materials Science Forum*. **327-328**:429-432.

52. Planes, A., Monosa, L., Rioa-Jara, D., Ortin. J. (1992) Martensitic transformation of Cu-based shape-memory alloys: Elastic anisotropy and entropy change. *Physics Rev B.* **45**(14):7633-7639.

53. Manosa, L., Zarestky, J., Lograsso, T., Dalaney, D.W., Stassis, C. (1993) Lattice-dynamical study of the premartensitic state of the Cu-Al-Be alloys. *Physics Rev B.* **48**:15708-15711.

54. Manosa, L., Jurado, M., Planes, A., Zarestky, J., Lograsso, T., Stassis, C. (1994) Elastic constants of bcc Cu-Al-Ni alloys. *Physics Rev B.* **48**:9969-9972.

55. Ren, X., Miura, N., Zhang, J., Otsuka, K., Tanaka, K., Koiwa, M., Suzuki, T., Chumlyakov, Y.I. (2001) A comparative study of elastic constants of Ti-Ni-based alloys prior to martensitic transformation. *Materials Science and Engineering A*. **312**:196-206.

56. Ren, X., Taniwaki, K., Otsuka, K., Suzuki, T., Tanaki, K., Chumlaykov, Y.I., Ueiki, T. (1999) Elastic constants of $Ti_{50}Ni_{30}Cu_{20}$ alloy prior to martensitic transformation. *Philos Mag A*. **79**:31-41.

57. Frick CP, Ortega AM, Tyber J, Gall K, Maier HJ. (2004) Multiscale structure and properties of cast and deformation processed polycrystalline NiTi shape-memory alloys. *Metallurgical and Materials Transactions A* **35A**:2013-2025.

58. Prokoshkin SD, Khmelevskaya LYU, Brailovski V, Trochu F, Turenne S, Turilina VYU. (2004) Thermomechanical treatments and their influence on the microstructure and stress/strain diagrams of NiTi shape memory alloys. *Canadian Metallurgical Quarterly* **43**(1):95-108.

59. Morawiec H, Stróz D, Chrobak D. (1995) Effect of deformation and thermal treatment of NiTi alloy on transition sequence. *Journal de Physique IV, Colloque C2, supplement Journal de Physique III* **5**:205-210.

60. Bataillard L, Bidaux J-E, Gotthardt R. (1998) Interaction between microstructure and multiple-step transformation in binary NiTi alloys using in-situ transmission electron microscopy observation. *Philosophical Magazine A* **78**(2):327.

61. Miura, F., Mogi, M., Ohura, Y. (1988) Japanese NiTi alloy wire: use of the direct electric resistance heat treatment method. *European Journal of Orthodontics.* **10**:187-191.

62. Airoldi, G., Riva, G. (1995) Pseudoelasticity of NiTi orthodontic wires modified by current methodologies: A critical comparison. *Journal de Physique IV, Colloque C2, supplement au Journal de Physique III.* **5**:397-402.

63. Cluff, D., Corbin, S., Gorbet, R. (2009) Powder metallurgy fabrication of hybrid monolithic SMA actuators. Proc. of Cansmart 2009, Montreal, Quebec, Canada. October 22-23, 2009.

64. Hey, J.C., Jardine, A.P. (1994) Shape memory NiTi synthesis from elemental powders. *Materials Science and Engineering A.* **188**:291-300.

65. Whitney, M., Corbin, S.F., Gorbet, R.B. (2008) Investigation of the mechanisms of reactive sintering and combustion synthesis of NiTi using differential scanning calorimetry and microstructural analysis. *Acta Materialia.* **56**:559-570.

66. Vamsi Krishna, B., Bose, S., Bandyopadhyay, A. (2007) Laser processing of net-shape NiTi shape memory alloy. *Metallurgical and Materials Transactions A.* **38A**:1096-1103.

67. Mahmud, A.S, Liu, Y., Nam, T.H. (2008) Gradient anneal of functionally graded NiTi. *Smart Materials and Structures.* **17**:015031.

68. Sevilla, P., Martorell, F., Libenson, C., Planell, J.A., Gil, F.J. (2008) Laser welding of NiTi orthodontic archwires for selective force application. *Journal of Materials Science: Materials in Medicine.* **19**:525-529.

69. Meng, Q., Liu, Y., Yang, H., Shariat, B.S., Nam, T.H. (2012) Functionally graded NiTi strips prepared by laser surface anneal. *Acta Materialia.* **60**:1658-1668.

70. Daly, M., Pequegnat, A., Zhou, Y., Khan, M.I. (2012) Enhanced thermomechanical functionality of a laser processed hybrid NiTi-NiTiCu shape memory alloy. *Smart Materials and Structures.* **21**(4):045028.

71. Daly, M., Pequegnat, A., Zhou, Y., Khan, M.I. (2013) Fabrication of a novel laser-processed NiTi shape memory microgripper with enhanced thermomechanical functionality. *Intelligent Material Systems and Structures.* **24**(8):984.

72. Khan, M.I., Pequegnat, A., Zhou, Y. (2012) Multiple memory shape memory alloys. *Advanced Engineering Materials* **15**(5):386.

73. Khan, M.I.; Zhou Y. N.; Innovative Processing Technologies, assignee. Methods and Systems for Processing Materials, Including Shape Memory Materials. World Patent application WO/2011/014962. 2010 Aug 6.

74. Tam, B., Khan, M.I., Zhou, Y. (2011) Mechanical and functional properties of laser-welded Ti-55.8 Wt Pct Ni Nitinol wires. *Metallurgical and Materials Transactions A.* **42**(8):2166-2175.

75. Chan, C.W., Man, H.C., Yue, T.M. (2012) Effect of post-weld heat-treatment on the oxide film and corrosion behaviour of laser-welded shape memory NiTi wires. *Corrosion Science* **56**:158-167.

76. Yan, X.J., Yang, D.Z., Liu, X.P. (2006) Electrochemical behavior of YAG laser-welded NiTi shape memory alloy. *Transactions of Nonferrous Metals Society of China* **16**:572-576.

77. Yan, X.J., Yang, D.Z. (2006) Corrosion resistance of laser spot-welded joint of NiTi wire in simulated human body fluids. *Journal of Biomedical Materials Research* **77A**(1):97-102.

78. Hsu, Y.T., Wang, Y.R., Wu, S.K., Chen, C. (2001) Effect of CO_2 laser welding on the shape memory and corrosion characteristics of TiNi alloys. *Metallurgical and Materials Transactions A* **32A**:569-576.

79. Yan, X.J., Yang, D.Z., Liu, X.P. (2007) Corrosion behavior of a laser-welded NiTi shape memory alloy. *Materials Characterization* **58**:623-628.

80. Man, H.C., Cui, Z.D., Yue, T.M. (2001) Corrosion properties of laser surface melted NiTi shape memory alloy. *Scripta Materialia.* **45:**447-1453.

81. Cui, Z.D., Man, H.C., Yang, X.J. (2005) The corrosion and nickel release behavior of laser surface-melted NiTi shape memory alloy in Hanks, solution. *Surface & Coatings Technology* **192**:347-353.

82. Schloßmacher, P., Haas, T., Schüßler, A. (1997) Laser-welding of a Ni-rich TiNi shape memory alloy: Mechanical behavior. *Journal de Physique IV.* **7**C5, C5/251-C5/256.

83. Ogata, Y., Takatugu, M., Kunimasa, T., Uenishi, K., Kobayashi, K. (2004) Tensile strength and pseudo-elasticity of YAG laser spot melted Ti-Ni shape memory alloy wires. *Materials Transactions.* **45**(4):1070-1076.

84. Falvo, A., Furgiuele, F.M., Maletta, C. (2005) Laser welding of a NiTi alloy: Mechanical and shape memory behaviour. *Materials Science and Engineering A.* **412**:235-240.

85. Maletta, C., Falvo, A., Furgiuele, F., Barbieri, G., Brandizzi, M. (2008) Fracture behaviour of Nickel-Titanium laser welded joints. *Journal of Materials Engineering and Performance.* **18**(5-6):569-574.

86. Schloßmacher P, Haas T, Schüßler A. (1994) Laser welding of Ni-Ti shape memory alloys. Proc. of the First Inter. Conf. on Shape Memory and Superelastic Technologies, Pacific Grove, CA, USA, p. 85-90.

87. Tuissi A, Besseghini S, Ranucci T, Squatrito F, Pozzi M. (1999) Effect of Nd:YAG laser welding on the functional properties of the Ni-49.6 at.%Ti. *Materials Science and Engineering A* **A273-275**:813-817.

88. Yan, X.J., Yang, D.Z., Liu, X.P. (2007) Influence of heat treatment on the fatigue life of a laser-welded NiTi alloy wire. *Materials Characterization.* **58**:262-266.

89. Chan, C.W., Man, H.C., Yue, T.M. (2012) Effect of postweld heat treatment on the microstructure and cyclic deformation behavior of laser-welded NiTi-shape memory wires. *Metallurgical and Materials Transactions A.* **43A**:1956-1965.

90. Song, Y.G., Li, W.S., Li, L., Zheng, Y.F. (2008) The influence of laser welding parameters on the microstructure and mechanical property of the as-jointed NiTi alloy wires. *Materials Letters.* **62**:2325-2328.

91. Yan, X.J., Yan, D.Z., Qi, M. (2006) Rotating-bending fatigue of a laser-welded superelastic NiTi alloy wire. *Materials Characterization.* **57**:58-63.

92. Gong, W.H., Chen, Y.H., Ke, L.M. (2011) Microstructure and properties of laser micro welded joint of TiNi shape memory alloy. *Transactions of Nonferrous Metals Society of China.* **21**:2044-2048.

93. Khan, M.I, Zhou, Y. (2010) Effects of local phase conversion on the tensile loading of pulsed Nd:YAG laser processed Nitinol. *Materials Science and Engineering A.* **527**:6235-6238.

94. David, S.A. (ed.) *Trends in Welding Research in the United States*. Block-Bolten, A., Eager, T.W. Selective evaporation of metals from weld pools, 55-73 (ASM International, Novelty, OH, 1982).

95. Moon, D.W. & Metzbower, E.A. (1983) Laser beam welding of aluminum alloy 5456. *Welding Journal, research supplement* **62**:53-58.

96. Block-Bolten, A. & Eager, T.W. (1984) Metal vaporization from weld pools. *Metallurgical Transactions B* **15B**:463-469.

97. Khan, P.A.A. & Debroy, T. (1984) Alloying element vaporization and weld pool temperature during laser welding of AISI 202 stainless steel. *Metallurgical Transactions B* **15B**:641-644.

98. Blake, A. & Mazumder, J. (1985) Control of magnesium loss during laser welding of Al-5083 using a plasma suppression technique. *Journal of engineering for industry* **107**(3):275-280.

99. Collur, M.M., Paul, A. & Debroy, T. (1987) Mechanism of alloying element vaporization during laser welding. *Metallurgical Transactions B* **18B**:733-740.

100. He, X., Debroy, T. & Fuerschbach, P.W. (2003) Alloying element vaporization during laser spot welding of stainless steel. *Journal of Physics D: Applied Physics* **36**:3079-3088.

101. He, X., Debroy, T. & Fuerschbach, P.W. (2004) Composition change of stainless steel during microjoining with short laser pulse. *Journal of Applied Physics* **96**(8):4547-4555.

102. Jandaghi, M., Parvin, P., Torkamany, M. J. & Sabbaghzadeh, J. (2008) Alloying element losses in pulsed Nd :YAG laser welding of stainless steel 316. *Journal of Physics D: Applied Physics* **41**:235503.

103. Funakubo, H. (ed) *Shape memory materials* (Gordon and Breach Scientific Publishers, New York, NY 1987).

104. Eckelmeyer, K.H. (1976) The effect of alloying on the shape memory phenomenon in Nitinol. *Scripta Metallurgica* **10**(8):667-672.

105. Donkersloot, H.C. & Van Vucht, J.H.N. (1970) Martensitic transformations in gold-titanium, palladium- titanium and platinum-titanium alloys near the equiatomic composition. *Journal of Less-Common Metals* **20**(2):83-91.

106. Lindquist, P.G. & Wayman, C.M. (1989) Transformation behavior of Tri50 (Ni (50-x) Pdx) and Tisa- (Ni (50-x) Ptx) alloys. *Proc MRS Int Mtg Adv Mater* **9**:123.

107. Zarnetta, R., et al. (2010) Identification of quaternary shape memory alloys with near-zero thermal hysteresis and unprecedented functional stability. *Advanced Functional Materials* **20**:1917-1923.

108. Zarinejad, M., Liu, Y. (2008) Dependence of transformation temperatures of NiTi-based shape-memory alloys on the number and concentration of valence electrons. *Advanced Functional Materials* **18**:2789-2794.

109. Cui, J., et al. (2006) Combinatorial search of thermoelastic shape-memory alloys with extremely small hysteresis width. *Nature Materials* **5**:286-290.

110. Recarte, V., Perez-saez, R.B., Bocanegra, M.L. & NO, San Juan, J. (2002) Influence of Al and Ni concentration on the martensitic transformation in Cu-Al-Ni shape-memory alloys. *Metallurgical Materials Transactions A* **33**A:2581-2591.

111. Yaws C.L. *Handbook of Vapor Pressure Vol. 4* (Gulf Publishing Co., Houston, TX, 1995).

112. Wang, F.E., Beuhler, W.J. & Pickart, S.J. (1965) Crystal structure and a unique "martensitic" transition of TiNi. *Journal of Applied Physics* **36**:3232-3239.

113. Butler, S.R., Hanlon, J.E. & Wasilewski, R. J. (1967) On martensitic transformation in TiNi. *Metal Science Journal* **1**:104-110.

114. Dautovich, D.P., Melkvi, Z., Purdy, G.R. & Stager, C.V. (1966) Calorimetric study of a diffusionless phase transition in TiNi. *Journal of Applied Physics* **37**:2513-2516.

115. Wasilewski, R.J., Butluer, S.R., Hanlon, J.E. & Wordon, D. (1971) Homogeneity range and the martensitic transformation in TiNi. *Metallurgical Transaction* **2**:229-238.

116. Filip, P. & Mazanec, K. (2001) On precipitation kinetics in TiNi shape memory alloys. *Scripta Materialia* **45**:701-707.

117. Lide, D.R. Ed. *CRC Handbook of Chemistry and Physics, 84th Edition*. CRC Press, Inc. Boca Raton, Florida, USA, 2003.

118. Wever, D.J., Veldhuizen, A.G., de Vries, J., Busscher, H.J., Uges, D.R.A, van Horn, J.R. (1998) Electrochemical and surface characterization of a nickel-titanium alloy. *Biomaterials*. **19**:761-769.

119. Shabalovskaya, S.A. (2002) Surface, corrosion and biocompatibility aspects of nitinol as an implant material. *Bio-Medical Materials and Engineering* **12**:69-109

120. Shabalovskaya, S., Anderegg, J., Van Humbeeck, J. (2008) Critical overview of Nitinol surfaces and their modifications for medical applications. *Acta Biomaterialia* **4**:447-67.

121. Shabalovskaya, S.A. (2001) Physicochemical and biological aspects of nitinol as a biomaterial. *International Materials Reviews* **46**(5):233-50.

122. Cissé, O., Savadogo, O., Wu, M., Yahia, L'H. (2001) Effect of surface treatment of NiTi alloy on its corrosion behavior in Hanks' solution. *Journal of Biomedical Materials Research* **61**:339-345.

123. Bass, J.K., Fine, H., Cisnero, G.J. (1993) Nickel hypersensitivity in the prosthodontics patient. *American Journal of Orthodontics and Dentofacial Orthopedics* **103**:280-285.

124. Berger-Gorbet, M., Broxup, B., Rivard, C., Yahia, L`H. (1996) Biocompatibility testing of Ni-Ti screw using immune histochemistry on section containing metallic implants. *Journal of Biomedical Materials Research* **32**:243-248.

125. Sevilla, P., Martorell, F., Libenson, C., Planell, J.A., Gil, F.J. (2008) Laser welding of NiTi orthodontic archwires for selective force application. *Journal of Materials Science: Materials in Medicine* **19:**525-529.

126. Villermaux, F., Tabrizian, M., Yahia, L.H., Meunier, M., Piron, D.L. (1997) Excimer laser treatment of NiTi shape memory alloy biomaterials. *Applied Surface Science* **109-110**:62-66.

127. Meier, H., Czechowicz, A., Langbein, S. (2010) Smart control systems for smart materials. *Proc. of the Int. Conf. on shape memory and superelastic technologies, Pacific Grove California, USA*. 224-225.

128. Ma, N., Song, G., Lee, H.J. (2004) Position control of shape memory alloy actuators with internal electrical resistance feedback using neural networks. *Smart Materials and Structures* **13**: 777-783.

129. Dutta, S.M., Ghorbel, F.H., Dabney, J.B. (2005) Modeling and control of a shape memory alloy actuator. *Proc. of IEEE Int. Symposium on Intelligent Control, Limassol, Cyprus.* 1007-1012.

130. Shabalovskaya, S., Anderegg, J., Laab, F., Thiel, P.A., Rondelli, G. (2003) Surface conditions of nitinol wires, tubing, and as-cast alloys: the effect of chemical etching, aging in boiling water, and heat treatment. *Journal of Biomedical Materials Research A: Applied Biomaterials* **65**(1):193-203.

131. Vojtech, D., Kubasek, J., Voderova, M., Seda, P., Michalcova, A. (2011) Study of mechanical, fatigue and corrosion, properties of the superelastic ni-ti alloy. In: Proceedings of 20th Anniversary International Conference on Metallurgy Materials, Czech Republic, EU; p. 1-7.

132. Miachardi, A., Aparicio, C., Planell, J.A., Gil, F.J. (2006) New oxidation treatment of NiTi shape memory alloys to obtain Ni-free surfaces and to improve biocompatibility. *Journal of Biomedical Materials Research A: Applied Biomaterials* **77**(2):249-56.

133. Pequegnat, A., Daly, M., Wang, J., Zhou, Y., Khan, M.I. (2012) Dynamic actuation of a novel laser processed NiTi linear actuator. *Smart Materials and Structures* **21**(9):094004.

134. Ikuta, K., Tsukamoto, M., Hirose, S. (1988) Shape memory alloy servo actuator system with electrical resistance feedback and application for active endoscope. *Proc. IEEE Int. Conf. on Robotics and Automation, Piscataway, NJ*, USA. **1**:427-430.

135. Murasawa, G., Kitamura, K., Yoneyama, S., Miyazaki, S., Miyata, K., Nishioka, A., Koda, T. (2009) Macroscopic stress-strain curve, local strain band behaviour and the texture of NiTi thin sheets. *Smart Materials and Structures* **18**(5):055003.

136. Liu, Y., Van Humbeeck, J., Stalmans, R., Delaey, L. (1997) Some aspects of the properties of NiTi shape memory alloys. *Journal of Alloys and Compounds* **247**(1-2):115-121.

137. Liu, Y., Xie, Z.L., Van Humbeeck, J., Delaey, L. (1999) Effect of texture orientation on the martensite deformation of NiTi shape memory alloy sheet. *Acta Metallurgica* **47**(2):645-660.

138. Eggeler, G., Hornbogen, E., Yawny, A., Heckmann, A., Wagner, M. (2004) Structural and functional fatigue of shape memory alloys. *Materials Science and Engineering A* **378**:24-33.

139. Sofla, A.Y.N., Elzey, D.M., Wadley, H.N.G. (2008) Cyclic degradation of antagonistic shape memory actuated structures. *Smart Materials and Structures* **17**:1-6.

140. Grossmann, C., Frenzel, J., Sampath, V., Depka, T., Oppenkowski, A., Somsen, C., et. al. (2008) Processing and property assessment of NiTi and NiTiCu shape memory actuator springs. *Mat.-wiss. u. Werkstofftech* **39**(8):499-510.

141. Hall, P.C., (2000) In Proc. of SMST-2000: The Inter. Conf. on Shape Memory and Superelastic Technologies, Pacific Grove, CA, USA, p. 67.

142. Fan, G., Chen, W., Yang, S., Zhu, J., Ren, X., Otsuka, K. (2004) Origin of abnormal multi-stage martensitic transformation behavior in aged Ni-rich Ti-Ni shape memory alloys. *Acta Materialia* **52**:4351-4362.

143. Zhou, Y., Zhang, J., Fan, G., Ding, X., Sun, J., Ren, X., Otsuka, K. (2005) Origin of 2-stage R-phase transformation in low-temperature aged Ni-rich Ti-Ni alloys. *Acta Materialia* **53**:5365-5377.

144. Filip, P., Mazanec, K. (2001) On precipitation kinetics in TiNi shape memory alloys. *Scripta Materialia* **45**:701-707.

145. Huang, X., Liu, Y. Effect of annealing on the transformation behavior and superelasticity of NiTi shape memory alloy. *Scripta Materialia* **45**:153-160.

146. Nishida, M., Toru, H., Ohba, T., Yamaguchi, K., Tanaka, K., Yamauchi, K. (2003) *Materials Transactions **44**(12):2631-2636.*

147. Otsuka, K., Shimizu, K. (1986) Pseudoelasticity and shape memory effects in alloys. *International Metals Review* **31**(3):93-114.

148. Schloβmacher, P., Haas, T., Shüβler, A. (1997) Laser-welding of Ni-rich TiNi shape memory alloy: Pseudoelastic properties. Proc. of SMST-1997: The Inter. Conf. on Shape Memory and Superelastic Technologies, Pacific Grove, CA, USA, p. 137.

149. Kompatscher, M., Demé, B., Kostroz, G., Somsen, Ch., Wassermann, E.F. (2002) Small-angle neutron scattering of precipitates in Ni-Ti shape memor alloys. *Acta Materialia* **50**:1581-1586.

150. Somsen, Ch., Kästner, J., Wassermann, E.F., Boullay, Ph., Schryvers. (2001) Microstructure of quenched Ni-rich Ni-Ti shape memory alloys. *Journal de Physique IV France* **11**:Pr8-445-449.

151. Stróz, D. (1997) Precipitation process in a deformed NiTi near equiatomic alloy. *Journal de Physique IV France* **7**:C5-293-297.

152. Delville, R., Malard, B., Pilch, J., Sittner, P., Schryvers, D. (2010) Microstructure changes during non-conventional heat treatment of thin Ni-Ti wires by pulsed electric current studied by transmission electron microscopy. Acta Materialia **58**:4503-4515.

153. Leary, R.K., Merson, E., Birmingham, K., Harvey, D., Brydson, R. (2010) Microstructural and microtextural analysis of InterPulse GTCAW welds in Cp-Ti and Ti-6Al-4V. Material Science and Enginering A **527**:7694-7705.

154. Lin, H.C., Wu, S.K., Lin, J.C. (1993) Proc. Inter. Conf. Martensitic Trans 1992: (CM Wayman and J Perkins, eds.), Monterey Inst. of Advanced Studies, Carmel, CA, USA, p.875.

155. Treppmann, D., Hornbogen, E., Wurzel, D. (1995) The effect of combined recrystallization and precipitation process on the functional and structural properties in NiTi alloys. *Journal de Physique IV, Colloques C2, Suppliment Journal de Physique III* **5**:569-574.

156. Zhu, L., Fino, J.M., Pelton, A.R. (2003) Oxidation of Nitinol. In: Proceedings of Smart Materials and Superelastic Technologies, California, USA.

157. Chu, C.L., Chung, C.Y., Chu, P.K. (2006) Surface oxidation of NiTi shape memory alloy in a boiling aqueous solution containing hydrogen peroxide. *Materials Science and Engineering A* **417**:104-109.

158. Firstov, G.S., Vitchev, R.G., Kumar, H., Blanpain, B., Van Humbeeck, J. (2002) Surface oxidation of NiTi shape memory alloy. *Biomaterials* **23**:4863-4871.

159. Chan, C.M., Trigwell, S., Duerig, T. (1990) Oxidation of an NiTi alloy. Surface and Interface Analysis **15**:349-354.

160. Trigwell, S., Hayden, R.D., Nelson, K.F., Selvaduray, G. (1998) Effects of surface treatment on the surface chemistry of NiTi alloy for biomedical applications. *Surface and Interface Analysis* **26**:483-489.

161. Shabalovskaya, S.A., Rondelli, G.C., Undisz, A.L., Anderegg, J.W., Burleigh, T.D., Rettermayr, M.E. (2009) The electrochemical characteristics of native Nitinol surfaces. *Biomaterials* **30**:3662-3671.

162. Munroe, N., Pulletikurthi, C., Haider, W. (2009) Enhanced biocompatibility of porous Nitinol. *Journal of Materials Engineering and Performance* **18**:765-767.

163. Schroeder, H.A., Balassa, J.J., Tipton I.H. (1962) Abnormal trace metals in man – nickel. *Journal of Chronic Diseases* **15**:51-65.

164. Kaaber, K., Veien, N.K., Tjell, J.C. (1978) Low nickel diet in the treatment of patients with chronic nickel dermatitis. *British Journal of Dermatology* **98**:197-201.

165. Bour, H., Nicolas, J.F., Garrigue, J.L., Demiden, A., Schmitt, D. (1994) Establishment of nickel-specific T cells from patients with allergic contact dermatitis: Comparison of different protocols. *Clinical Immunology and Immunopathology* **73**:142-145.

166. Rahim, M., Frenzel, J., Frotscher, M., Pfetzing-Micklich, J., Steegmuller, R., Wohlschlogel, M., Mughrabi, H., Eggeler, G. (2013) Impurity levels and fatigue lives of pseudoelastic NiTi shape memory alloys. *Acta Materialia* **61**:3677-3686.

167. Nam, T.H., Saburi, T., Shimizu, K. (1990) Cu-content dependence of shape memory characteristics in Ti-Ni-Cu alloys. *Materials Transaction* **31**(11):959-967.

168. Hosoda, H., Hanada, S., Inoue, K., Fukui, T., Mishima, Y., Suzuki, T. (1998) Martensite transformation temperatures and mechanical properties of ternary NiTi alloys with offstoichiometric compositions. *Intermetallics* **6**:291-301.

169. Hsieh, S.F., Wu, S.K. (1998) A study on ternary Ti-rich TiNiZr shape memory alloys. *Materials Characterization* **41**:151-162.

170. Kumar, P.K., Lagoudas, D.C., Zanca, K.J., Lagoudas, M.Z. (2006) Thermomechanical characterization of high temperature SMA actuators. Proc. of SPIE 6170, Smart Structures and Materials: Active Materials: Behaviour Mechanics, San Diego, CA, USA.